# DYNAMICS OF NANOPARTICLE COMBUSTION

BY

DAVID JAMES ALLEN

DISSERTATION

Submitted in partial fulfillment of the requirements
for the degree of Doctor of Philosophy in Mechanical Engineering
in the Graduate College of the
University of Illinois at Urbana-Champaign, 2015

Urbana, Illinois

Doctoral Committee:

Professor Nick Glumac, Chair
Professor Emeritus Herman Krier
Professor Greg Elliott
Professor Emeritus Surya Vanka

# ABSTRACT

A heterogeneous shock tube was used to ignite and measure the combustion behavior of the nano-aluminum suspension behind reflected shock waves. The burning time and particle temperatures were measured using optical diagnostics. In order to use pyrometry measurements for nano-aluminum particles, the emissivity of nano-alumina particles was also measured using the shock tube to heat the particles to known temperatures. The burning time and peak particle temperature results suggested that heat transfer models currently used for burning nanoparticles may significantly overestimate heat losses during combustion. By applying conventional non-continuum heat transfer correlations to burning nano-aluminum particles, the observed peak temperatures, which greatly exceed the ambient temperature, should only be observable if the burning time were very short, of the order of 1 $\mu$s, whereas the observed burning time is two orders of magnitude larger. These observations can be reconciled if the energy accommodation coefficient for these conditions is of the order of 0.005, which is the value suggested by Altman, instead of approximately unity, which is the common assumption. A simple model was developed for nano-aluminum particle combustion focusing on a surface controlled reaction as evidenced by experimental data and heat transfer to the surroundings. The simple model supports a low energy accommodation coefficient as suggested by Altman.

This result has significant implications on the heat transfer and performance of the nanoparticles in combustion environments. Direct measurement is needed in order to decouple the accommodation coefficient from the assumed combustion mechanism in the simple model. Time-resolved laser induced incandescence measurements were performed to measure the accommodation coefficient of nano-alumina particles in various gaseous environments. The accommodation coefficient was found to be 0.03, 0.07, and 0.15 in helium, nitrogen, and argon respectively at 300 K and 2 atm is each

environment. These values represent upper limits for the accommodation coefficient as scaling suggests that the accommodation coefficient will decrease with increasing particle and ambient temperature to values similar to those observed during shock tube measurements. The accommodation coefficient values measured using LII are similar to what has been seen for other metallic nanoparticles and significantly smaller than values used in soot measurements. The results will allow for additional modeling of the accommodation coefficient to be extended to other environments and support previous measurements of high combustion temperatures during nano-aluminum combustion. Further constant volume combustion measurements were used to determine the macroscopic effect of a low energy accommodation coefficient on the heat release to the ambient surrounding in a aersolized aluminum combusting medium.

*To my loved ones, ....*

# ACKNOWLEDGMENTS

I would like to first thank my advisers, Prof. Nick Glumac and Prof. Herman Krier. Their guidance, assistance, and encouragement has made this research possible and I am very grateful for the opportunities and knowledge they have provided me.

I would also like to thank my current and past colleagues, Patrick Lynch, John Rudolphi, Lance Kingston, Joe Kalman, Michael Clemenson, Brad Horn, Jeff Shen, Matthew Fitzgerald, Stacy Guo, Mike Soo, Chris Murzyn, and Jose Guadarrama for their advise, insights, and friendship. Melissa Radek, Laura Chen, Harry Rocha, Tommy Pielwicz, Phil Rezandk, and Colin Ringel were undergraduate assistants who were pivotal in the completion of this research, I am grateful for their assistance.

I would most like to thank my friends and family, especially my partner Elizabeth Trawick, my father William Allen, my mother Catherine Garrett, and my brother Bradley Allen. They have given me unending support and love, and it is because of them that I have the ability and confidence to succeed. I thank God for blessing me with such great influences in my life.

This research was sponsored by DTRA under grant HDTRA1-10-1-0003. The project manager is Dr. Suhithi Peiris. The Scanning Electron Micrographs were taken in the Frederick Seitz Materials Research Laboratory Central Facilities, University of Illinois, which are partially supported by the U.S. Department of Energy under Grant DEFG02-9-ER45439.

# TABLE OF CONTENTS

# LIST OF TABLES

# LIST OF FIGURES

# CHAPTER 1

# INTRODUCTION

The primary purpose of the following work is to measure the combustion behavior of nano-aluminum particles in a controlled environment. A heterogeneous shock tube was used to ignite and measure the combustion behavior of the nano-aluminum suspension behind reflected shock waves. The ignition delay, burning time, and particle temperatures were measured using optical diagnostics. Theoretical work by Altman [1] suggested that high temperature nanoparticles in high ambient temperatures may have a small thermal accommodation coefficient. In order to accurately model the nano-aluminum particle behavior it was necessary to experimentally determine fundamental heat transfer properties of the nanoparticles with the ambient surroundings. Laser induced incandescence experiments and constant volume combustion chamber experiments were used to obtain an estimate of the heat transfer occurring from the nanoparticles during combustion.

## 1.1 Research Motivation

Nano-aluminum combustion is an active area of research due to the potential to improve performance in propellants and explosives [2–8]. Aluminum, and other metals, are highly energetic materials as shown in Table 1.1. Lithium, beryllium, and boron have also been areas of active research, but aluminum is most commonly used because it has a relatively high energy density and is not volatile or toxic such as lithium and beryllium and is more readily ignited than boron [9–12]. The energy density of aluminum including the weight of the oxidizer is greater than that of liquid hydrogen and dynamite. However, aluminum requires high temperatures in order to ignite which limits its potential use to applications that require high temperatures such as explosives and propellants. In propellant formulations the aluminum

is used to raise the temperature (and in turn the pressure) of the combustion gases in the combustor. In the space shuttle rocket booster aluminum comprised 20% of the weight of the propellant mix. The remainder of the mix was HTPB binder and ammonium perchlorate oxidizer. In this scenario the HTPB binder initially burns to raise the temperature above the threshold of aluminum ignition. Once this threshold is met the aluminum combustion further raises the temperature. In explosive applications aluminum is used to enhance the initial blast [13]. In thermobaric devices the aluminum is dispersed prior to detonation and then reacts with the ambient environment upon passage of the detonation shock wave. In enhanced blast applications the aluminum may be used as a structural reactive casing which reacts with the detonation gases and ambient air after structural breakout.

**Table 1.1: Energy density of metals and other common fuels**

| **Fuel Type** | **MJ/kg** Fuel and Oxidizer | **MJ/kg** Fuel |
|---|---|---|
| Be | -24.4 | -67.6 |
| Li | -19.8 | -42.6 |
| B | -18.3 | -58.9 |
| Al | -16.4 | -31.0 |
| $H_2$ (liquid) | -15.0 | -121.0 |
| Mg | -14.9 | -24.7 |
| Gasoline | -10.0 | -45.0 |

In both propellant formulations and explosive applications there is a need to decrease the overall burning time of the aluminum particles. In rockets, if the particle does not fully combust within the residence time of the combustor then the excess energy is lost to the nozzle exit. In explosive applications the particles must ignite and combust rapidly behind the shock front in order to increase the blast pressure prior to quenching. For this reason there has been much interest in reducing the burning time and ignition temperature of aluminum particles. Reduction in the burning time and ignition delay will result in a greater energetic impulse which can lead to a significant increase in thrust in rockets and blast overpressure in explosives.

There have been various methods used in the attempt to increase the burning rate of aluminum. Sippel et al. attempted to decrease the ignition temperature of aluminum by alloying the aluminum particle with other more readily ignitable materials such as teflon and magnesium [14]. Others have

shown that the use of halogen gases in the oxidizing mix will decrease the ignition temperature of aluminum [15]. Of particular interest here is the effect of particle size reduction on the ignition and combustion characteristics. Scaling suggests that decreasing the particle size should have a significant decrease in the burning time of an aluminum particle [16]. It has also been shown that the ignition temperature of aluminum decreases with decreasing particle size in various experimental set-ups [17, 18]. However, as the particle size shifts to the nano-scale there is a significant transition from continuum mechanics and diffusion controlled combustion to the free molecular regime and kinetically limited combustion [19, 20]. The mechanism of nano-aluminum combustion remains poorly understood, and the motivation of the present work is to gain further insight into the fundamental processes that occur during nano-aluminum combustion.

## 1.2 Aluminum Particle Combustion

For larger particles burning in the diffusion limit, a fair understanding of the ignition and combustion characteristics has been demonstrated [16] such that predictive simulations are possible. However, for particle sizes approaching the micron scale under most conditions, many of the trends observed in large particle combustion no longer apply. Burning rates begin to deviate from a $d^2$ law, with exponents curiously observed to be less than unity [20–22]. The pressure dependence of the burning rate becomes significant [23], and there is evidence that the relative oxidation efficiencies of $CO_2$ and $H_2O$ change [20]. Peak combustion temperatures begin to decrease, and ignition temperatures are also markedly lower [24]. For nano-scale Al, a significant ambient temperature dependence on the burning rate emerges [25].

### 1.2.1 Micron-sized Aluminum Particle Combustion

Aluminum exposed to air is coated by a thin (0.5-4 nm) aluminum oxide layer that inhibits and controls the ignition of the particle [26]. It has been observed under slow heating rates that the aluminum oxide shell grows as it undergoes a phase transition from amorphous alumina to $\gamma$ crystalline phase, to $\alpha$ crystalline phase [27]. The particle continues to grow through this pro-

cess until ignition in reached. During the phase transition the bare aluminum is exposed to oxygen which allows it to react, grow, and heat the particle. As the particle temperature reaches the melting temperature of aluminum oxide ($\sim$2300 K) surface forces cause exposure of the bare aluminum which furthers combustion to completion.

The ignition process under higher heating rates ($\geq 10^6$ K/s) is more unclear. It has been suggested that the thermal stresses cause cracks in the oxide layer which allow for aluminum vapor to excape and react in the gas phase [28]. It has also been suggested that under higher heating rates the rate of reaction may exceed the rate of shell growth due to phase change leading again to aluminum vapor escape at high temperatures [29].

After ignition the process of large particle combustion is well understood. Glassman shows that for particles greater than 20 $\mu$m the primary reactions occur in the vapor phase in a classical droplet diffusion flame with an oxide layer [30]. The aluminum vapor escapes the oxide layer and diffuses to the flame front where reaction occurs with the oxidizer rapidly and progresses the combustion further. This flame structure is predicted by the Glassman criterion which suggests when the volatilization temperature of the oxide layer is greater than the boiling temperature of aluminum [30].

Reaction at the flame front leads to the production of smaller alumina product droplets which transport back to the surface and form oxide caps. This phenomena was observed in experiment by Melcher et al. [31]. The heat release due to combustion is insufficient to volatilize the alumina and therefore the peak temperature of the flame is the alumina volatilization temperature [30]. The primary reactions occur homogeneously in the gas phase and can be seen in Equations 1.1 - 1.4 for the aluminum/oxygen system. Figure 1.1 depicts the homogeneous aluminum combustion mechanism [32].

$$Al(g) + O_2 \rightarrow AlO + O \tag{1.1}$$

$$AlO + O_2 \rightarrow AlO_2 + O \tag{1.2}$$

$$2AlO + \frac{1}{2}O_2 \rightarrow Al_2O_3(l) \tag{1.3}$$

$$AlO_2 + AlO_2 \rightarrow Al_2O_3(l) + \frac{1}{2}O_2 \tag{1.4}$$

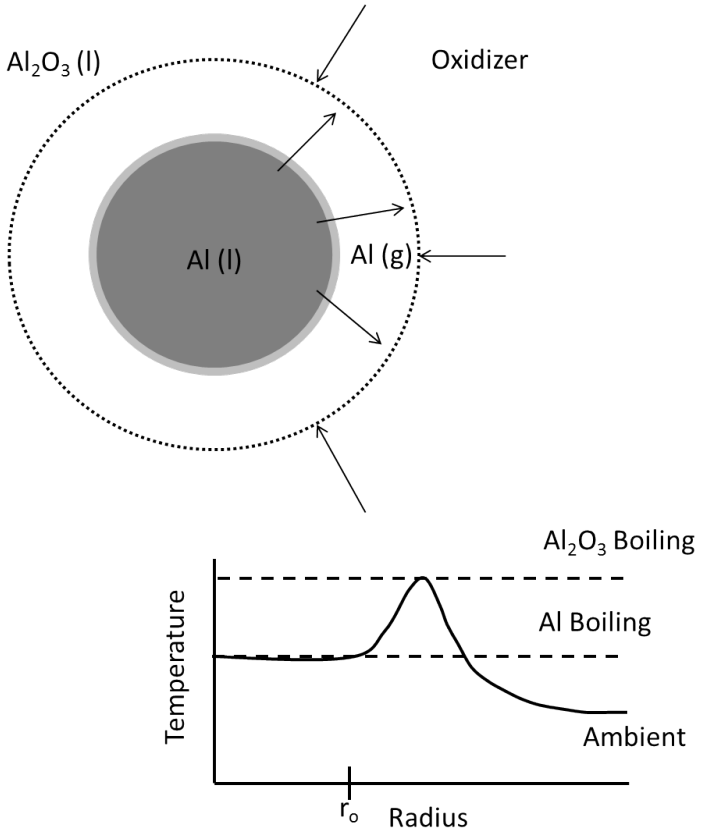


**Figure 1.1: Diagram of diffusion flame structure for aluminum combustion recreated from Bazyn [32]**

As previously stated the combustion mechanism of larger aluminum particles has been extensively studied using various experiments. Beckstead et al has produced a commonly used correlation for the burning time of aluminum particles greater than 20 $\mu$m [16]. The Beckstead correlation suggests that the burning rate is proportional to the particle diameter, ambient temperature, ambient pressure, and oxidizer mole fraction as shown in equation 1.5. The correlation suggests a diameter dependence of $d^{1.8}$ which is close to the theoretical diameter dependence of $d^2$ for the classical droplet diffusion solution [30]. This deviation is attributed to non-symmetry effects. The pressure and temperature dependence are relatively small within the diffusion controlled flame structure regime.

$$t_b \sim d^{1.8} T^{-0.2} P^{0.1} X^{-1} \tag{1.5}$$

It has been shown that as the particle size decreases below 20 $\mu$m the Beckstead correlation is no longer valid [19, 20]. This transition has been suggested to be due to a transition from diffusion controlled combustion to a kinetically limited combustion regime. Such a transition is supported using the Dahmkohler number scaling as shown by Glassman [30] in equation 1.6 which compares the rate of diffusion to the rate of the kinetics where $d$ is the diameter of the particle, $i$ is the mass stoichiometric coefficient, $k_s$ is the surface reaction rate, $D$ is the diffusion coefficient, and $m_{0,\infty}$ is the oxygen mass concentration far from the particle surface. The Dahmkohler number is linearly related to particle diameter expressing that as the particle diameter is decreased the characterisic kinetic time scale increases relative to the characteristic diffusion time scale.

$$Da = \frac{t_{b,dif}}{t_{b,kin}} = \frac{d\, i m_{0,\infty} k_s}{4 D ln(1 + i m_{0,\infty})} \tag{1.6}$$

Lynch has performed significant work on micron sized particles combusting within the transition regime to obtain a correlation for particle burn time [20]. His results showed a clear shift in the diameter dependence of the particle burn time. This has been suggested to be evidence of a transition in the combustion mechanism. Lynch states that in general the transition has been experimentally observed as a weakening of the diameter exponent of the burn time, enhanced pressure dependence, and a change in the observed flame structure.

The reaction front for a particle burning in the transition regime shifts towards the surface of the particle. This shift occurs because the primary rate limiting step is no longer diffusion of aluminum but instead surface limiting processes such as reaction kinetics or solid state diffusion. Theoretically this leads to the flame being shifted towards the surface of the particle and the temperature gradients significantly decreasing as shown in Figure 1.2. Figure 1.2 is a diagram of the surface flame structure with the corresponding temperature profile [32]. These type of flames have also been seen for larger particles burning in $CO_2$ [33] where kinetics are the rate limiting combustion step, and and it is commonly assumed that this flame structure is predominant in small particle combustion.

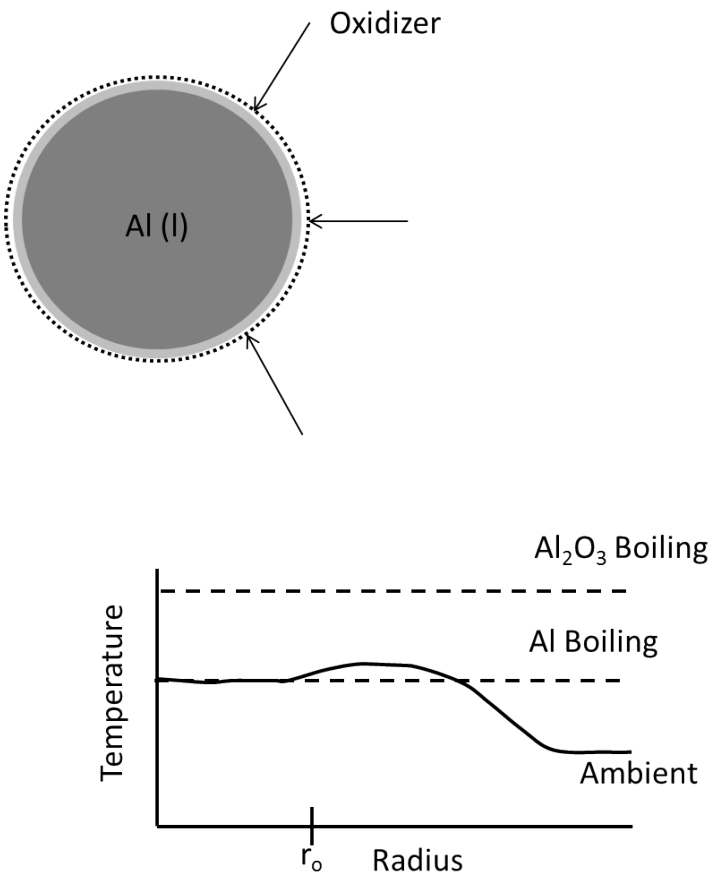


**Figure 1.2: Diagram of surface flame structure for aluminum combustion recreated from Bazyn [32]**

### 1.2.2 Nanoparticle Combustion

The combustion process for aluminum becomes increasingly unclear at the nanoscale. Several modeling efforts on nano-aluminum combustion have occurred [17, 24, 34], and some observations have been reconciled. However, a robust model capable of simulating combustion kinetics over a wide range of conditions has not yet been achieved.

It has been shown that nano-aluminum will ignite at temperatures much below the melting temperature of aluminum oxide (2300 K) which is the ignition temperature of aluminum particles greater than approximately 1 $\mu$m [18, 34]. This is a desirable property for metal combustion and is one of the main traits that has caused a great deal of interest in using nano-aluminum rather than larger particles. There are competing theories for the mechanism of nano-aluminum igntion in the temperature range between the

melting temperature of aluminum (∼930 K) and the melting temperature of aluminum oxide (∼2300 K) as larger particles do not ignite in this temperature range. The two primary ignition mechanism theories are the diffusive-oxidation mechanism [17, 18] and the melt dispersion mechanism [34, 35].

The diffusive oxidation mechanism, often called the shrinking core mechanism, suggests that oxidizer diffuses through the aluminum oxide layer to react with the aluminum core heterogeneously [36]. Initial reaction heats the particle which presumably increases the kinetics and potentially the solid state diffusion. In this model the solid-state diffusion is predicted to be the rate-limiting oxidation step. The solid state diffusion of the aluminum through the oxide coating is much slower than the gas phase diffusion of oxidizer to the outer particle surface. The relative rates of aluminum diffusion outward through the oxide layer and the oxygen diffusion inward through the oxide layer will determine the location of the primary reaction, and these rates are relatively uncertain. In any case, the primary reaction will either occur at outer particle surface if aluminum solid state diffusion is relatively rapid, or at the aluminum core surface beneath the oxide layer if the oxygen is able to diffuse through the oxide layer [37]. In this combustion model the gas phase concentration around the particle is the same as the classical kinetic limit discussed for micron sized particle combustion but with surface diffusion providing the limiting process instead of surface reaction.

The other primary nano-aluminum igntion and combustion mechanism theory is the melt dispersion mechanism. This mechanism predicts that the thermal stresses within the nanoparticle oxide layer during heating cause spallation into bare aluminum nano-clusters which are able to react in a kinetically limited fashion [34].

The two mechanisms offer drastically different views on the underlying combustion phenomena and there is evidence to support each in various ignition environments. Nano-thermite experiments have shown evidence of smaller product particles which is predicted due to particle spallation in the melt dispersion mechanism [35]. More recent work by Chowdhury et al using time of flight mass spectroscopy did not observe nano-aluminum clusters and found igntion and reaction rates that follow trends predicted by the diffusive oxidation method [38]. Therefore, it is uncertain which of the mechanisms is most appropriate or under what ignition conditions one mechanism is predominant over the other. The shock tube used in the present

experiments provides ignition conditions which are highly representative of ignition conditions in blast applications. In shock tube experiments, Lynch found little evidence of gas phase species during nano-aluminum combustion which agrees with predictions from the diffusive oxidation theory [39]. While not direct evidence of the diffusive oxidation theory, the lack of aluminum vapor during shock tube experiments with and without oxidation cannot be readily explained using the melt dispersion reaction mechanism.

As previously mentioned, in the melt-dispersion mechanism the kinetics is the rate limiting oxidation step, and in the diffusive oxidation theory the solid state diffusion represents the rate limiting step. In the classic kinetic limit, there is no gas-phase combustion, and species concentration and thermal gradients approach zero. Due to rapid heat transfer of small particles, the nanoparticle temperature is not expected to significantly exceed that of the ambient gas unlike the case of larger micron sized particles burning in the kinetically limited regime [40]. Indeed for some conditions, e.g. nano-aluminum burning in $CO_2$, negligible particle temperature rises have been observed in previous work. However, under other conditions with more efficient oxidizers at higher pressures, significant rises in particle temperature have been measured [25] which is unexpected and has yet to be reconciled. The present experiments investigate this phenomena more thoroughly to understand the heat transfer phenomena which may lead to the unexpected particle temperature rise. In order to do this a greater discussion of particle and nanoparticle heat transfer is necessary.

## 1.3 Particle Heat Transfer

The heat transfer of the particle plays an important role in combustion applications. It is well understood that as the particle size decreases there is a transition from the continuum regime of heat transfer to the free molecular regime of heat transfer [41]. These regimes are designated by the characteristic Knudsen number of the system. For aerosolized spherical particles the Knudsen number is defined as the ratio of the mean free path ($\lambda$) of the ambient gas to the radius of the spherical particle as shown in Equation 1.7 where the mean free path of the ambient gas is calculated as shown in Equation 1.8 [42]. Each regime of gas-particle interaction is governed by very

different physics which will be elaborated on below.

$$Kn = \frac{2\lambda}{d} \tag{1.7}$$

$$\lambda = \frac{RT}{\sqrt{2}\pi d^2 N_A P} \tag{1.8}$$

The high peak temperature (∼3000 K) results from Bazyn at high pressures suggests that the particles may be undergoing heat transfer in the transition or free molecular regime. A primary objective of the present study is to gain a better understanding of the underlying heat transfer phenomena.

In order for a 100 nm nanoparticle to reach 3000 K it would need to fully combust in less than 1.0 $\mu$s if it assumed that all of the heat goes to heating the particle to a uniform temperature and that heat is lost through convection and radiation to ambient temperature walls. Present results have clearly shown the nominal burn time of nanoparticles to be significantly greater than 1 $\mu$s which supports the well established notion that these particles are burning in the transition or free molecular realm of heat transfer [40]. However, expressions for heat transfer in these regimes with common assumptions also overpredict the heat flux from the particle based on experimental work as will be discussed in greater detail below.

### 1.3.1 Continuum Regime

The continuum regime of heat transfer is treated in a classical approach where the object of interest is much greater in size than the spacing of the ambient gas particles. Knudsen values less than 0.01 generally are considered the onset of the continuum regime of heat transfer, and Knudsen values between 0.01 and 0.1 are considered the slip regime. In the continuum regime the particle is significantly larger than the surrounding molecules and continuum fluid mechanics describing boundary layer theory and heat transfer can be used to determine particle heat transfer because local thermodynamic equilibrium is achieved. In the slip flow regime the continuum hypothesis is valid but local thermodynamic equilibrium is not satisfied near the particle surface and a temperature jump between the gas and surface occurs. For aerosols at atmospheric pressure the continuum treatment applies to particles greater

than twenty microns in diameter and slip flow treatment applies to particles greater than two microns and less than twenty microns.

An analytical solution has previously been obtained from first principles for the heat transfer from a stationary sphere in a fluid. This analysis shows the Nusselt number is equal to 2 under stationary conditions. The Nusselt number is defined as shown in equation 1.9 where $h$ is the heat transfer coefficient and $k$ is the thermal conductivity of the gas. For non-stationary flow over a sphere Levey suggested the empirical relation shown in equation 1.10 which is valid for conditions experienced behind the incident shock flow in the continuum regime [43]. With knowledge of the Nusselt number, particle diameter, and thermal conductivity of the ambient gas, the heat flux from a heated particle to the ambient gas can be calculated using Newton's law of cooling as shown in equation 1.11.

$$Nu = \frac{hd}{k} \tag{1.9}$$

$$Nu = 2 + 0.4Re^{1/2} + 0.06Re^{2/3}Pr^{0.4}\left(\frac{T_f}{T_p}\right)^4 \tag{1.10}$$

$$q = Nu\frac{k}{d}A_s(T_p - T_a) \tag{1.11}$$

The heat flux from a particle in the continuum and slip flow regime is relatively insensitive to the ambient pressure conditions. The only term in equation 1.11 which has pressure dependence is the thermal conductivity of the ambient gas (k) which for air is insensitive to pressure until very low pressures ($\leq$100 Pa). For pressures of consideration in aluminum combustion the thermal conductivity of gases of interest (oxygen, nitrogen, argon) is independent of pressure. This is a stark contrast to the free molecular regime of heat transfer where the heat transfer rate is linearly dependent on pressure.

### 1.3.2 Transition and Free Molecular Regime

Knudsen values greater than 10 are generally considered the onset of the free molecular regime of heat transfer. Knudsen values between 0.1 and 10 are considered a transition regime where neither the continuum regime nor free molecular regime directly applies however interpolation formulae between the

two regimes or quasisteady analytical solutions are commonly used . As the particle size is further decreased to the nano-scale Knudsen numbers may approach the entirely free molecular regime during combustion. A 100 nm particle in air at atmospheric pressure and 2000 K has a Knudsen number of approxiamtely 10. Therefore, for nanoparticle combustion the transition and free molecular regime of heat transfer govern the majority of the heat transfer.

One of the commonly used empirical models for particle heat transfer in the transition regime is shown in equation 1.12 [44]. Where the Nusselt number is inversely related to the Knudsen number. This model has been used by Lynch previously to determine particle heat up time behind the incident shock in the heterogeneous shock tube. However, this correlation has been presently shown to overestimate the heat losses during nano-aluminum combustion as will be discussed later.

$$Nu = \frac{0.3}{Kn} \tag{1.12}$$

It has recently been shown using direct Monte Carlo simulation that the model proposed by Fuch for heat transfer in the transition regime is the most accurate interpolation analytical model [42]. Fuch's model suggests a Langmuir layer surrounding the particle inside which the heat transfer is governed by free molecular regime physics. Outside the Langmuir layer the physics is governed by continuum regime treatment. An iterative process is used to evaluate the temperature at the boundary between the free-molecular layer and continuum surrounding. Dreizin applied this model to the treatment of metal particles in the transition heat transfer regime [21]. In the free molecular regime heat conduction between the gas and particle surface following equation 1.13 where $c$ is the velocity of the gas molecule, $\alpha$ is the energy accommodation coefficient (EAC), and $\gamma$ is the average specific heat ratio as described by Filippov [42].

$$q = \alpha \frac{c\,P}{8\,T_a} \frac{\gamma + 1}{\gamma - 1} (T_p - T_a) \tag{1.13}$$

### 1.3.3 Energy Accommodation Coefficient

Equation 1.13 introduces the EAC which will be discussed in greater detail as it has a significant impact on the heat transfer in the free molecular regime. The energy accommodation coefficient is a fundamental parameter that describes the amount of energy transferred between a gas molecule and a particle surface upon collision as shown in equation 1.14 [45–47]. The numerator indicates the amount of energy transferred upon collision and the denominator indicates the maximum amount of transferrable energy determined by the second law of thermodynamics.

$$\alpha = \frac{E_{g,o} - E_{g,i}}{E_{g,o,max} - E_{g,i}} \tag{1.14}$$

In general the accommodation coefficient is the efficiency of the heat transfer that occurs in the free molecular regime. From a classical collisional theory molecular dynamics point of view two types of collisions may occur between the gas molecule and the surface. The first is an inelastic collision where the potential forces are not great enough to hold the gas molecule near the surface long enough for sufficient kinetic energy transfer. In the second type of collision the potential is large enough for the gas molecule to be physisorbed to the surface for a sufficient time such that the internal and kinetic energy of the molecule are able to fully equilibrate with the surface. The probability of each collision type, and in turn the value accommodation coefficient, is dependent on two primary factors, the ratio of weight between the gas and surface atoms ($\mu$=$\mathrm{m}_g/\mathrm{m}_s$) and the interface potential [48]. It has been suggested in the literature that the probability of the gas molecule collision resulting in a long enough duration for complete energy transfer to occur depends strongly on matching the vibration phase of the surface atom with that of the incident gas molecule [49], which is an implicit function of the molecular mass ratio [48]. This result has been observed in low temperature electron beam experiments which monitor the energy transfer between a lightweight gas (helium) and a heavy surface (tungsten).

Classically there are two approaches to calculating the EAC from theory. The two approaches used to model gas-surface interactions are the classical and quantum-mechanical model [50]. Goodman used the the classical model which suggests each particle is attached by a spring to a fixed lattice [46]. This model gives a simplified understanding of the EAC but in general vio-

lates the discrete nature of the oscillator energy states and does not in general satisfy the principle of detailed balancing which states that at equilibrium each collision process should be equilibrated by the reverse process [50].

The quantum mechanical model of the EAC treats the surface as an ensemble of phonons. This calculation cannot lead to a general solution for gas-surface interaction as is done in the classical solution and in general presents a problem with unitarity at the probability calculation which leads to the exact solution presenting an unsolvable problem [50]. Therefore, in order to obtain a relatively accurate description of the EAC the primary methods have been to measure the value for specific systems as has been done with aerosolized soot particles [51–53].

More recently, computational molecular dynamic simulations have successfully been used to predict the accommodation coefficient [47, 54]; however, these models are highly dependent on the gas/surface interface potentials used in the model, and it is often necessary to validate such models with experimental data before the results can be extended to new particle systems.

Because of the aforementioned reasons the EAC is relatively poorly understood for most systems without direct measurement. The common assumption in unknown systems is that the EAC is unity or close to it, even though there is little evidence to support this value [55]. In fact this assumption was applied by Dreizin and others in various models of small particle aluminum combustion, albeit for micron sized particles [21]. A great deal of research has gone into accurately describing the accommodation coefficient of soot systems. Most results suggest the value to be between 0.18 and 0.5 [56]. The most effective experimental method to determine the EAC is using time resolved laser induced incandescence (TiRe-LII) of a well described particle sample [51, 57, 58].

Relatively little work has been done to describe the accommodation coefficient of metal and metal oxide nanoparticles systems. VanDer Wal has performed preliminary tests and shown the LII method to be sensitive to particle concentration and size with a variety of metal nanoparticles including tungsten, iron, molybdenum, and titanium [59] which opened the pathway for TiRe-LII measurements to be performed on metal systems. LII has since been used by other researchers to measure the accommodation coefficient, size distribution, and concentration of certain metal systems, primarily iron [57, 58]. Kock and Eremin performed 2-color TiRe-LII measurements of

the accommodation coefficient on iron nanoparticles in various gaseous environments. Eremin's results showed the EAC to be 0.01, 0.2, and 0.1 for the Fe/He, Fe/CO, and Fe/Ar systems respectively [57, 58]. These values were significantly lower than those also found by Eremin for carbon systems (0.44-0.51) [60]. Koch's results showed the EAC to be 0.13 for both the Fe/Ar and Fe/$N_2$ system [58]. These results further suggest that the accommodation coefficient may be smaller than commonly assumed for the aluminum/alumina system, yet no experimental measurements have been performed to date.

Theoretical work by Altman suggested that for metallic particles at high particle and ambient temperatures the energy accommodation coefficient may be two orders of magnitude smaller than the values commonly observed for soot [1]. Additional experimental work by Altman et al. was performed using laser irradiation to heat up nanoparticles generated in a flame. The energy accommodation coefficient was found to be near 0.005 which agreed nicely with their theoretical upper limit [50].

Rather than attempt to solve the unsolveable quantum-mechanical solution for the gas surface interface Altman used the principle of detailed balance to derive an upper limit for the EAC [1]. He found that the EAC is bound by an upper limit as shown in equation 1.15 where $\theta$ is the Debye temperature of the solid. This result relies heavily on the Debye temperature as a cutoff above which the particle can no longer accommodate energy transfer. However, it gives a prediction for the accommodation coefficient at high particle and ambient temperatures that are necessary for combustion applications.

$$\alpha_E < \frac{1}{2\frac{C_v}{R} + 1} \frac{\theta^2}{T_g T_s} \tag{1.15}$$

The result by Altman shows that as the particle and ambient temperature increase the upper limit of the accommodation coefficient decreases. The decrease in the accommodation coefficient with increasing particle temperature is generally well accepted. As the particle temperature increases the probability of the gas molecule being physisorbed to a surface for a sufficiently long time such that the internal and kinetic energy of the molecule is able to fully equilibrate with the surface is decreased.

The effect of ambient gas temperature on the accommodation coefficient is less certain. The result by Altman in equation 1.15 suggests that as the ambient gas temperature increases the upper limit of the accommodation co-

efficient will correspondingly decrease. This is contrary to the result derived by Goodman from lattice theory considering simplified gas-surface scattering interactions [46]. In the simplified lattice model the result showed that in all cases the accommodation coefficient initially decreased as ambient temperature increased until reaching a minimum value, $\alpha_{min}$. As the temperature increased further the accommodation coefficient asymptotically increases toward a steady value $\alpha_{\infty}$, slightly higher than $\alpha_{min}$. In the assumption of lattice theory which relies on a lattice model with highly simplified atomic force laws the shape of this curve is similar for all gas/surface interactions as shown in Figure 1.3.

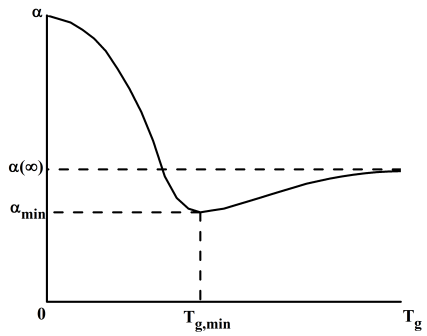


**Figure 1.3: Energy accommodation coefficient dependence on ambient gas temperature. Figure reproduced from Goodman [46]**

Relatively little work has investigated the dependence of the accommodation coefficient on temperature beyond the work performed by Altman. Michelsen attempted to derive a particle and gas temperature dependence for the accommodation coefficient using molecular beam data from Hager, Walther, and coworkers for the interaction of NO with graphite surfaces to be applied to soot particles [61]. Michelsen found an exponential decrease in the accommodation coefficient with increasing particle temperature. The data sets were not complete enough for the NO/graphite system to generate an overall accommodation coefficient as a function of the gas temperature. Michelson attempted to estimate the effect by extending the values of the data set using linear extrapolation but little evidence support this method outside of the chosen data-set. Using this extrapolation it was found that the accommodation coefficient decreased with increasing temperature at gas temperatures below 1650 K and increased with increasing gas temperature

above 1650 K.

Altman's prediction would suggest that for combusting nano-aluminum particles the accommodation coefficient will be sufficiently small ($\sim$0.005) at high temperatures. This result has significant implications for nano-aluminum combustion where transfer of heat to the ambient gas is desired. If the accommodation coefficient is significantly small radiation becomes a more signficant heat transfer pathway.

## 1.4 Emissivity of Nano-aluminum

Relative emissivities of metal oxides are commonly used while performing pyrometric temperature measurements of high temperature particles. Pyrometry is used to determine the temperature of a condensed phase particle by measuring the radiant intensity at two or more wavelengths and fitting the relative intensities to a Planck's distribution as is shown in Equation 1.16 for two wavelengths. In Equation 1.16, $h$ is the Planck constant, $c$ is the speed of light, $k$ is the Boltzmann constant. The two wavelengths are denoted by $\lambda_1$ and $\lambda_2$, and $S_p$ stands for the detected emission at each wavelength. $S_{bb}$ is the measured signal from a black body lamp at temperature $T_{bb}$ used for calibration, and $\epsilon_p$ refers to the particle emissivity. By using the effective temperature the measurement is no longer sensitive to the absolute intensity measurements, and calibration of the collection optics is not necessary. Calibration using a known blackbody temperature $T_{bb}$ source is necessary to measure $S_{bb}$ at each wavelength [58].

$$T_p = \frac{hc}{k}\left(\frac{1}{\lambda_2}-\frac{1}{\lambda_1}\right)\left[ln\left[\frac{S_p(\lambda_1,T_p)S_{bb}(\lambda_2,T_p)\epsilon_p(\lambda_2)}{S_p(\lambda_2,T_p)S_{bb}(\lambda_1,T_p)\epsilon_p(\lambda_1)}\right]+\frac{hc}{kT_{bb}}\left(\frac{1}{\lambda_2}-\frac{1}{\lambda_1}\right)\right]^{-1} \tag{1.16}$$

When performing the calculation it is necessary to have an accurate value for the ratio of spectral emissivities ($\epsilon_p(\lambda_2)/(\epsilon_p(\lambda_1))$ at the two given wavelengths. Significant work has been conducted on evaluating the emissivity of bulk alumina [62], but the optical properties of small particles are not necessarily the same [63]. Furthermore, only a limited amount of work has been reported at high temperatures relevant to aluminum combustion ($\sim$ 3000

K). Since little explicit data are available, researchers have had to assume functional forms of $\epsilon_p(\lambda)$, and the choices vary significantly. Authors in the past have used various wavelength assumptions including $\epsilon_p(\lambda_2)/\epsilon_p(\lambda_1)$ being equivalent to a constant, $\lambda_1/\lambda_2$, and $\lambda_1^2/\lambda_2^2$ [64,65]. Lynch et al. demonstrated that using the wrong assumption may lead to errors ranging from hundreds of Kelvin to over 1000 K [65].

Previous work by Lynch and later Kalman using shock heated particles in an inert environment investigated the emissivity ratio at various ambient temperatures between 2500-3500 K [65,66]. The initial work by Lynch investigated the relative emissivity without direct knowledge of the optical depth. Kalman later showed the optical depth can have a significant influence on the observed emissivity ratio in certain cases. It was found that the emissivity ratio of nano-aluminum was relatively constant in the temperature range between 2500-3500 K. The emissivity dependence was shown to be $\lambda^{-1.2}$ which is close to the value predicted by Rayleigh scattering.

Lynch was not able to extend the spectral emissivity temperature range below 2500 K due to limitations of the detection sensitivity used in their experiments. For nano-aluminum it is necessary to extend the knowledge of the relative emissivity to temperatures below 2300 K because ignition can occur at temperatures as low as 1500 K. Extrapolation to lower temperatures is highly uncertain, especially due to the fact that nano-aluminum will undergo a phase change below 2300 K to a solid alumina particle surface. Without direct measurement extending the emissivity assumption through to temperatures below the melting point of alumina is highly uncertain and is not easily justified.

In order to accurately apply pyrometry techniques to nano-aluminum combustion it was necessary to directly measure the wavelength dependence of the emissivity at the wavelengths used for pyrometry and at temperatures down to 1500 K. These measurements were performed in addition to the combustion diagnostics in order accurately interpret the pyrometry data obtained during shock tube experiments.

## 1.5 Objectives

The preceding review has shown that there are significant remaining questions regarding nano-aluminum based energetic material combustion. The objective of this study is develop a better understand of the underlying combustion and heat transfer phenomena which occur during nano-aluminum combustion.

These issues are addressed through a series of shock tube tests that have been performed to measure the nano-aluminum particle temperature, burn rate, and emission spectra. From this information we can deduce the primary combustion mechanism and heat transfer phenomena under highly controlled conditions. These measurements are performed using high speed optical diagnostics such as pyrometry, spectroscopy, and photometry. From these measurements we can deduce transient combustion properties under various ambient environments.

The experimental data on burning time and temperature are supported by a simple model of nano-aluminum combustion that employs as few limiting assumptions as possible, focusing only on the energy balance leading to particle temperature rise. For ultrafine particles, classical theory predicts that rapid heat transfer results in combustion temperatures that only minimally exceed the ambient temperature, even when common Knudsen number correlations are used for Nusselt number calculation [44]. It is not until the energy accommodation coefficient approaches values less than 0.01 that significant temperature rises are observed. The prediction of the particle temperature requires specification of the reaction rate (i.e. heat release rate) in addition to the heat transfer coefficient. Multiple heat transfer models are considered to determine the predicted transient particle temperature and to see if the nano-aluminum particle experiences thermal isolation from the surrounding gas.

Laser induced incandescence is used to obtain a value for the accommodation coefficient that is decoupled from an assumed combustion mechanism. To date no previous measurements have been made on the accommodation coefficient that is relevant to aluminum combustion. The present data will allow for future modeling with appropriate values for the heat transfer from the particle. This information is critical in the modeling and evaluation of systems using nano-aluminum as an energetic material and without this

information heat transfer estimates may be off by orders of magnitude.

Constant volume combustion measurements are used to obtain a macroscopic estimate of the heat transfer that occurs via radiation and condution. Ignition of nano-aluminum particles occurs in a lean mixture of hydrogen which is ignited and subsequently ignites the aluminum nanoparticles with excess oxygen. From the pressure rise the amount of energy that is transferred via conduction can be estimated. This experiment is representative of enhanced blast conditions and will give a good understanding of the effect free molecular regime heat transfer has on the macroscopic event.

The following specific objectives will be addressed in the subsequent chapters:

- Characterize the burn time behavior of various size nano-aluminum particles with the objective to:
  - Find the effect of pressure on the particle burn time. It is expected that in the diffusion limit pressure will have an insignificant effect on particle burn time while in the kinetic limit pressure will have a linear effect on particle burn time.
  - Find the effect of ambient temperature on the partricle burn time. In the kinetically limited and solid state diffusion limited regimes of combustion the ambient temperature has a signficant effect on overall burn time
  - Find the effect of particle size on the ambient burn time. The diameter dependence gives insight into the rate limiting step of the combustion process.
- Characterize the particle temperature during combustion with the objective to:
  - Find the effect of pressure on the particle temperature. It has been shown previously that at high pressures the peak particle temperatures are well above ambient which is unexpected. Characterizing this phenomena will give a better understanding.
  - Find the effect of ambient temperature on the particle temperature. Observing the effect of ambient temperature on particle

temperature will characterize if a shift in the combustion mechanisms may occur.

  - Analyze the measurements for indications of the flame structure and limiting processes

- Create a combustion and heat transfer model with the objective to:

  - Accurately predicts the combustion phenomena that is observed in the shock tube experiments
  - Investigate the mechanism of heat transfer in the free-molecular regime using common heat transfer expressions in order to determine the appropriateness of various heat transfer models.

- Perform Laser Induced Incandescence measurements on nano-alumina particles with the objective to:

  - Quantify the energy accommodation coefficient of nano-alumina particles in various environments and pressures
  - Extrapolate and apply the measured accommodation coefficient values to nanoparticle systems and conditions of interest
  - Compare results with competing energy accommodation coefficient calculations in literature. Apply to heat transfer model.

- Measure the relative emissivity of nano-aluminum particles in inert environments with the objective to:

  - Determine the relative emissivity relationship at wavelengths of interest at various temperatures. This can be used to determine if the phase change has a significant impact on the emissivity assumption.
  - Apply the measured emissivity relationship to pyrometry measurements used in the shock tube and laser induced incandescence measurements for accurate interpretation of results.

- Perform constant volume combustion measurements of nano-aluminum particles burning in a lean mixture of hydrogen and oxygen with the objective to:

- Determine the ambient pressure rise due to heat release during nano-aluminum combustion. Obtain an estimation of the energy released due to radiation compared to conduction in the ambient gas.
- Determine the extent of particle combustion by collecting condensed products for analysis.
- Compare results to various energy accommodation coefficient results in order to give an order of magnitude estimation on the amount of energy lost via radiation and conduction.

# CHAPTER 2

# EXPERIMENTAL METHODS

The experimental methods used to study the combustion and heat transfer phenomena of nano-aluminum are described in detail below. The shock tube facility has been in operation since the early 1990's under the advisement of Professor Herman Krier, Professor Rodney Burton, and Professor Nick Glumac. It has been detailed in multiple previous publications [37, 67, 68] with various improvements upon each iteration, most recently by Lynch [69]. The laser induced incandescence measurements were performed in a separate small volume chamber that was adapted for the specific purpose. The same small volume chamber was used for the constant volume combustion measurements. The design and operation of each experimental set-up is discussed in detail below. This discussion is followed by a detailed description of the diagnostics, setup, and instrumentation implemented in the experiment to make the ignition, combustion, pressure, temperature, and heat transfer measurements.

## 2.1 Shock Tube Measurements

High temperature shock tube measurements were used to measure the burning time, particle temperature, and emission spectra of burning aluminum nanoparticles. The nanoparticles were obtained from four different manufacturers with nominal sizes of 18, 50, 80, and 110 nm. Each sample had a significant size distribution, and the particles are described in greater detail in Section 2.5. A parametric study was performed by measuring the combustion parameters of the nominally 50 nm particle while varying the ambient temperature, pressure, and oxidizing environment. Four tests were run at each condition. Table 2.1 shows the parametric study outline used while performing the shock tube measurements. In addition to varying the

ambient environment, tests were run in select conditions while varying the particle sample to include tests using the 18, 80, and 110 nm particle samples.

**Table 2.1: Test matrix used in parametric study**

| Particle Size (nominal) | Environment | Temperature (K) | Pressure (atm) |
|---|---|---|---|
| 50 nm | Air | 1500 | 10 |
| 50 nm | Air | 2000 | 10 |
| 50 nm | Air | 2500 | 10 |
| 50 nm | Air | 1500 | 20 |
| 50 nm | Air | 2000 | 20 |
| 50 nm | Air | 2500 | 20 |
| 50 nm | Air | 1500 | 30 |
| 50 nm | Air | 2000 | 30 |
| 50 nm | Air | 2500 | 30 |
| 50 nm | 20% $CO_2$ - 80 % Ar | 1500 | 10 |
| 50 nm | 20% $CO_2$ - 80 % Ar | 2000 | 10 |
| 50 nm | 20% $CO_2$ - 80 % Ar | 2500 | 10 |
| 50 nm | 20% $CO_2$ - 80 % Ar | 1500 | 20 |
| 50 nm | 20% $CO_2$ - 80 % Ar | 2000 | 20 |
| 50 nm | 20% $CO_2$ - 80 % Ar | 2500 | 20 |
| 50 nm | 20% $CO_2$ - 80 % Ar | 1500 | 30 |
| 50 nm | 20% $CO_2$ - 80 % Ar | 2000 | 30 |
| 50 nm | 20% $CO_2$ - 80 % Ar | 2500 | 30 |
| 18 nm | Air | 1500 | 20 |
| 80 nm | Air | 1500 | 20 |
| 110 nm | Air | 1500 | 20 |
| 18 nm | 20% $CO_2$ - 80 % Ar | 2000 | 20 |
| 80 nm | 20% $CO_2$ - 80 % Ar | 2000 | 20 |
| 110 nm | 20% $CO_2$ - 80 % Ar | 2000 | 20 |

### 2.1.1 Shock Tube Operation

The details of shock tube theory are well understood and can be found in entire texts devoted to the subject [70–72]. The facility at the University of Illinois, Urbana-Champaign is termed a heterogeneous shock tube due to the fact that it contains a mixture of gases and condensed phases. The shock tube is capable of generating highly controlled elevated temperature and pressure conditions with various oxidizers. Previously, micron sized aluminum has been the primary condensed phase investigated in the facility using $H_2O$,

$CO_2$, and $O_2$ as oxidizers [32, 69]. The shock tube has a converging section to accelerate the shock speed and uses a duel diaphragm burst methodology. The driver section has a 16.5 cm inner diameter and is 3.05 m long. The driven section has an 8.9 cm inner diameter and is 8.38 m long. Figure 2.1 shows a schematic of the shock tube.

In short, the shock tube is used to generate an elevated temperature and pressure environment behind the incident shock which is then further elevated behind the shock that is reflected off of the end wall. The shock is driven by high pressure helium. Upon diaphragm rupture, the shock coalesces and propagates down the length of the tube in the oxidizing environment. The temperature and pressure of the driven gas is risen very rapidly behind the incident shock. Temperatures between 1000-4000 K and pressures between 1-40 atm are achievable in the shock tube by varying the driven section and driver section pressures. Temperature, pressure, and oxidizing environment can be changed nearly independently of one another.

The particles are injected immediately before diaphragm rupture. As the shock travels through the particles, they are swept towards the end wall and exposed to the incident shock ambient conditions. The shock then reflects off of the end wall and again travels through the particles. The particles are immediately stagnated very near the end wall where they burn in the elevated reflected shock conditions during the test time.

The test time behind the reflected shock in the shock tube refers to the duration of time between the moment the incident shock hits the endwall and the moment the same shock wave hits the end wall again after reflecting off of the contact discontinuity. The test time depends on the shock velocity, but is typically $\sim$2 ms in the facility described. During the test time the particles and oxidizing environment are relatively stagnant, and the temperature and pressure of the gas are accurately known from the shock relations. After the test time the ambient conditions can no longer be accurately described. Behind the reflected shock the ambient gas and particles stagnate rapidly. Larger particles with more momentum take longer to completely stop behind the reflected shock, but the particle cloud is typically on the order of 2-4 cm wide in the axial direction.

The test time and ambient conditions are determined by measuring the shock speed velocity using four piezoelectric pressure transducers. Figure 2.2 below shows an example of the transient pressure profiles used to calculate

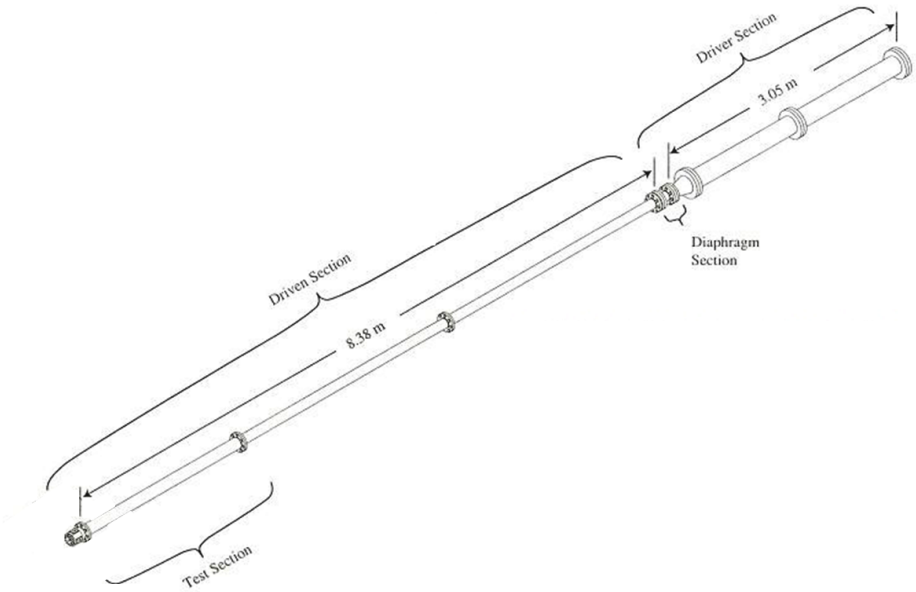


**Figure 2.1: Schematic of shock tube**

the velocity. The distances between each transducer are accurately known, and the pressure trace gives four very decisive time of arrival measurements. Using this information, three velocities can be calculated for the midpoints between the four pressure transducers. The velocity decreases slightly ($\sim$10 m/s) as it progresses towards the endwall due to friction. This trend is fit to a first order approximation, and the endwall velocity is determined. Using the velocity, initial driven pressure, and initial temperature the incident and reflected shock parameters are calculated using the Gordon-McBride equilibrium calculation.

The particles are radially injected into the shock tube using a pneumatically driven piston. Approximately 1-5 mg of powder is loaded into the particle loading insert. Injecting this amount of powder ensures that particle spacing within the test environment is large enough such that each particle burns independently of others. The pneumatic ram is triggered electronically. The ram slides down cylinder toward the powder loading insert which is locked into place with a set screw. The powder becomes entrained in the rapid flow traveling from the injector body through the powder insert. The flow travels into the shock tube through a 60 $\mu$m mesh that further disperses

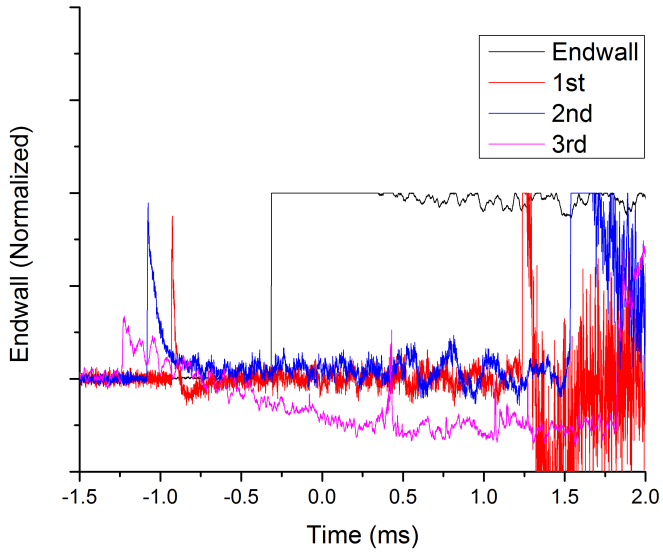


**Figure 2.2: Transient pressure trace used to calculate the incident shock velocity**

the powder upon entry. The powder remains suspended in the test gas until shock passage due to the small particle size. A previous study has shown that the cross injection system provides a reasonably dispersed particle cloud with some shock tube wall impingement [32]. The particles that impinge upon the shock tube wall do not end up in the test section due to wall drag, and therefore do not affect measurements. The driven gases are mixed in a mixing tank prior to filling the shock tube. The gases are allowed to mix while the shock tube is being vacuumed down. After purging the shock tube with the mixture to be used in the test the shock tube is vacuumed, the gases are filled, and the shock tube valve is closed.

A fiber optic end section was used for the present combustion experiments within the shock tube as shown in Figure 2.3. This end section is ideal for burning time measurements due to the many axial measurement locations. Spatial resolution is important for burning time measurements due to particle motion behind the reflected shock, therefore. Light collected through the sapphire endwall viewport was used in order to perform pyrometry and spectroscopy measurements as will be discussed in greater detail in the following section.

A different sapphire viewport end-section was used for the emissivity mea-

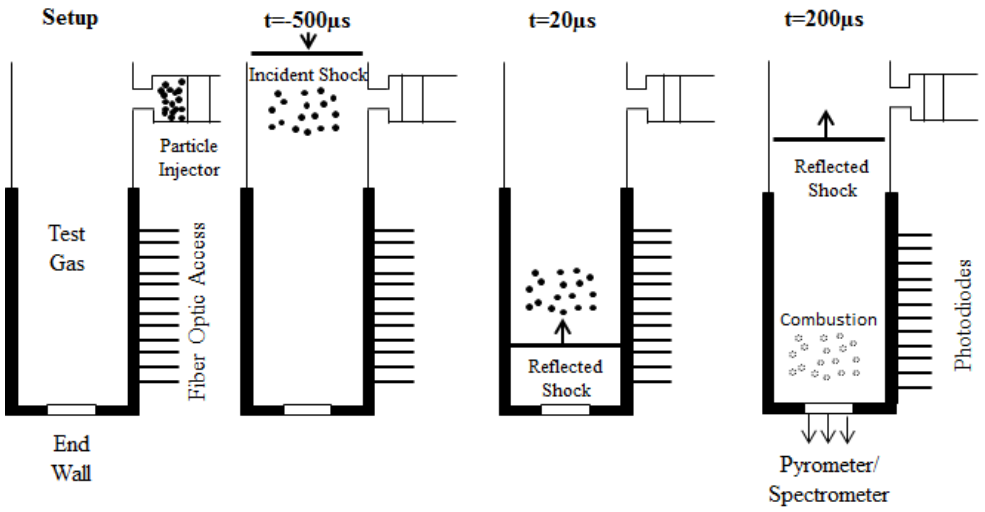


**Figure 2.3: Schematic of shock tube with radial injection and fiber optic end section (top view)**

surements which allowed greater optical access within a given axial location. This was necessary due to the desire to measure the optical depth using laser extinction orthogonally to the detection of particle radiation. A schematic of the sapphire end-section can be seen in Figure 2.4.

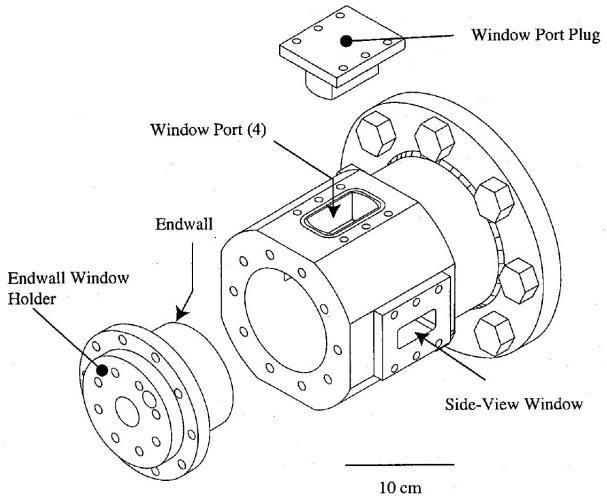


**Figure 2.4: Schematic of shock tube sapphire end-section with greater orthogonal optical access**

### 2.1.2 Emission Spectroscopy

Emission spectroscopy is primarily used to determine the intermediate gas phase species emitted in these unknown systems. Not all gas phase species emit detectable banded structures, but those that do create diagnostic opportunities. AlO is a notable example which is has been used in aluminum combustion previously [32, 69]. Emission requires that the molecule release light energy and transition to lower energy level. The amount of detectable spontaneous emission depends on multiple variables including temperature, concentration, and radiative lifetime. In this study we investigate the emission spectroscopy of the nano-aluminum particles.

The emission is collected using multiple spectrometer arrangements depending on the resolution desired. A custom f/9 444mm focal length spectograph with a 30 micron inlet slit was used with a 1200 gr/mm grating was used to obtain 0.1 nm resolution. A TRIAX 190 mm focal length spectrometer with a 300 gr/mm grating was used to obtain lower resolution spectra ($\sim$2 nm) over the entire visible range. The gratings were changed to obtain the desired resolution and wavelength range. Each spectograph is coupled to a Hamamatsu S7010-1007 back thinned CCD detector that has 128 x 1044 pixels 26 $\mu$m square. The signal is vertically binned in order to increase signal to noise ratio. The spectrum is also integrated over the entire test time. Post test emission is blocked using a Uniblitz shutter which is timed to fully close immediately after the test time.

Dark signals are taken with the same exposure time and the same conditions as during the test without combustion emission. The dark image is used to remove the contribution of stray light to the test. Emission spectra were predominantly wavelength calibrated using a Ne calibration lamp for wavelength ranges greater than 500 nm. Other calibration sources including a mercury lamp, iron hollow cathode lamp, aluminum hollow cathode lamp, and a nickel hollow cathode lamp, were used as needed. Atomic line peaks are found using OriginLab peak finding software by fitting them to a Voigt profile. Once the peaks are found they were matched to specific wavelengths, and the wavelength vs. pixel relationship is fit to a $2^{nd}$ order polynomial. Typically five peaks are fit for each wavelength calibration.

Intensity calibration is accomplished using an Oriel 6319 tungsten calibration lamp and fitting it to a blackbody distribution over the known spectral

range. The Oriel tungsten calibration lamp emits at a color temperature of 3200 K. During intensity calibration, the tungsten lamp is placed near the center of the shock tube in order to best represent the emission during the combustion event.

### 2.1.3 Photometry

Burning time measurements are made using Thorlabs PDA36A photodiodes and the fiber optic shock tube end section as shown in Figure 2.5. The fiber optic test section allows optical access to multiple axial locations. The test section utilizes 1.5mm TEQS coated silica multimode fibers to provide optical access. The fibers are epoxy-mounted through the center of 1/4"-20 cap screws that are o-ring sealed. The spacing between each cap screw is 3/8". Each fiber has a field of view of 0.25" in the center of the shock tube such that each fiber is observing emission from an isolated axial location.

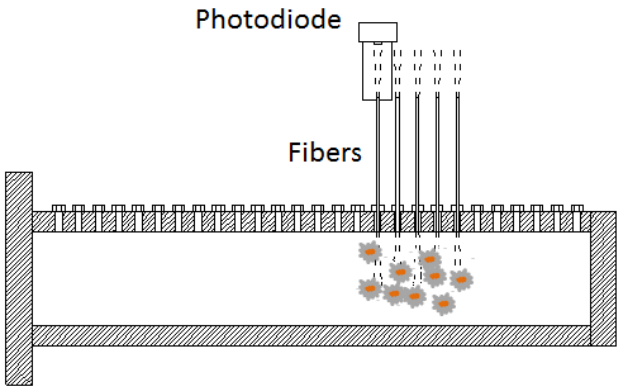


**Figure 2.5: Photometry set-up using fiber-optic end section**

The photodiodes are unfiltered for nano-aluminum combustion. It was previously found by Lynch [39] that there is little gas phase emission during combustion, and therefore it was not necessary to filter the emission in a specific wavelength range as is done in larger aluminum particle combustion. In larger aluminum particle combustion the emission is often filtered around the AlO B-X emission band. When the emission is filtered around a gas

phase emission band the luminosity is correlated to the presence of AlO gas phase intermediate species. In the present set-up, the luminosity is correlated to thermal emission because no gas phase species are present. Luminosity is correlated to burn time through temperature.

The burn time is processed using the 10%-90% area burn time method. An illustration of the calculation is shown in Figure 2.6. A background intensity level is subtracted off the intensity curve prior to integration to account for emission non-combusting condensed phase product alumina particles. A linear interpolation is used to to go from the initial background level to the late time background level which peaks at the point of peak intensity. Integration is then performed on the intensity curve with the background subtracted. The burn time is measured as the time when 10% of the curve has been integrated to the time when 90% of the curve has been integrated.

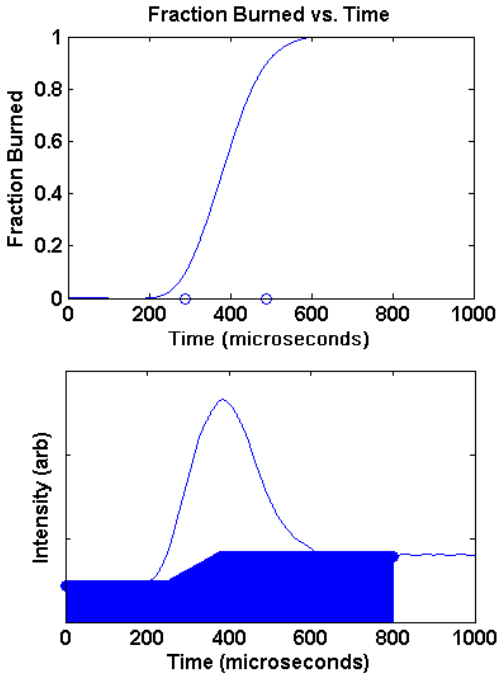


**Figure 2.6: Sample burn time calculation using the 10%-90% area burn time method**

### 2.1.4 Pyrometry

A 3-color pyrometer previously used for aluminum combustion systems is used to measure the condensed phase temperature within the system [69]. The pyrometer consists of a fiber bundle that collects light from the combustion event through a slit. The cable trifurcates the light into three channels; the light from each channel is passed through an interference filter and onto a photomultiplier tube (PMT). The interference filters are centered at 705, 826, and 905 nm with 10 nm bandpass width. The shorter wavelengths are monitored using a Hamamatsu R928 photomultipliers and the 905 nm wavelength is monitored by a Hamamatsu R636-10 photomultiplier with an IR sensitive GaAs photocathode.

The same pyrometric technique was used to both monitor the particle temperature during combustion and during laser induced incandescence measurements. During shock tube combustion measurements all three wavelength ranges were used in order to determine a 3-color pyrometry temperature. During laser induced incandescence experiments only two channels were used due to limitations in the number of high speed oscilloscope channels available. Therefore, during LII experiments only the 705 and 826 nm wavelengths were used in order to determine a 2-color pyrometry temperature. In order to determine the 3-color pyrometry temperature during combustion measurements the three wavelengths were fit using a custom Matlab script to the best fit Planck's distribution with the emissivity assumption determined from emissivity measurements and discussed later in the results section.

The system is calibrated using an Oriel 6319 tungsten lamp. This lamp has a known spectral output similar to a 3200 K blackbody. A Uniblitz shutter is placed between the tungsten lamp and pyrometer during calibration and is pulsed to open and close in under 1 ms to obtain a temporal response similar to the actual test. Outputs of the photomultipliers are amplified using a Stanford Research Systems Quad preamplifier unit with a 300 MHz bandwidth. The time response of the pyrometry system is sub-microsecond. The system is calibrated using tungsten a calibration lamp. Noise level is typically 5-10% of the signal and, the measurement uncertainty has previously been estimated to be $\pm$150 K [73]. Averaging over 10 $\mu$s can reduce the noise contribution to a few percent and repeatability is better than 2%.

Planck's law is shown in Equation 2.1 and is used to fit a temperature

to the distribution of intensity with wavelength as was discussed previously. From 2.1 it is evident that at a specific wavelength the emissive power is exponentially dependent on temperature. The overall emitted intensity at all wavelengths is proportional to $T^4$. Therefore, it is commonly assumed that the measured pyrometry temperature is indicative of the peak temperature within the collection volume of the optical measurement.

$$E(\lambda, T) = \epsilon(\lambda) \frac{C_1 \lambda^{-5}}{e^{C_2/\lambda T} - 1} \tag{2.1}$$

The condensed phase dominates the emission where molecular emission is absent because the emissivity of condensed phases is much greater than that of gases. Pyrometry is also a spatially averaged measurement, therefore the observed temperature is not a true single particle temperature but a convolution of the particle temperatures within the collection volume that is weighted exponentially by each particle temperature at that given moment in time. In the shock tube, the particles in the dilute mixture burn independently of one another.

## 2.2 Emissivity Measurements

The emissivity measurements were performed in the shock tube similarly to the combustion measurements but instead used inert nano-alumina particles further described in section 2.5.2 injected into air. The particles were heated behind the reflected shock of the shock tube to a known temperature, and the radiation from the heated particles was monitored using the pyrometer previously described in section 2.1.4 with a tri-furcated cable directing light collected through the sapphire end-section into three independent segments which pass through a bandpass filter at either 705, 826, or 905 nm before being detected on a photomultiplier tube.

Lynch used the same shock tube method for heating the nano-alumina particles previously in order to determine the emissivity dependence on wavelength [65]. Lynch collected the thermal radiation through a spectograph onto a Hamamatsu back-thinned CCD in a similar manner to that discussed previously in section 2.1.2 and used to monitor gas phase emission during combustion. This method was suitable for measurements of emissivity wave-

length dependence at particle temperatures down to approximately 2500 K. At temperatures below 2500 K the signal to noise ratio became too large to accurately fit the spectra to a blackbody curve. This was not an issue for micron size particles because micron size aluminum particles do not ignite until the ambient temperature is 2300 K. Nanoparticles, however, ignite at temperatures as low as 1500 K, and therefore the emissivity assumption must be extended to lower temperatures for the present experiments. This is further necessitated due to phase change will likely occur below 2300 K from liquid to solid which may dramatically alter the emissive properties of the material.

In order to extend the method used by Lynch of measuring the emissivity or shock heated particles to lower temperatures the aforementioned pyrometer was used to collect the radiation rather than a spectrometer. The pyrometer is significantly more sensitive to the thermal radiation due to the larger collection area and wavelength range of the photomultplier and bandpass filter combination. The drawback is that the wavelength dependence is fit to the three discrete wavelengths of the bandpass filters (705, 826, 905) rather than the entire wavelength range as was done by Lynch.

It was shown by Kalman that optical depth has a significant effect on the measured wavelength dependence of the emissivity. For this reason, the optical depth was measured in these tests using laser extinction. A 1 mW Melles-Griot helium-neon laser (632.8 nm) beam was propagated perpendicular to the optical collection of radiation onto the trifurcated cable of the pyrometer. The laser intensity was recorded by a ThorLabs PDA36A photodiode after it was passed through a 632 nm (1 nm FWHM) interference filter as was done by Kalman [66].

The experimental set-up for the emissivity is shown in Figure 2.7. The set-up is calibrated similarly to pyrometry measurements with a Oriel tungsten lamp at 3200 K. Extreme care is taken to diffuse using an engineered diffuser from ThorLabs which created a near Lambertian intensity distrubtion inside the shock tube during calibration. This method decreases the dependence of the calibration on the source position and direction.

The data were compared to the predicted blackbody emission at the temperature determined by the shock velocity relationship within the shock tube and multiplied by the spectral response of the pyrometer at each wavelength. This functional dependence of emissivity with wavelength (e.g. $F(\lambda)$) is cal-

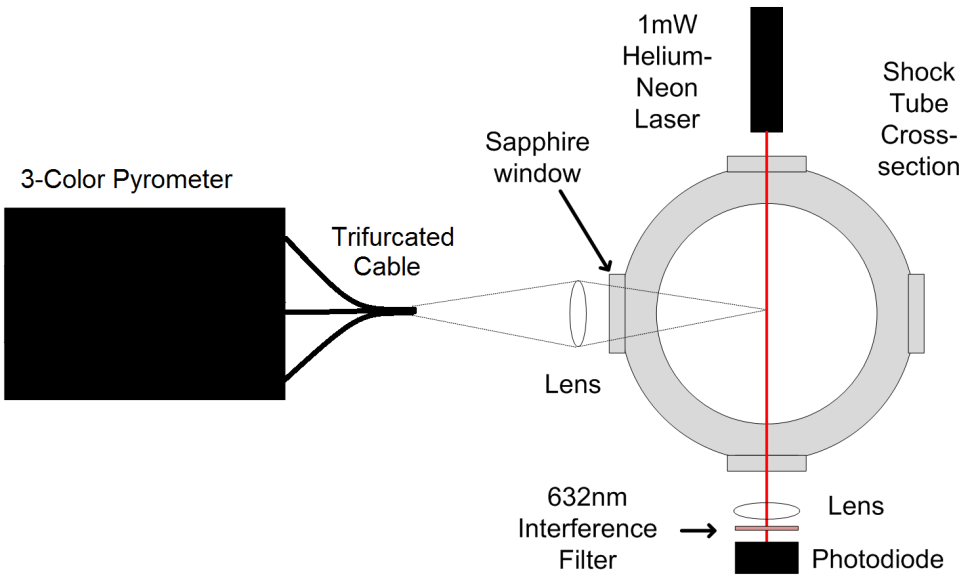


**Figure 2.7: Diagram of emissivity measurement set-up in heterogeneous shock tube**

culated using Equation 2.2 where $I_{exp}$ is the intensity measured during experiment at a given wavelength, $I_{exp,bb}$ is the intensity calculated from Planck's law at a given wavelength and the experimental test temperature, $I_{cal,bb}$ is the intensity calculated from Planck's law at a given wavelength and the calibration black body (3200 K) temperature, and $I_{cal}$ is the measured intensity from the black body calibration source.

$$F(\lambda) = \frac{I_{exp}}{I_{exp,bb}} \frac{I_{cal,bb}}{I_{cal}} \tag{2.2}$$

Using this method the absolute irradiance is never measured, and therefore the absolute emissivity is never measured. Instead the measured emissivity is related to the true emissivity within a multiplicative constant. In pyrometry applications it is the scaling of the emissivity that is important, and thus the data were fit to a power law as shown in Equation 2.3.

$$\epsilon(\lambda, T) = C\lambda^{n(T)} \tag{2.3}$$

## 2.3 Time-resolved Laser Induced Incandescence

In time resolved laser induced incandescence (TiRe-LII) a short laser pulse heats aerosolized nanoparticles of a sample volume and the resulting incandescence is monitored. The heat transfer of the particles can be modeled, and with a known accommodation coefficient, the particle size and volume fraction can be determined. Inversely, if the accommodation coefficient is unknown but the particle size distribution is known, the method can be used to measure the accommodation coefficient. Using time-resolved laser induced incandescence on a well characterized particle sample is the most common experimental way to measure the energy accommodation coefficient [58, 60, 74].

### 2.3.1 TiRe-LII Method

TiRe-LII can be used to measure the accommodation coefficient by monitoring a single wavelength band of light (monochromatic) [74] or by using two or more separate bands in order to perform pyrometry [57]. It is possible to model the monochromatic incandescence signal at a given wavelength using Equation 2.4 where $C_{abs,\lambda}(\lambda, d_p)$ refers to the absorption cross section given in Equation 2.5 [47]. The particle sizes are assumed to obey some probability density function $P(d_p)$, and spectral emissive power $E_{b,\lambda}$ is given by Planck's function. The term $C_\lambda$ is an experimental parameter that is dependent on the particle volume fraction and detection optics and must be found by calibrating the incandescence signal, which can be difficult and often leads to uncertainty.

$$J_\lambda(t) = C_\lambda \int_0^\infty P(d_p) C_{abs,\lambda}(\lambda, d_p) E_{b,\lambda}[T_s(d_p, t), \lambda] \mathrm{d}d_p \tag{2.4}$$

$$C_{abs,\lambda}(\lambda, d_p) = \mathrm{Im}\left[\frac{m_\lambda^2 - 1}{m_\lambda^2 - 1}\right] \frac{\pi^2 d_p^3}{\lambda} \tag{2.5}$$

Two color TiRe-LII measures an effective temperature by relating the ratio of intensity at two monochromatic wavelengths to a Planck's function distribution with an emissivity ratio assumption as shown before in Equation 1.16 and restated below in Equation 2.6. In Equation 2.6, $h$ is the Planck constant, $c$ is the speed of light, $k$ is the Boltzmann constant. The two wave-

lengths are denoted by $\lambda_1$ and $\lambda_2$, and $S_p$ stands for the detected emission at each wavelength. $S_{bb}$ is the measured signal from a black body lamp at temperature $T_{bb}$ used for calibration and $\epsilon_p$ refers to the particle emissivity. By using the effective temperature the measurement is no longer sensitive to the absolute intensity measurements, and calibration of the collection optics is not necessary. Calibration using a known blackbody temperature $T_{bb}$ source is necessary to measure $S_{bb}$ at each wavelength [58].

$$T_p = \frac{hc}{k}\left(\frac{1}{\lambda_2} - \frac{1}{\lambda_1}\right)\left[ln\left[\frac{S_p(\lambda_1, T_p)S_{bb}(\lambda_2, T_p)\epsilon_p(\lambda_2)}{S_p(\lambda_2, T_p)S_{bb}(\lambda_1, T_p)\epsilon_p(\lambda_1)}\right] + \frac{hc}{kT_{bb}}\left(\frac{1}{\lambda_2} - \frac{1}{\lambda_1}\right)\right]^{-1} \tag{2.6}$$

By measuring the effective temperature of the particles the accommodation coefficient can be calculated using Equation 6 which shows particle heat loss due to conduction, radiation, and volatilization [48]. Some consideration must be given to the evaporation term where $h_v$ is the enthalpy of vaporization per atom, $n_v$ is the molecular number flux which is dependent on the vapor pressure, and $c_v$ is the thermal speed of the gaseous molecules. Alumina particles do not strictly evaporate from $Al_2O_3$ liquid to vapor but rather volatilize primarily to AlO and O molecules and atoms as is discussed by Glassman [30]. Therefore, it is difficult to model the evaporation term, and thus the goal of our approach is to measure the thermal incandescence at temperatures where the volatilization term is negligible.

$$\begin{aligned} \rho c_p \frac{\pi d_p^3}{6}\frac{dT_p}{dt} = -\pi d_p^2 \frac{\alpha_E P_g c_g}{8T_a}\frac{\gamma+1}{\gamma-1}\big(T_p - T_a\big) - \\ \int_0^\infty \pi d_p^2 Q_{abs,\lambda}\pi I_{b,\lambda}[T_s(d_p,t),\lambda]\mathrm{d}\lambda - \Delta h_v \frac{\pi d_p^2}{4} n_v c_v \end{aligned} \tag{2.7}$$

### 2.3.2 Experimental Set-up

In the present experiments the fundamental beam of a Quantel Brilliant Nd:YAG laser was used to rapidly heat nano-alumina particles, and the incandescence of the nanoparticles was monitored using a 2-color TiRe-LII set-up. The 2-color TiRe-LII set-up consisted of an f/2 collection lens focusing the particle incandescence onto a bifurcated fiber optic. The fiber optic

split the incoming light into two separate paths; the light from each path passed through a narrow range band pass filter centered at differing wavelengths and was collected on a Hamamatsu R928 photomultiplier tube. The signal from the Hamamatsu R928 photomultiplier tubes was amplified using a Stanford Research Systems Quad pre-amplifier with a 300 MHz band-width and collected using a Lecroy 9360 300 MHz oscilloscope. The two band pass filters had a center wavelength of 705 and 826 nm respectively. Each band pass filter had a full width half maximum transmission range of 10 nm. These wavelengths were chosen because they have previously been used to monitor the particle combustion temperature during aluminum combustion and the emissivity properties of alumina have been extensively studied within this wavelength range [65, 66, 75].

For each test approximately 20 mg of particles were injected into a 38.3 $in^3$ chamber filled with helium, nitrogen, or argon at various pressures for the present tests. The injection process uses the inert gas high pressure line to force particles through a mesh and small injection piece at the bottom of the chamber as shown in Figure 2.8. The injection piece has six holes at a 30 degree angle such that powder disperses evenly throughout the chamber.

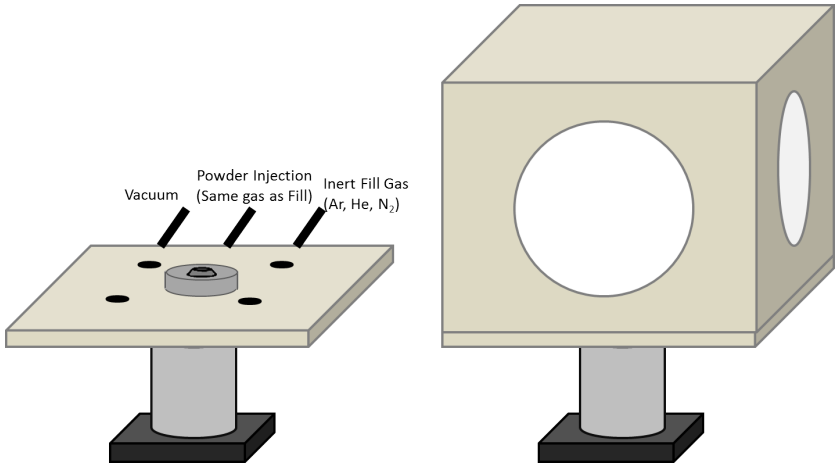


**Figure 2.8: Base section of LII experimental chamber including injector**

The ambient pressure of the inert gas within the chamber was varied between tests, however, the majority of the experiments were performed at 2 atm of pressure. At this pressure the Knudsen number is $\sim$2. Similar Knudsen numbers are observed in shock tube measurements of aluminum combustion [40]. The chamber has three quartz windows. The incandes-

cence is collected perpendicular to the path of the laser beam using an f/2 optical lens. Figure 2.9 shows a schematic of the test set-up. The particles are injected and allowed to equilibrate in suspension for 5 minutes prior to firing the laser pulse. The pulse duration and repetition rate are 5 ns and 20 Hz respectively. The LII signal was averaged over 15 laser pulses. The time resolution of the photomultipliers is approximately 10ns, significantly shorter than the overall incandescence which would last more than 500 ns. The system was calibrated using the chopped signal from a tungsten lamp at a known 3200 K temperature.

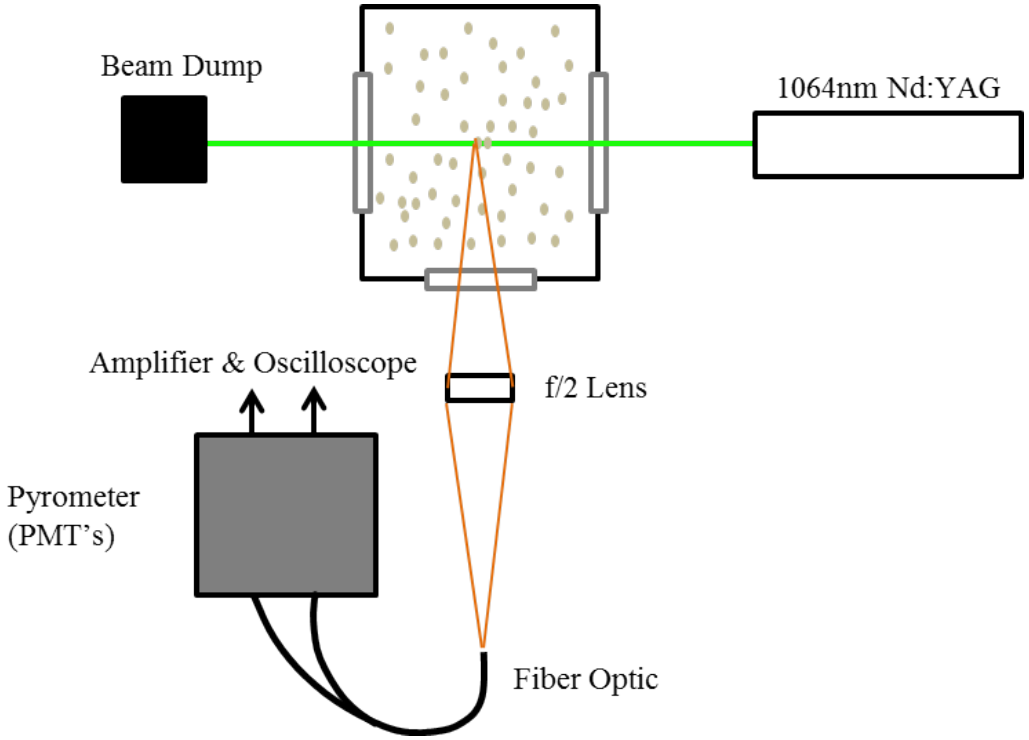


**Figure 2.9: Top view of LII experimental set-up**

VanDer Wal described the effects of varying laser fluence on metal nanoparticles with various vaporization temperatures using double pulse LII experiments [59]. It was shown that the threshold fluence before the onset of significant laser induced emission processes (LIE) was dependent on the vaporization temperature of each metal as shown in Table 2.2. Titanium, which has a similar vaporization temperature (3560 K) to the volatilization temperature of alumina (3800 K), had a threshold average fluence of 1.2 J/cm$^2$ for delayed detection 50 ns after the laser pulse.

The laser energy was measured using a Power Max 500D power meter, and

**Table 2.2: Threshold fluence for various metal and metal oxides**

| Metal | Vaporization Temperature (K) | Fluence (J/cm$^2$) |
|---|---|---|
| Iron | 3134 | 1.2 |
| Titanium | 3560 | 1.5 |
| Alumina | 3800 | Unknown |
| Molybdenum | 5833 | 1.8 |

the beam diameter was measured by systematically blocking the laser beam using a knife blade prior to the beam passing through a diffuser and the being monitored using a Thorlabs photodiode PDA36A. Using this method, the intensity of laser light that hits the photodiode decreases as the beam becomes increasingly blocked with the knife blade. Figure 2.10 shows the experimental measurement of intensity and the best fit cumulative density function assuming a Gaussian distribution.

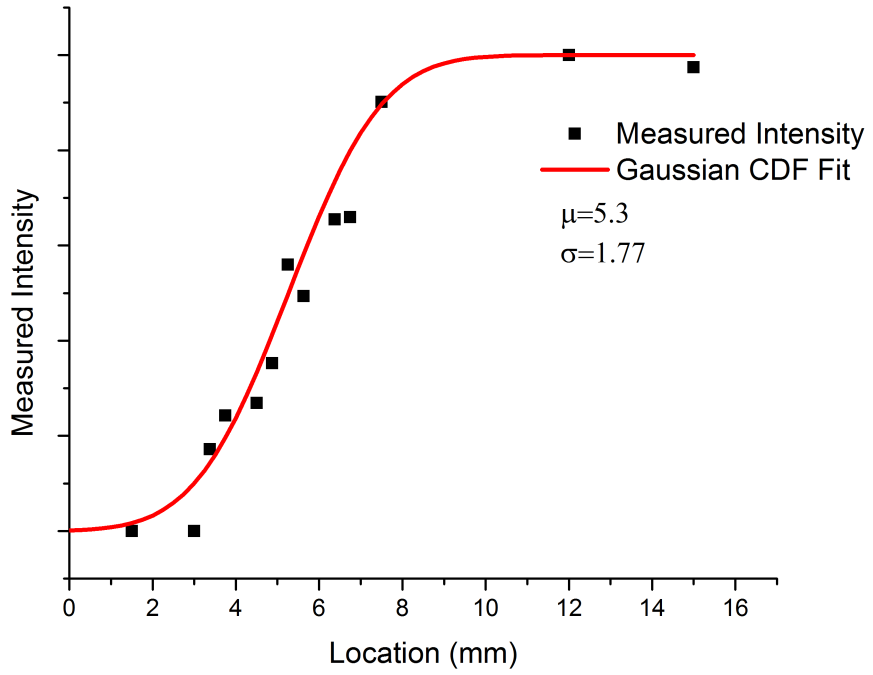


**Figure 2.10: Experimental measurement of laser beam diameter and best-fit Gaussian cumulative distribution function**

By integrating the Gaussian distribution to determine the beam area, the overall fluence is calculated to be 425 mJ/cm$^2$. This value represents the

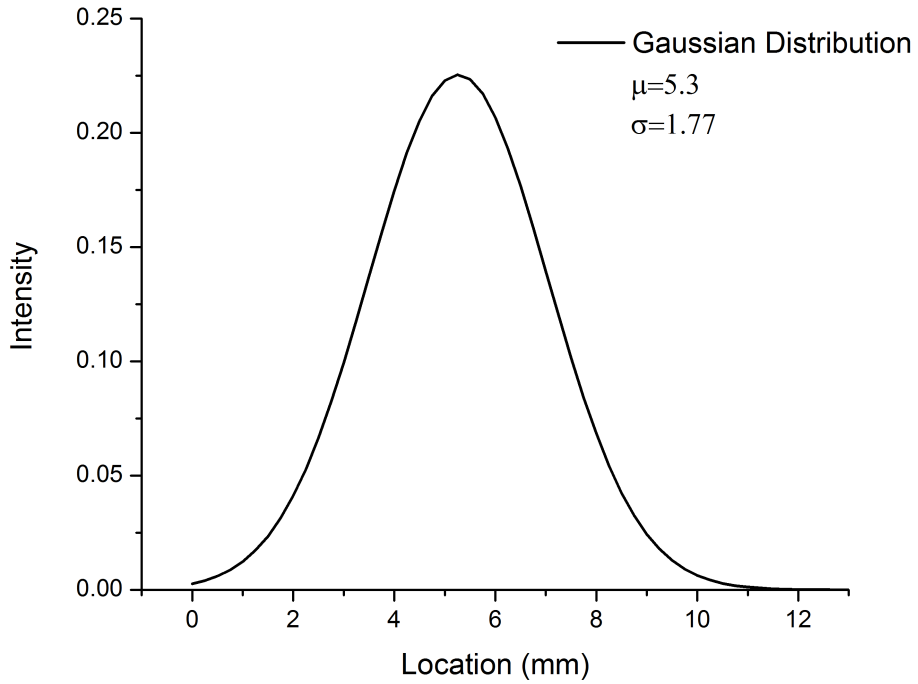


**Figure 2.11: Laser beam intensity distribution using best fit Gaussian distribution**

average fluence within the beam, as it is the total amount of energy within the beam divided by the total beam area. From Figure 2.11 the peak intensity is nearly twice the average value, and therefore the fluence may be as large as 1 J/cm$^2$ in regions within the beam. The 425 mJ/cm$^2$ average fluence is well below the threshold set forth by Vander Wal of 1.2 J/cm$^2$ [59].

## 2.4 Constant Volume Combustion

In order to further investigate the heat transfer properties of nano-aluminum a constant volume combustion experiment was performed. The heat transfer is monitored by measuring the energy release of the particles used to raise the pressure of the ambient gas. In this experiment a dilute amount of nano-aluminum powder is injected into a dilute hydrogen oxygen mixture ($\sim$10%$H_2$). The hydrogen oxygen mixture is spark ignited and the heat release from the hydrogen combustion which will result in aluminum ignition

and combustion with the excess oxygen. The pressure rise due to combustion will be monitored which will give an indication of the energy release. Similar measurements have been performed previously by Dreizin on metallic particles in methane-air mixtures [76].

During combustion, the stored energy can be lost to the ambient gas in form of pressure or through radiation to the environment as shown in the first law of thermodynamics. In cases where the accommodation coefficient is small, it is expected that radiation losses ($Q$) are large and measurable. In order to perform this experiment it is necessary to first characterize the energy release due to the hydrogen-oxygen mixture with inert particles ($E_{rxn}$). Once characterized, any energy release above the baseline must be due to aluminum particle combustion.

$$Q_{rad} = U(p,T)_{prod} - U(p,T)_{reac} - E_{rxn} \tag{2.8}$$

In order to use equation 2.8 the product particle composition must be well characterized. The post test particles were collected and analyzed to gain an estimate for the percentage of combustion completeness. With this estimate it was possible to determine the amount of energy lost due to radiation. Further assuming that the radiation losses from condensed water vapor are negligible will allow for an estimate of the radiation losses from the aluminum during combustion. In many combustion processes the energy lost due to radiation is considered negligible as a percentage of the total heat transfer. If the accommodation coefficient is sufficiently low the energy lost due to radiation is expected to be a significant percentage ($\sim$10-30%).

### 2.4.1 Experimental Set-up

The chamber used for the laser induced incandescence was also used for the constant volume combustion experiments. Figure 2.12 shows an image of the actual experimental set-up. Figure 2.13 shows a schematic of the set-up which varies from the LII experiments slightly in that spark ignition is needed and the gaseous mixture is flammable rather than inert in order to ignite the aluminum.

The chamber is initially vacuumed down through the vacuum port to near vacuum. After being purged at least twice, the hydrogen and oxygen gases

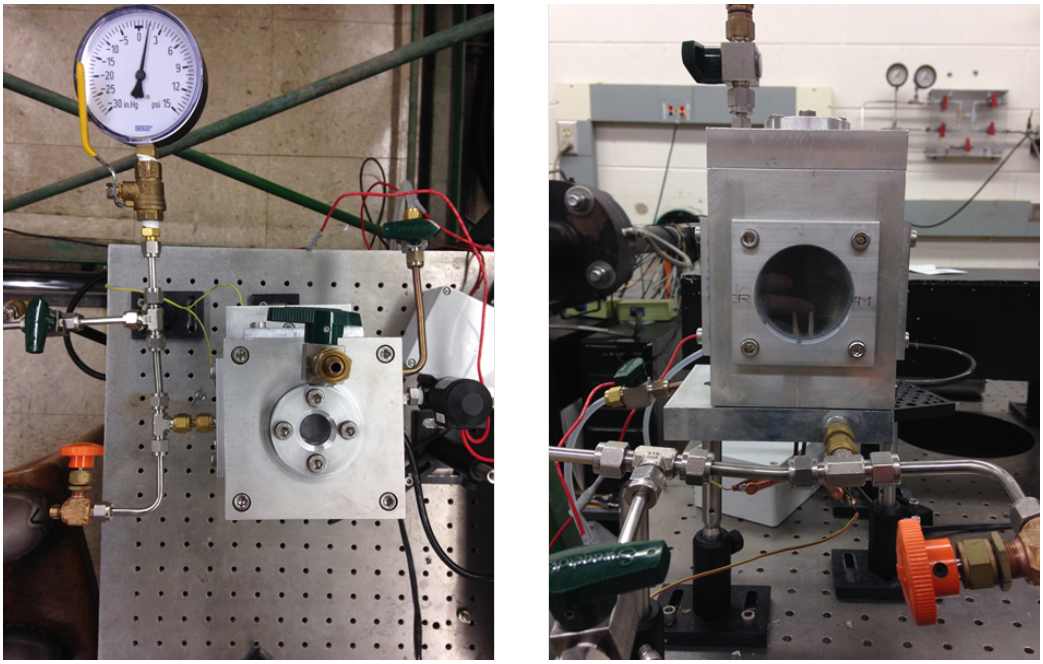

**Figure 2.12: Image of the constant volume combustion chamber from the top (left) and from the side (right)**

are introduced. The static chamber pressure is monitored using a SSI Technologies MGA-300 series pressure gauge in order to control the composition. Most experiments are run with a mixture of 10% $H_2$ and 90% $O_2$. The initial pressure in the chamber is 0.5 bar absolute. 80 mg of nano-aluminum particles are injected similarly to the injection process used for the LII experiments. The injection uses a solenoid valve that opens for 100 ms to allow a small amount of 15 psig oxygen to force the loaded nano-aluminum particles into the chamber. Exactly two seconds after the beginning of injection, a copper bridgewire (100 $\mu$m thick copper wire) is exploded using a fireset that discharges a capacitor with a voltage of approximately 4kV across the bridgewire. This energy explodes/ignites the bridgewire which in turn ignites the hydrogen oxygen mixture.

The pressure rise due to combustion is monitored using a GEMS 2200 series pressure transducer rated for vacuum to 45 psig pressures located at the top of the chamber. The pressure sensor is terminated using a 500 ohm resistor in order to measure the voltage using a PicoScope 4000 series oscilloscope. The time response of the pressure transducer is 0.5 ms. The ignition of the hydrogen oxygen mixture occurs near the center of the chamber and propagates throughout the 38.3 $in^3$ volume.

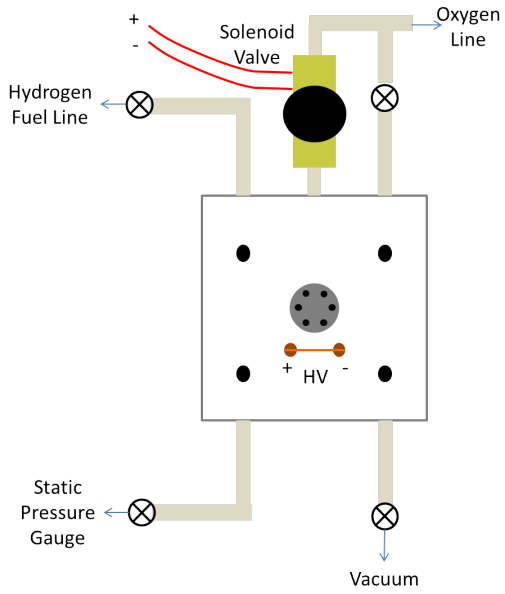


**Figure 2.13: Top down schematic of the test chamber set-up for constant volume combustion measurements**

Calibration tests are done to measure the pressure rise due to the hydrogen-oxygen combustion without nano-aluminum present. During these tests inert nano-alumina particles are injected to mimic the actual experimental conditions but do not react and release energy. The energy release due to the hydrogen combustion is subtracted off prior to determining the heat transfer release due to nano-aluminum combustion. The NASA Gordon-Mcbride constant volume calculation can be used in order to determine the theoretical equilibrium combustion pressure and temperature that would be achieved in adiabatic conditions.

After each test the particles are allowed to settle to the bottom and are then collected for processing. Energy-dispersive X-ray spectroscopy (EDS) is performed using a JEOL 6060LV general purpose SEM. The EDS device determines atomic species concentration from a specific sample. The collected particle oxygen concentration is compared to the oxygen concentration of nano-alumina particles and nano-aluminum particles that have not undergone combustion in the constant volume combustion chamber.

### 2.4.2 Chamber Calibration

The primary measurement in the constant volume combustion measurement is the transient pressure profile during combustion using the GEMS 2200 pressure transducer. The pressure transducer is statically calibrated by filling the combustion chamber with oxygen and measuring the static pressure with a digital SSI technology pressure gauge with 0.1 psi resolution. The pressure within the chamber is varied and the linear response of the GEMS pressure transducer is determined as shown in Figure 2.14. The pressure voltage relationship is shown to be highly linear as desired within the pressure range of the transducer.

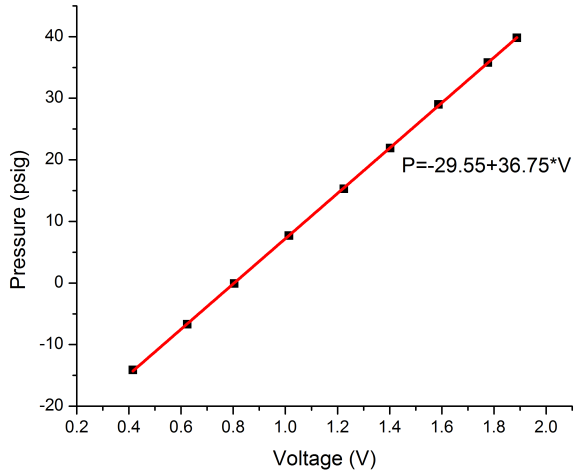


**Figure 2.14: Pressure calibration of the GEMS sensor with linear fit**

## 2.5 Particle Description

### 2.5.1 Nano-aluminum

Multiple nano-aluminum particle samples were obtained for the shock tube combustion experiments, each with a different nominal particle diameter size as shown in Table 2.3. The particles were obtained from SkySpring Nanomaterials and NovaCentrix nanomaterials. A Hitachi S-4700 high resolution

scanning electron microscope (SEM) was used to accurately characterize the particle size distribution of each sample. Over 100 particle diameter measurements were made from each sample in order to obtain a distribution. Table 2.3 shows the number average and mass average particle diameters of each nominal sample powder. The SkySpring 18 nm particles were not characterized because the resolution required to characterize these particles accurately was not achievable. Any distribution obtained would have been biased towards the larger particles which were readily resolved while the smaller particles below 18 nm would not have been accounted for. The highest resolution images achieved qualitatively showed the SkySpring 18 nm particle distribution to be significantly smaller than the other sample distributions even though an accurate average could not be quantified.

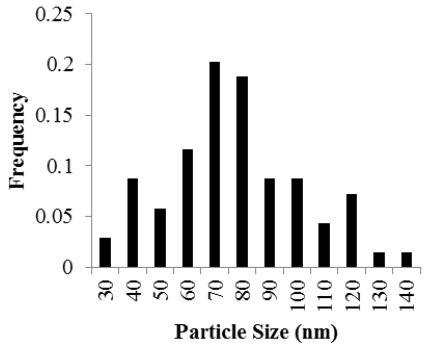


**(a) Particle size distribution for the SkySpring Nanomaterials 50nm particles**

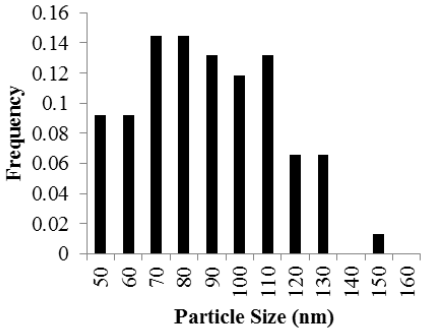


**(b) Particle size distribution for the NovaCentrix 80nm particles**

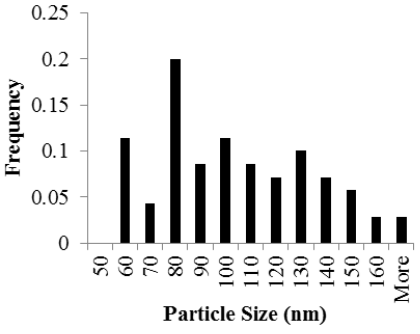


**(c) Particle size distribution for the NovaCentrix 110nm particles**

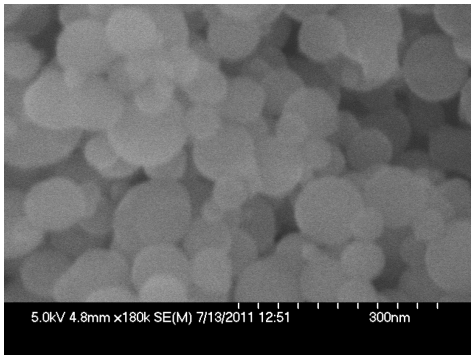


**(d) Sample Scanning Electron Microscopy (SEM) image of the NovaCentrix 80nm particles**

**Figure 2.15**

**Table 2.3: Summary of Average Particle Diameters**

| Particle Type | Number Average Diameter (nm) | Mass Average Diameter (nm) |
|---|---|---|
| SkySpring 18nm | - | - |
| SkySpring 50nm | 73.2 | 80.9 |
| NovaCentrix 80nm | 83.4 | 90.1 |
| NovaCentrix 110nm | 100 | 110 |

Each sample had a large distribution of particle sizes. Figure 2.15a-2.15c show the histograms of the three characterized samples and Figure 2.15d shows a corresponding SEM image for the NovaCentrix 80 nm particles. All particles imaged were found to be highly spherical. Nano-aluminum has previously been shown to form both weak and strong agglomerates dependent on the manufacturing process. The images show the particles acquired have weak agglomeration and very little particle necking. The particles acquired from NovaCentrix are specified to be 80-90% aluminum and the oxide-coating thickness is 1.5-2.5 nm. Both samples acquired from SkySpring Nanomaterials are 99.9% pure on a trace metals basis.

### 2.5.2 Nano-alumina Particles

The aluminum oxide particles were obtained from Alfa Aesar and have a nominal size of 40-50 nm and are 99.5% pure. In order to measure the accommodation coefficient using LII it is necessary to have an accurate estimate of the particle size distribution and knowledge of agglomeration. Previous efforts of LII on metal nanoparticles have focused on measurements of particle size during synthesis. In these efforts the particle size distribution is either laboriously measured through many TEM images of sampled particles or a lognormal distribution with specified standard deviation is assumed. Using TEM has been the preferred method for small particles, however in many synthesis processes it is not always possible to obtain TEM samples and therefore require distribution assumptions based on particle formation theory. In the latter the results are often highly dependent on the distribution assumption.

Here particle synthesis is not of interest, and the particles being used are

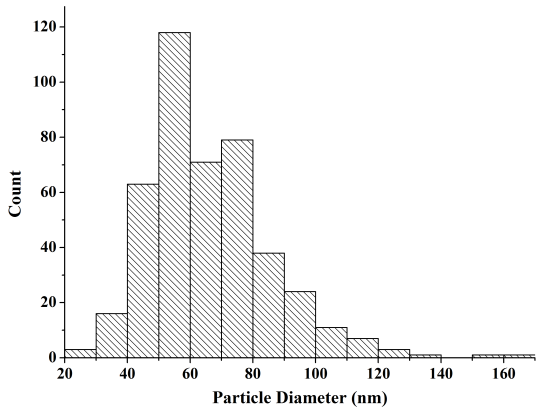


**Figure 2.16: Particle size distribution for the Alfa-Aesar 40-50 nm particles**

previously made and injected into the experimental chamber, and therefore the size distribution must be directly measured. The particles used presently are large enough to use scanning electron microscopy (SEM) analysis. More than 300 particles were measured in order to obtain an accurate statistical sample. Figure 2.16 shows a histogram of the measured sample particle sizes. The sample was found to have a significant size variation which must be accounted for in the interpretation of the accommodation coefficient. Figure 2.17 shows a representative SEM image showing the size variation within the particle sample. The particles are highly spherical and show only weak agglomeration with one another. SEM analysis was again performed using a Hitachi S4700 instrument.

## 2.6 Particle Agglomeration

The issue of nanoparticle agglomeration within the shock tube must be addressed as agglomerated particles may alter the interpretation of the measured burn times. The SEM images shown previously show that the particles are initially weakly agglomerated. The shock tube set-up is designed to promote the break up of weak agglomerates. During injection the particles are forced through an array of fine -325 gauges wire meshes ($\leq$40$\mu$m) which will disperse large agglomerates. Once aersolized within the shock tube the particles are further broken up by the incident and reflected shock wave. It

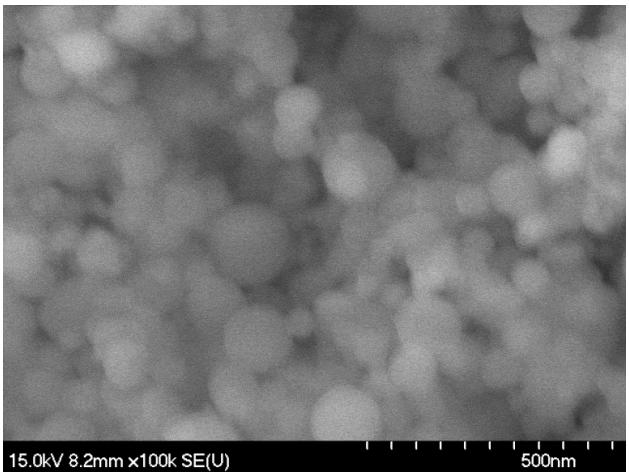


**Figure 2.17: Sample Scanning Electron Microscopy (SEM) image of the Alfa-Aesar 40-50 nm particles**

has been shown that shock waves are effective at breaking up weak agglomerations and is in fact the primary method used to break up agglomerated particles [77–79]. Thus, it is expected that after shock passage the particles are well dispersed. Burn time traces support the notion that the particles are well dispersed. The luminosity traces due to nanoparticles are significantly different than those observed for larger particles.

Once well dispersed, the primary concern is that agglomeration will occur during the test time after shock passage. Calculations have been performed in order to determine the effect of particle agglomeration. The first calculation treats the nanoparticle as a large gas molecule within the shock tube and determines the collisional frequency of one nano-aluminum particle with another. In order to perform this calculation the following assumptions were made. It was assumed that 0.1 mg of nano-aluminum particles were injected into the shock tube with an 8.9 cm diameter. The incident and reflected shock temperatures and pressures were 600 K and 3.5 atm (incident), and 1500 K and 20 atm (reflected). It is further assumed that the injected particles form an evenly spaced particle distribution with a uniform 80 nm pariticle size distribution and that the particle cloud thickness is 0.5 cm behind the incident shock. This assumption is supported by previous shock tube measurements in an acrylic optical section [37].

Using the above assumptions the aluminum cloud number density is calculated to be $4.4(10^{15})$ particles/m$^3$ and the particle mass is $7.24(10^{-19})$ kg. The particle speed is calculated using equation 2.9 and the collisional fre-

quency is calculated using equation 2.10 to be 3.81 collisions/s. Over the course of the incident shock residence time which is conservatively 5 ms the number of collisions is less than $2(10^{-2})$. The same calculation can be performed at the reflected shock conditions suggesting that there are less than $2.5(10^{-2})$ collsions.

$$\nu = \left(\frac{8k_bT}{\pi m_p}\right)^{1/2} = \left(\frac{8(1.381)(10^{-23})600}{\pi 7.24(10^{-19})}\right)^{1/2} \tag{2.9}$$

$$f = \frac{1}{4}c_o\nu A \tag{2.10}$$

The previous calculation treats the nanoparticle like a large gas molecule which is relatively conservative. The agglomeration can also be estimated by determining the particle collision rate using the Smoluchowski Monodisperse model which is often used for larger particles in aerosols. Smoluchowski solved a solution a simple ODE considering the Brownian motion of the particles in order to obtain the concentration profile as a function of time which is shown in equation 2.11. The particle flux can be calculated using equation 2.12.

$$c = c_o\left[1 - \frac{d}{r} + \frac{d}{r}\text{erf}\left(\frac{r-d}{2\sqrt{Dt}}\right)\right] \tag{2.11}$$

$$f = c_o\pi d^2 D\frac{\delta c}{\delta r} \tag{2.12}$$

Using equation 2.12 with $D=5(10^{-9})$ $\text{m}^s/\text{s}$ at the incident shock temperature (600 K) and $D=20(10^{-9})$ $\text{m}^2/\text{s}$ at the reflected shock temperature (1500 K) the flux is calculated as a function of time. Figure 2.18 shows the calculated flux which can be integrated over time in order to determine the number of collisions. Using this method the number of collisions within the shock tube test time is $1.42(10^{-2})$ which is again negligble. Therefore, the results indicate agglomeration during the test time is relatively small due to the short time scales behind the incident and reflected shock.

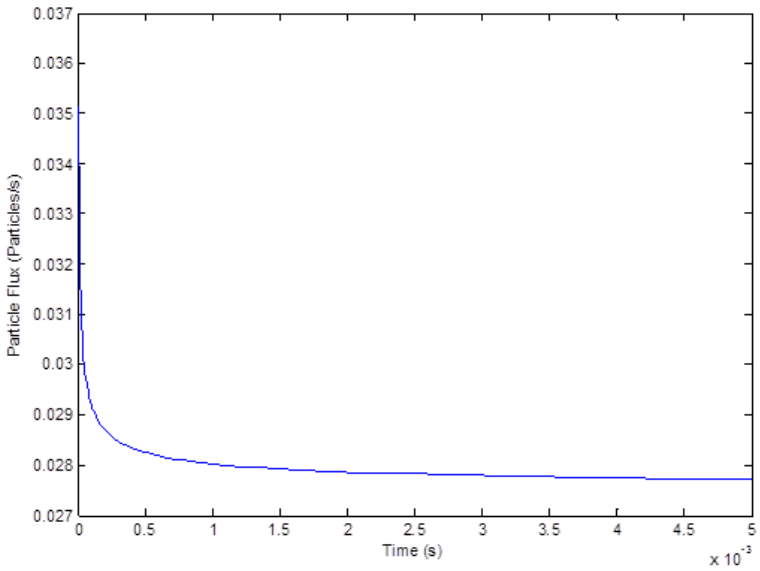


**Figure 2.18: Particle flux as a function of time calculated using the Smoluchowski monodisperse model**

# CHAPTER 3

# SHOCK TUBE COMBUSTION RESULTS AND DISCUSSION

## 3.1 Emissivity Measurements

In order to accurately perform pyrometry measurements of nano-aluminum combustion it was necessary to measure the emissivity properties at temperatures as low as 1500 K which had not previously been done as discussed in Section 1.4. Figure 3.1 shows an example transient temperature plot where the experimental temperature has been calculated using three color pyrometry with different wavelength dependencies. The graph shows that the nano alumina particle temperature remains relatively constant in the inert environment behind the reflected shock as expected.

In Figure 3.1 it is clear that the experimental particle temperature most closely matches the ambient temperature calculated from the shock relations using an emissity relation between $\epsilon \sim 1/\lambda$ and $\epsilon \sim 1/\lambda^2$. Using the method described in Section 2.2 the functional relationship of the emissivty with wavelength is precisely calculated by fitting a power law. In order to do this the luminosity signal $I_{exp}$ is integrated over the entire test time to increase the signal to noise ratio, and Equation 2.2 is used which is rewritten below in Equation 3.1. The intensity traces at each wavelength using the pyrometer have 1 $\mu$s time resolution. Using the integrated intensity over the entire test time is mathematically similar to using the average temperature in Figure 3.1 in order to best fit the wavelength dependence. This process is done at temperatures above and below the melting temperature of alumina in order to determine if a shift occurs.

$$F(\lambda) = \frac{I_{exp}}{I_{exp,bb}} \frac{I_{cal,bb}}{I_{cal}} \tag{3.1}$$

Figure 3.2 shows the functional wavelength dependence at the three discrete wavelengths and the resulting wavelength power law fit which was nor-

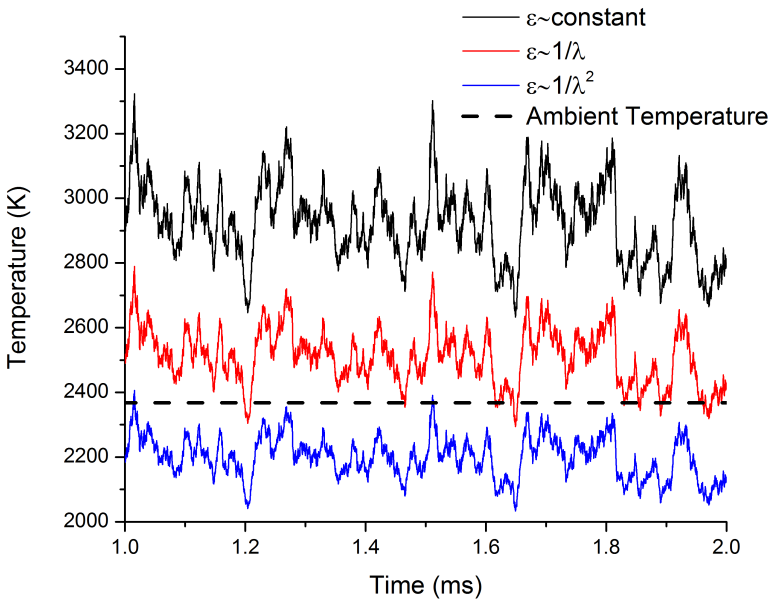


**Figure 3.1: Comparison of calculated particle temperature using various common emissivity assumptions to the ambient temperature derived from shock relations**

| Temperature (K) | C | n | $R^2$ |
|---|---|---|---|
| 2644 | .7247 | -0.918 | .9978 |
| 2368 | .6026 | -1.446 | .9994 |
| 1801 | .4227 | -2.449 | .9889 |

**Table 3.1: Power fit parameters for nano-alumina using the pyrometer setup. Fits were normalized to a wavelength of 0.7 $\mu$m**

malized to 0.7$\mu$m. The fit parameters for the power law according to Equation 2 are tabulated in Table 3.1. A shift in the wavelength dependence of nano-alumina emissivity from $\lambda^{-0.92}$ to $\lambda^{-2.4}$ appears to occur as the phase changes. The resultant wavelength dependency at 2644 K agrees well with the higher temperature wavelength dependency ($\lambda^{-1}$) found using the previously discussed full spectral range by Kalman [66]. At 1801 K the wavelength dependency has shifted, potentially due to alumina phase change from liquid to solid. For the solid phase alumina, the $\lambda^{-2}$ emissivity assumption appears to be more appropriate than the other assumptions. The 2368 K test is very near the 2327 K alumina melting temperature, and the wavelength dependence is between the two limits yielding a monotonic temperature de-

pendence. The value tabulated in Table 3.1 at 2368 K of n∼-1.45 is consistent with Figure 3.1 where graphically it is obvious that the best fit wavelength dependence is between $\epsilon \sim 1/\lambda$ and $\epsilon \sim 1/\lambda^2$.

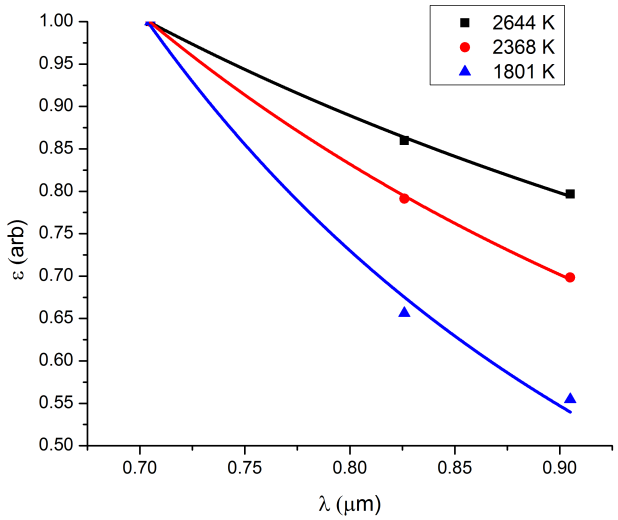


**Figure 3.2: Spectral Emissivity measured at lower temperatures with the PMT setup. All curves are normalized at 0.7$\mu$m.**

Kalman compared the experimental data at these lower temperatures with a model based on Mie theory [66] using the refractive indices provided by Bakhir [80] and Parry and Brewster [81]. The model using Bakhir's data yielded a spectral dependence near $\lambda^{-0.7}$ for all three temperatures. The indices calculated by Parry and Brewster provided a dependence of approximately $\lambda^{-2}$ for this temperature range. The latter slightly agrees with the measured spectral dependences from the current work. Neither set of refractive indices show the strong temperature dependence that is seen from the measured spectra. However these indices of refraction were not measured from highly pure alumina particles or in argon. Further it was suggested by Reed and Calia [82] that impurities in the samples critically changed the indices of refraction measured, and they found a large spread in the data from many authors. For these reasons, it is not expected that the results here necessarily match those predicted by Mie theory using the indices of refraction that are available.

## 3.2 Spectroscopic Measurements

Emission spectroscopic measurements of aluminum combustion were performed through the sapphire end-wall of the fiber optic end section using the methods discussed in Section 2.1.2. The emission spectra gives an indication of the gas phase reaction that is occurring during combustion. Lynch has previously shown that there is very little gas phase emission or absorption at the temperatures of consideration in the present study during nano-aluminum combustion in oxygen [39]. For nanoparticles it was found that aluminum monoxide (AlO) gas phase emission and absorption was not present at temperatures below 2300 K, and Al vapor was not seen in emission below 2300 K and was not seen in absorption below 1500 K. The amount observed in absorption was relatively little. Similar emission experiments were performed here in order to verify the lack of gas phase emission in all ambient conditions.

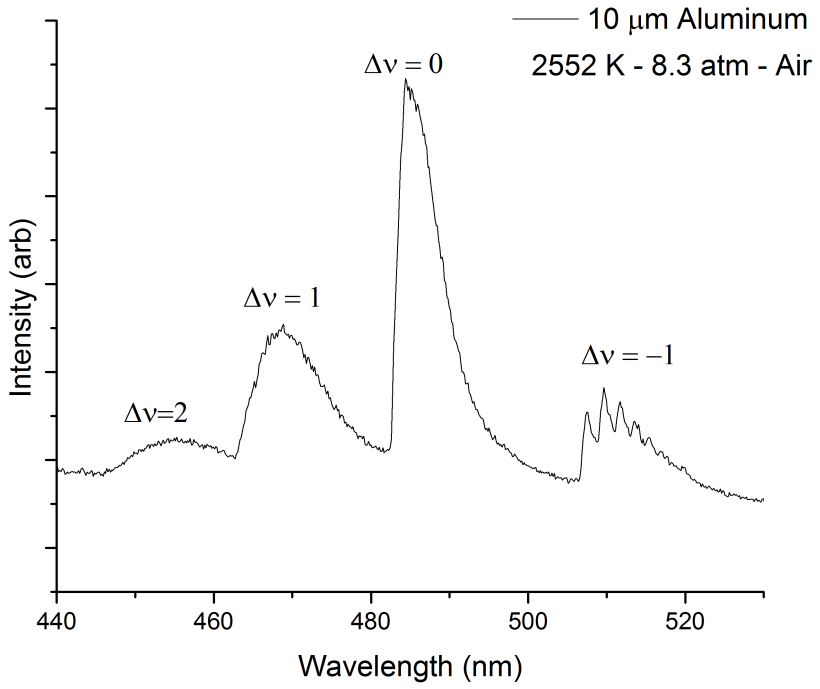


**Figure 3.3: Emission spectra of the combustion of 10$\mu$m aluminum particle showing evidence of AlO gas phase emission**

Based on the results of Lynch it was expected that the emission will be solely thermal during the combustion of nano-aluminum. This is contrary to

what is seen during large particle ($\geq$10$\mu$m) combustion where AlO emission is prevalent as is shown in Figure 3.3. The emission spectrum shown in Figure 3.3 was measured in the same shock tube experiment as the present nano-aluminum particle combustion measurements were taken. Aluminum vapor emission can also be seen during the combustion of large aluminum particles at 396.1 nm due to the significant amount of gas phase reaction.

Tests were performed in 20%$O_2$-80%$N_2$ and 20%$CO_2$-80%Ar at pressures varying from 5-30 atm and ambient temperatures varying from 1500-2000 K. The emission spectrum observed was purely thermal radiation as is shown in Figure 3.4 under all conditions.

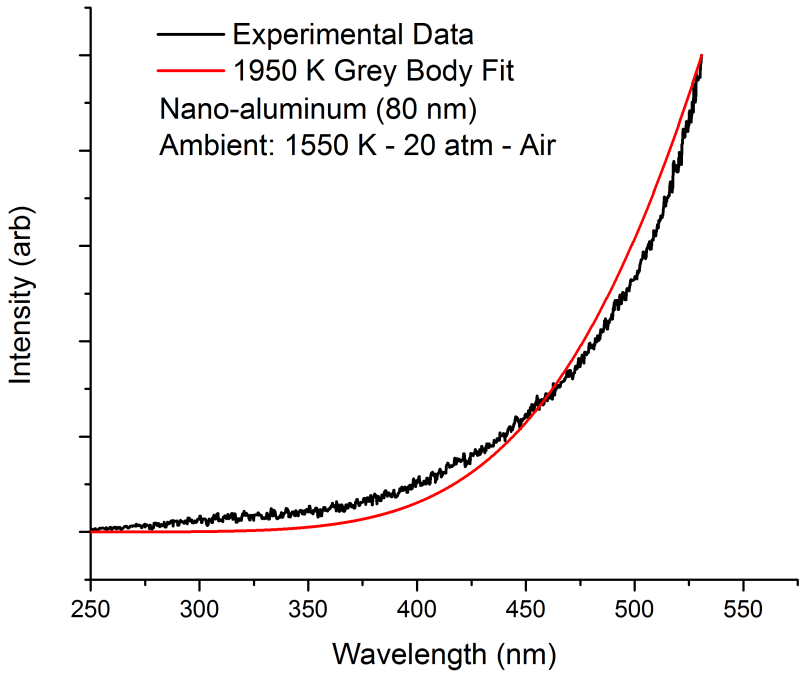


**Figure 3.4: Greybody radiation fit to experimental data using emissivity assumption from Kalman [66]**

While only thermal emission was observed for each condition, the slope of the thermal emission curve that was observed changed in different environments. The slope gives an indication of the condensed phase temperature during the test similar to pyrometry, however, the spectrum is integrated over the entire 2 ms test time and therefore gives little insight into the transient combustion event.

A grey body curve can still be fit to give an estimate of the thermal temperature and has been done previously for larger particle combustion background signals [75]. When this is done using the emissivity assumption proposed by Kalman [66] the result shows the condensed phase temperature to be ∼1950 K. This temperature is non-physical, but represents an intensity weighted temperature average for the combusting particles during the 2 ms test time. In reality the combusting particles have a transient temperature profile where the temperature is above 1950 K during the burn time of the nanoparticle and then emit at the ambient 1550 K for the remainder of the test time after combustion has completed. This temperature averaging is the primary reason the best curve fit in Figure 3.4 appears to have a slightly different curvature than the experimental data.

The curve fit temperature result does indicate that the particle temperature rises significantly above the ambient environment temperature which has important implications for the heat transfer of the nanoparticle that will be discussed in greater detail later. Had the particle temperature remained near the ambient temperature as predicted using conventional heat transfer expressions the transient temperature would be constant, and the grey body temperature fit would indicate the particle temperature to be 1550 K. The fact that this is not the case supports later pyrometry measurements that the particle temperature rises above the ambient temperature.

## 3.3 Burning Time Measurements

### 3.3.1 Air Burn Time Results

Shock tube burning time tests were repeated at least four times at each ambient condition for all particle classes in order to obtain a good estimate of the overall burning time with run to run deviation. The run to run variation for the nanoparticles was relatively low, especially at higher temperatures. Figure 3.5 shows the run to run variation for nominally 50 nm particles at 2000 K and 20 atm for four different tests. The traces were normalized and shifted such that the initial rises all begin to occur at time zero on the graph. These traces were then averaged when comparing separate conditions in order to depict a characteristic luminosity trace at a given temperature

and pressure.

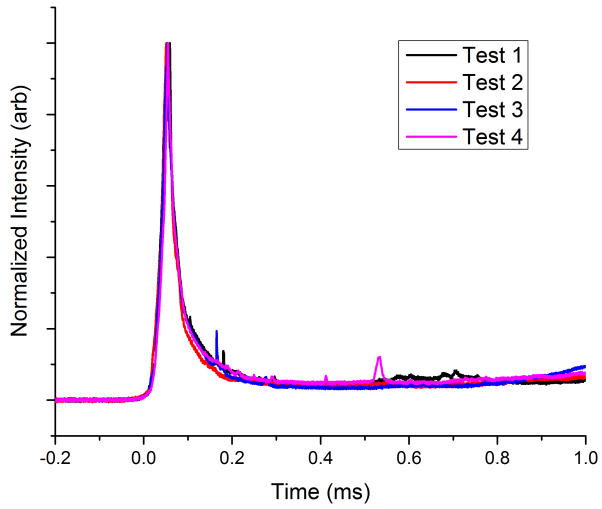


**Figure 3.5: Comparison of the normalized luminosity trace between four separate tests for the nominally 50 nm particles at 2000 K and 20 atm**

The burning time measurements showed relatively long burn times, greater than 50 microseconds for all nano-aluminum particle classes combustion in every environment and in some conditions much greater ($\sim$500$\mu$s). Figure 3.6 shows an example luminosity traces for the nominally 50 nm particles burning in air at various pressures. A strong pressure dependence is evident which is a significant deviation from the results of Beckstead for particle combustion greater than 20$\mu$m. The Beckstead correlation previously discussed in equation 1.5 shows very little pressure dependence for particle burning in a diffusion dominated flame structure. Instead, the luminosity traces show a near linear dependence with pressure.

The linear burn time dependence with pressure trend continued even as the ambient temperature was increased to 2000 K as shown in Figure 3.7. A linear pressure dependence is predicted in a kinetically limited process where the reaction rate is directly dependent on surface concentration of oxidizing molecules. Using the 10-90% area burn time method as discussed previously in Section 2.1.3 the pressure dependence was found to be approximately $P^{1.26}$ at 1500 K and $P^{0.92}$ at 2000 K in air. Theoretically if the nanoaluminum particles are combusting in the purely kinetic limit for both regions a pressure

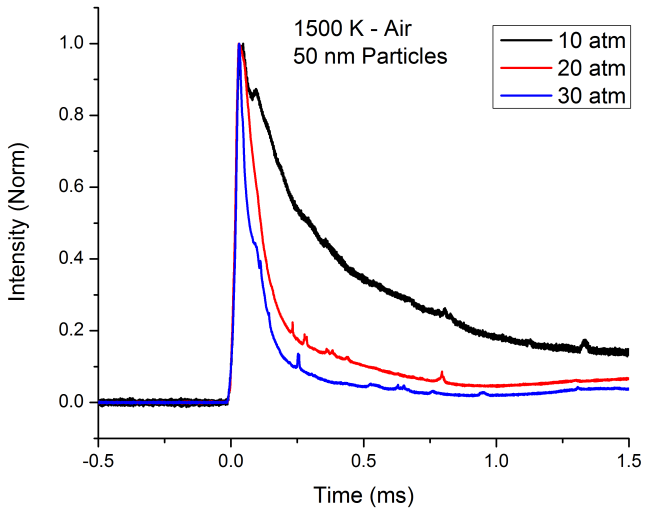


**Figure 3.6: Characteristic luminosity trace of 50 nm aluminum particles in air at 1500 K and various pressures**

dependence of $P^1$ would be anticipated for both; however, the results are relatively close to the theoretical solution and may deviate solely due to the use of the 10-90% area burn time cutoff method. The further deviation from $P^1$ at 1500 K may also suggest that rather than a purely surface reaction, solid state diffusion may become a greater limitation at lower ambient temperatures.

A significant temperature dependence on the particle burn time was also seen and is shown in the comparison between Figure 3.6 and 3.7. For micron sized particles the Beckstead correlation suggests a very weak temperature dependence. Again, the deviation from the Beckstead correlation predictions suggests a transition to a more surface process limited combustion mechanism as previously suggested. In a combustion mechanism where solid state diffustion and/or kinetics are the primary controlling mechanism a large temperature dependence is expected due to the Arrhenius nature of kinetic reactions.

Figure 3.8 summarizes the burn time results from each test for 50 nm particles in air at 10, 20, and 30 atm with the temperatures varying between 1500 and 2000 K. The graph clearly shows both a strong temperature dependence and a pressure dependence. The Arrhenius fit to the data yielded activation energies of 74.9 kJ/mol, 65.1 kJ/mol, and 63.4 kJ/mol at ~9.2,

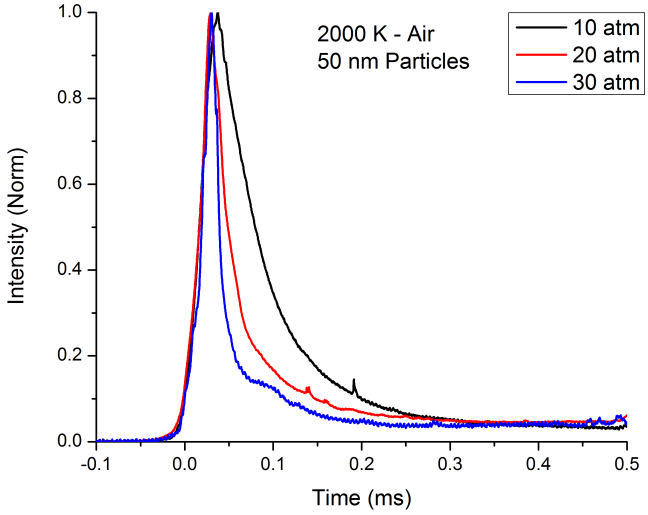


**Figure 3.7: Characteristic luminosity trace of 50 nm aluminum particles in air at 2000 K and various pressures**

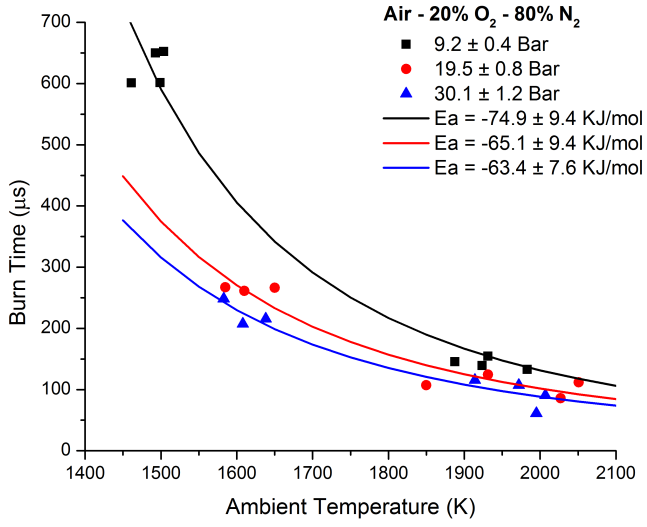


**Figure 3.8: Plot of burn time vs. ambient temperature for various pressures including an Arrhenius fit in order to determine the activation energy of the reaction**

19.5, and 30.1 bar respectively. These values compare favorably with previously measured activation energy by Bazyn where he found a 71.6 kJ/mol activation energy for nano-aluminum combustion at 8 atm and a 50.6 kJ/mol activation energy at 32 atm. Table 3.2 shows previously measured activation energies for aluminum oxidation from various references and experiments.

| Activation Energy (kJ/mol) | Reference |
|---|---|
| 63.4-74.9 | Present Result |
| 50.6-71.6 | Bazyn 2006 [25] |
| 77.9 | Roberts et al. 1993 [9] |
| 83.8 | Medvedev et al 1982 [83] |
| 95.5 | Hlavacek et al. 1993 [84] |

**Table 3.2: Measured activation energies from various references for aluminum oxidation**

When the ambient temperature was raised to 2500 K the luminosity trace no longer continued to demonstrate the same shape as was seen at lower temperatures. Figure 3.9 shows a luminosity trace that is representative of the nanoparticle burning at 2500 K in air at 10 atm. In Figure 3.9 there are two distinct peaks, the first of which is similar to the luminosity traces seen at lower ambient temperatures and the second late time peak which is much broader and long lasting.

It is suggested that the second peak is due to larger micron size particles within the sample. Very few large particles were observed within the sample using SEM, however the luminosity from the particle scales with the surface area. Therefore, a 5 micron sized particle will emit 10,000x stronger than a 50 nm particle and may dominate the signal. Micron sized particles are well known to only ignite at temperatures above 2300 K. They are also likely to be observed in the late time luminosity signal because they have a larger Stokes number than the nanoparticles and take longer to accelerate and decelerate to the gas velocity behind the incident and reflected shock. Because it is not obvious how to deconvolve the two separate particle combustion regimes a burn time for nanoparticles at temperatures greater than 2500 K is not suggested. This issue is not present at temperatures below 2300 K where micron sized particles will not ignite and thus will remain at the ambient temperature. At these temperatures the large particles only contribute to the background signal.

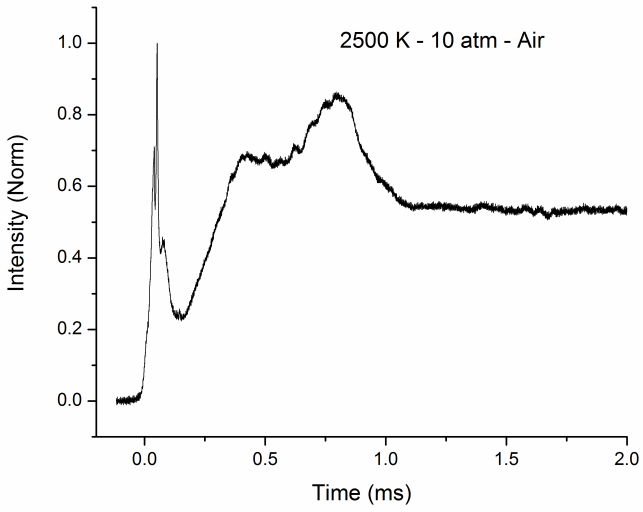


**Figure 3.9: Experimental luminosity trace of 50 nm particles burning in air at 2500 K and 10 atm**

Tests were also performed to determine the diameter dependence of the burning time using the 18, 80, and 110 nm nominal nano-aluminum samples. The diameter dependence gives a strong indication of the particle combustion regime as discussed previously. A combustion mechanism that is purely kinetically limited would fall within the $d^1$ while a gas phase or solid state diffusion mechanism would scale with $d^2$.

As shown in Section 2.5 each sample had a significant size distribution even while given a nominal particle size. Therefore, it was inherently difficult to ascertain a diameter dependence with any degree of certainty. Figure 3.10 shows a characteristic luminosity trace for each particle class in air at approximately 1500 K and 20 atm of pressure. It is clear that the 20 nm sample has a significantly shorter burn time than the other particles, however the 110 nm sample appears to have the next shortest burn time which is an unexpected and likely unphysical result. This result is attributed to the significant sample size distribution and run to run deviation which cannot be ignored. In all tests, the 20 nm sample had a significantly shorter burn time, however beyond this result the three other samples had relatively similar overall decay times once many tests had been averaged. Within this result, no diameter dependence could be easily gleaned.

Using only a comparison between the 20 nm particles and the other particle

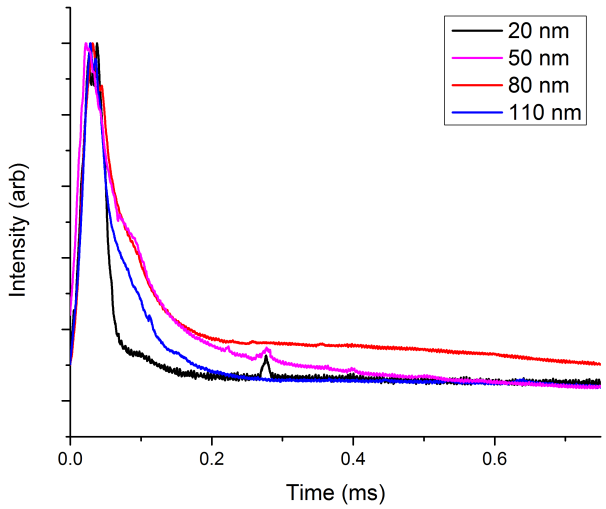


**Figure 3.10: Comparison of characteristic luminosity traces from each particle sample in air at 1500 K and 20 atm**

samples as a group, it can be decisively stated that the burn time scaling is much less than $d^2$. The average burn time for the 20 nm particles was approximately 100 $\mu$s. For 80 nm particles the burn time would need to be 1600 $\mu$s in order for $d^2$ scaling to apply which is clearly not the case. Even if the average particle size was closer to 40 nm for the nominally 20 nm particles the burn time would need to be 400 $\mu$s which does not appear to be the case. Therefore, within sample size uncertainty and run to run deviation it is likely that the diameter dependence is much less than $d^2$; however, beyond this estimation an exact diameter dependence cannot be determined. Both Huang [85] and Fitzgerald [86] previously suggested using flat flame burner combustion of nano-aluminum that the diameter dependence was on the order of $d^{0.3}$ which is within experimental uncertainty of the present results.

### 3.3.2 $CO_2$ Burn Time Results

The pressure and temperature dependence seen for nano-aluminum combustion in air was also seen in other oxidizing environments. Aluminum has been previously shown to combust in both $CO_2$ and $H_2O$ environments which has made it attractive for a potential propellant in other atmospheres. Because

of this, aluminum combustion has been extensively studied in these oxidizing environments. The Beckstead correlation can be used to predict burn times in either $CO_2$ or $H_2O$ using weighted oxidation efficiencies. Curious results have been seen regarding the relative oxidation efficiency of $CO_2$ and $H_2O$ for micron size particles within the transition regime. Lynch found a shift in relative oxidation efficiency that suggested for large particles within the diffusion regime $H_2O$ is a more efficient oxidizing agent while in the transition regime $CO_2$ becomes more efficient at higher oxidizing concentrations. Tests were performed using the heterogeneous shock tube in order to characterize the performance of nano-aluminum in $CO_2$ environments. Figure 3.11 shows characteristic luminosity plots for 50 nm aluminum combustion in $CO_2$ at 2000 K in various pressures.

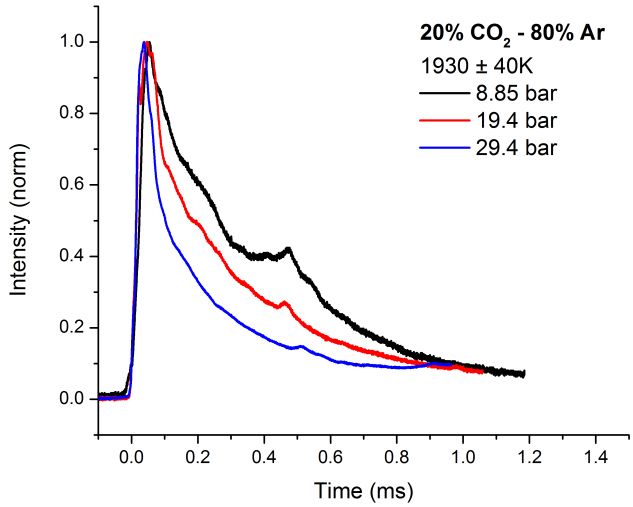


**Figure 3.11: Characteristic luminosity traces of 50 nm aluminum combustion in $CO_2$ at 2000 K and various pressures**

Figure 3.11 again shows the significant pressure dependence indicating a surface controlled mechanism. The burn times found for 50 nm aluminum in 20% $CO_2$ are significantly longer than the burn times found for the same particles in air when comparing Figure 3.11 and 3.7 as expected. Oxygen is a significantly more efficient oxidizing agent than $CO_2$, and the resulting burn times are nearly a factor of 5 times more efficient when using air compared to a similar mole fraction of $CO_2$. Table 3.3 shows the mole fraction of monatomic oxygen and diatomic oxygen at 2000 K and 10 atm for both envi-

ronments. In air, the mole fraction of O and $O_2$ are 7.7 and 59.4 times greater in air than in the $CO_2$ environment respectively. The ratio between the burn time in each environment and ratio between the mole fraction of monatomic oxygen are similar suggesting that in both environments the rate limiting kinetic step may be the reaction of monatomic oxygen with aluminum. This analysis does not consider the kinetics involving carbon monoxide the formation of which is an important kinetic step in aluminum combustion in carbon dioxide environments.

**Table 3.3: Concentration of oxidizing species at 2000 K and 10 atm in air and $CO_2$ environments**

| **Gas Environment** | **Mole % O** | **Mole % $O_2$** |
|---|---|---|
| 20% $O_2$ - 80% $N_2$ | $9.52(10^{-5})$ | $2.06(10^{-1})$ |
| 20% $CO_2$ - 80% Ar | $1.24(10^{-5})$ | $3.47(10^{-3})$ |

In the case of $CO_2$ as an oxidizer no combustion signature was observed from a luminosity trace for nano-aluminum combustion at 1500 K. Bazyn previously found 80 nm aluminum to indicate combustion via luminosity at temperatures as low as 1500 K in 50% $CO_2$ however the decrease in concentration from 50% to 20% may significantly affect the ignition temperature in a surface limited combustion process.

Unlike in the case of oxygen, at temperatures up to 2500 K late time particle combustion did not interfere with burn time measurements at pressures above 30 atm. This result suggests that the larger micron sized particles/agglomerates did not combust at 2500 K within $CO_2$ at 20% concentrations. Lynch previously found that the burn time of aluminum particles combusting in the transition regime decreases with increasing pressure giving which agrees with the interpretation that at higher pressures larger particles within the sample may begin to combust more efficiently [20].

An Arrhenius plot can again be fit to the $CO_2$ burning time results as was done previously for air. Figure 3.12 shows the calculated activation energies for nano-aluminum combustion in 20% $CO_2$ which were found to be 103.9 kJ/mol and 113 kJ/mol at 19.2 and 9.5 bar respectively. These activation energies are nearly twice the value observed for combustion of nano-aluminum in air.

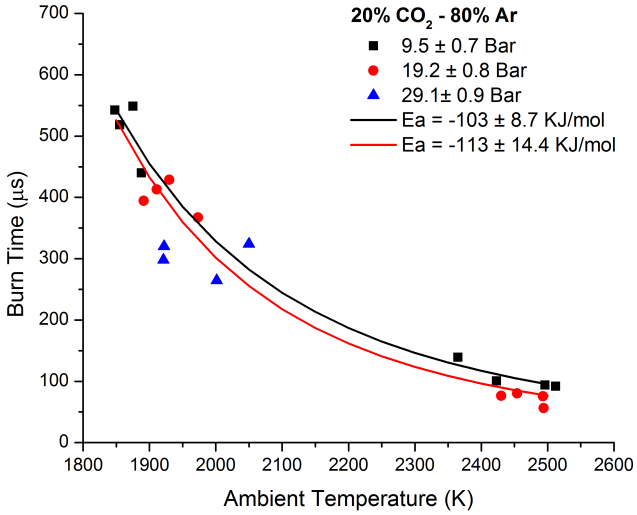


**Figure 3.12: Plot of burn time vs. ambient temperature for 50 nm aluminum in 20%$CO_2$ - 80%Ar at various pressures including an Arrhenius fit in order to determine the activation energy of the reaction**

## 3.4 Pyrometry Measurements

Pyrometry measurements give a transient temperature profile of the condensed phase during combustion. In the case of nano-aluminum the evidence suggests the primary reactions occur at the particle surface and therefore the pyrometry gives an indication of the overall heat release. Pyrometry results were taken simultaneous to photometry measurements in each environment at various ambient temperatures and pressures. The three color temperature was calculated using the emissivity assumption previously discussed in Section 3.1. The emissivity was shown to change significantly above and below the melting temperature of aluminum, and therefore the emissivity assumption is allowed to vary depending on particle temperature. Rather than create the change as a stepwise function at 2300 K which would numerically create a non-physical stepwise drop in temperature the emissivity assumption was allowed to transition linearly over the temperature range of 2300-2000 K as it cooled. This treatment did not significantly alter the shape of the temperature profile as compared to the shape temperature profile without changing the emissivity; however, it did result in lower calculated temperatures when the particle is below the melting temperature of alumina.

### 3.4.1 Air Pyrometry Results

The three color pyrometry measurements indicated a rise in particle temperature above the ambient gas temperature during high pressure combustion that was previously seen by Bazyn [25] but is unexpected considering traditional heat transfer losses from the particle. The particle temperature initially rises relatively rapidly and then steadily decays to a temperature slightly above the ambient temperature which is measured using the shock relations. The duration of the temperature rise is similar to the duration of the luminosity trace used to measure the burn time as would be expected because both are direct indications of particle temperature. The calculated three color temperature has a considerable amount of fluctuation due to the exponential nature of Planck's law. A Savitzky-Golay filtered temperature profile is also shown in order to reduce some of the fluctuation in the temperature profile.

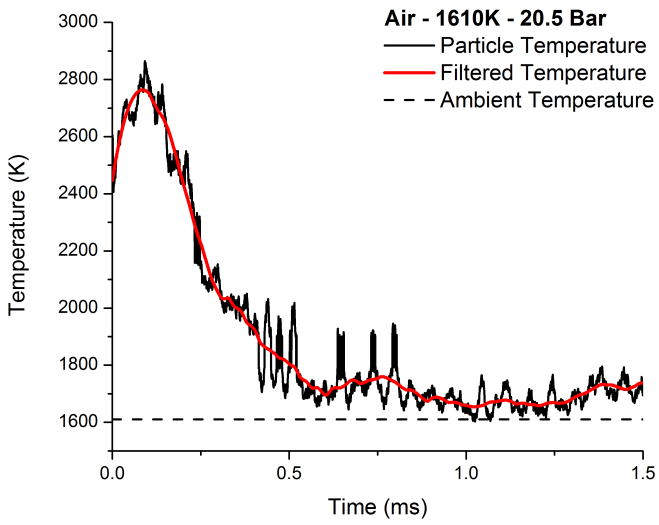


**Figure 3.13: Three color pyrometry temperature measurement of the nominally 50 nm aluminum particles combustion in air**

Figure 3.14 summarizes the peak temperature results for the 50 nm particle combustion in air environments. It is clear that there is a significant pressure dependence on the peak temperature. At low pressures the peak temperature is only slightly above ambient, while at high pressures the peak temperature approaches 3000 K. The pressure dependence is further indication of a surface

combustion process which is highly dependent on surface concentration of the oxidizer. This was seen previously in the burning time measurements where the nanoparticle burn time was equally dependent on the ambient pressure.

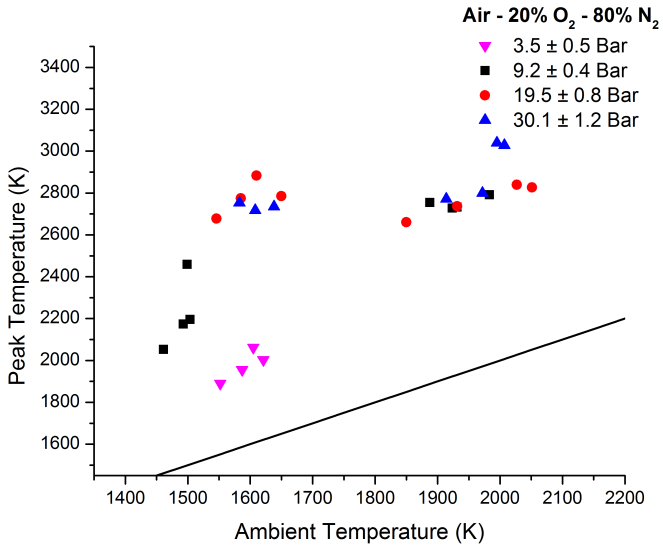


**Figure 3.14: Summary of peak temperature during 50 nm particle combustion vs. ambient temperature at various pressures in air**

The peak temperature appears to remain relatively constant as the ambient temperature is increased further at the higher pressures with only a small overall increase in ambient temperature. This may suggest that above approximately ~3000 K another temperature limiting heat loss mechanism begins to dominate. This could be an indication that when the particle reaches these high temperature boiling of aluminum which ranges from 2800-3400 K depending on the ambient pressure. The boiling temperature is higher for the higher pressures which would suggest that the peak temperature should be higher for the 30 bar experiments compared to those at 20 bar, if boiling were the temperature limiting effect which does not appear to be the case at 1500 K ambient temperatures. At 2000 K ambient temperatures the average peak temperature is higher for 30 bar experiments compared to 20 bar experiments but only slightly and within uncertainty. This analysis ignores the fact that heat losses are likely greater for the 30 bar experiments, and therefore the resulting similar temperatures may be an offset of boiling effects and heat loss due to the surroundings. As the pressure increases the heat loss due to vaporization of aluminum will be decreased until higher temperatures

are achieved but heat loss to the surroundings is likely linearly increased.

**Table 3.4: Summary of nano-aluminum particle peak temperatures measured using 3-color pyrometry during combustion in air at 20 atm**

| Particle Type | Peak Temperature (K) |
|---|---|
| SkySpring 18nm | 3145 |
| SkySpring 50nm | 2854 |
| NovaCentrix 80nm | 2794 |
| NovaCentrix 110nm | 3004 |

The average peak temperature is between 3200-3500 K for all particle samples at approximately 1500 K and 20 atm in air. Bazyn et al. [25] similarly found peak temperatures for nano-aluminum combustion near 2500 K for 8.5 atm pressures and 3500K for 32 atm pressures. If the combustion process is surface limited the rate of heat gain and the rate of heat loss should scale similarly; however, the volumetric heating of the particle would suggest that smaller particles should reach a higher temperature if no heat sink such as aluminum boiling is present. The fact that all particles maintained a similar temperature near the aluminum boiling temperature suggests that the peak temperature may be limited to the aluminum boiling temperature. Once boiling is reached the vapor reacts rapidly at the surface further propagating boiling.

The average peak temperatures from each particle sample did compare favorably with the average burn times from each particle sample. In general, the 18 nm particles had the shortest burn times and the highest peak temperatures, while the 50 and 80 nm samples had the longest burn times and lower peak temperatures; however, there is a approximately a $\pm$150 K uncertainty in the pyrometry measurements, and this trend is not statistically relevant outside of measurement uncertainty.

### 3.4.2 $CO_2$ Pyrometry Results

The $CO_2$ results showed an ambient temperature dependence on the particle peak temperature. At the higher ambient temperatures ($\sim$2500 K) the

particle peak temperature did not rise significantly above the ambient temperature. At lower ambient temperatures (∼2000 K) the peak temperature did rise above the ambient temperature. Figure 3.15 shows the high ambient temperature pyrometry trace. At the higher ambient temperatures the nanoparticles emit enough light to be observed behind the incident shock and a pyrometry temperature can be fit. In Figure 3.15 the particle temperature prior to shock reflection (t=0) is the incident shock ambient temperature and immediately after shock reflection the particle temperature rapidly increases to the reflected shock ambient temperature of ∼2500 K. As an aside, the rise in the temperature from incident to reflected shock coniditions occurs over the course of ∼20 $\mu$s and gives a good estimation for the time duration of the shock passage through the aersolized particle cloud. It is evident that the particle temperature does not significantly rise above the ambient temperature in either the incident or the reflected shock conditions.

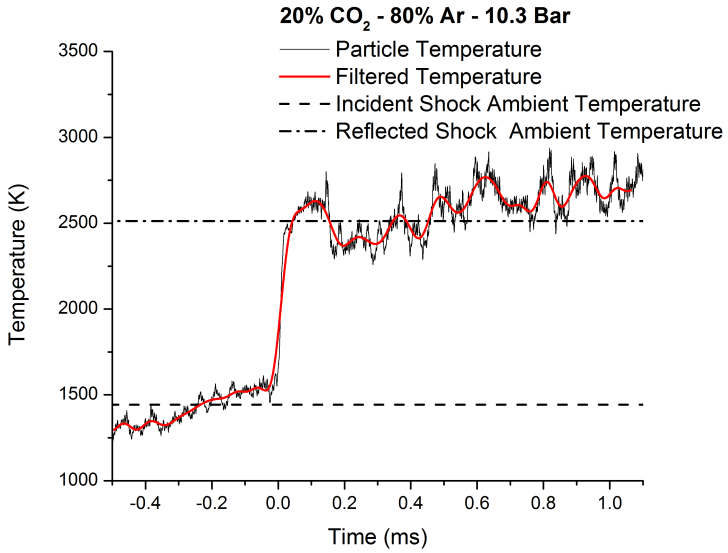


**Figure 3.15: Three color pyrometry temperature measurement of the nominally 50 nm aluminum particles combustion in $CO_2$ at 2500 K and 10 atm**

At lower ambient temperatures the incident particles do not emit enough light in order for a temperature to be fit prior to shock reflection consistent with the pyrometry results in air. This is due to the fact that when the reflected shock conditions are 2000 K rather than 2500 K the incident shock conditions are lower than 1000 K as compared to approximately 1500 K.

Emission at a single wavelength is exponentially related to temperature and so it is expected that the pyrometry trace would not detect emission at the incident shock temperature when the reflected shock temperature is 2000 K. At lower ambient temperatures the peak temperature is observed to rise above the ambient temperature as shown in Figure 3.16.

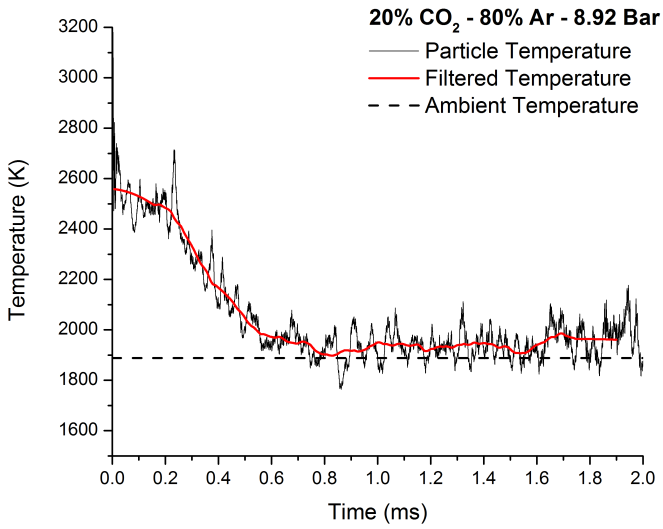


**Figure 3.16: Three color pyrometry temperature measurement of the nominally 50 nm aluminum particles combustion in $CO_2$ at 2000 K and 10 atm**

Figure 3.17 summarizes the peak temperature results for the 50 nm particle combustion in $CO_2$ environments. The trend of lower pressure and lower ambient temperature combustion leading to higher peak temperatures is unexpected. It is possible that the particles are pre-igniting behind the incident shock at higher ambient temperatures and this may explain in part why they are visible behind the incident shock. Bazyn observed nano-aluminum particles to ignite at temperatures as low as 1500 K, however, in the present results no luminosity was observed from particles when the reflected shock temperature was 1500 K previously suggesting they did not ignite at this low temperature. This may suggest that the particles were ignited previously at temperatures as low as 1500 K in $CO_2$ but the particle temperature did not peak but rather leveled off to the ambient intensity level giving no photometric evidence of burning.

At a given ambient temperature increasing the pressure will decrease the

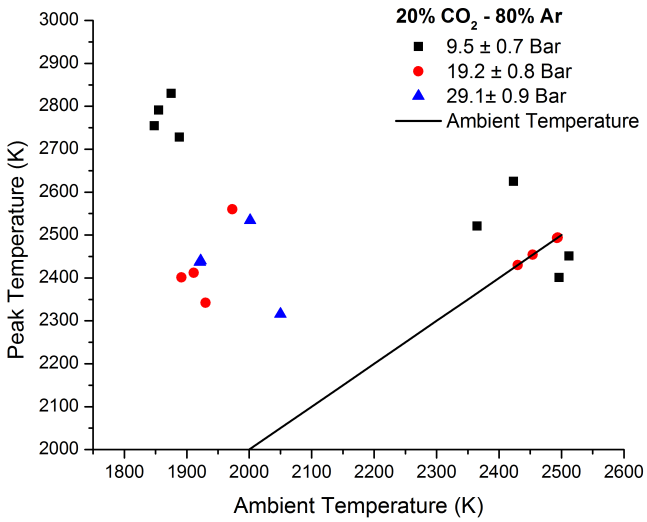


**Figure 3.17: Summary of peak temperature during 50 nm particle combustion vs. ambient temperature at various pressures in $CO_2$**

mole fraction of O, CO, and $O_2$ which are the primary reacting species. Yet, at the higher pressures the overall number density of these species is equal to or greater than the number density at lower pressures; and therefore the increase in particle temperature at lower pressures cannot be directly related to radical concentration unless molecular diffusion is less efficient at lower radical mole fractions.

The observed peak temperature may be due to experimental factors as well. For instance at higher pressures the particles may not be achieving full particle burn out. This would result in lower temperatures and shorter burning times. At 10 atm the particles may be achieving higher combustion completeness. It may also suggest that in $CO_2$ the luminosity may not be directly correlated to particle burn time due to a spectral effect. It was previously observed during spectroscopic measurements that the emission intensity was very strong under similar ambient conditions [25]. A final possible explanation is that the low initial pressures required to achieve the 10 bar final pressure promote a greater amount of air leakage into the test section. The presence of a small amount of air would promote high particle temperature while the majority of the burning would still occur with $CO_2$. This effect would not necessarily be as noticeable at 10 bar - 2500 K ambient conditions where the initial driven pressure would be higher than it is at 10

bar - 2000 K.

The observed duration of the temperature rise is similar to the observed burning time for the 2000 K and 10 atm $CO_2$ tests. At higher ambient temperatures an initial shorter peak is still present in the luminosity trace used for the burn time. Such a peak is not supported by the pyrometry traces which suggest the particle remains at the ambient incident and reflected shock conditions.

## 3.5 Burn Time vs. Peak Temperature Paradox

When considering the shock tube experimental results for the nano-aluminum particles that are combusting in air, the long burn time and high particle peak temperature results present a heat transfer paradox. The two parameters are intimately interlinked in that if the burn time is short it suggests that the particle is releasing energy more rapidly and should heat to a higher temperature, especially in the case of a surface combustion process. Therefore, a shorter burn time would presumably cause an increased peak temperature.

One of the greatest advantages of nanoparticles is the larger surface area to volume ratio. This advantage is what causes increased catalytic activity, reactivity, and overall performance in many systems. However, for nanoparticles the heat transfer from the particle is also expected to be sufficiently large due to the large surface area. A rudimentary analysis which assumes a spherical 80 nm particle with an even temperature distribution suggests that the particle must fully combust in less than 0.5 microseconds in order to reach 3000 K assuming a Nusselt number of 2, radiation to shock tube walls at 300 K as are found in the shock tube and a sufficiently large heat sink. The Nusselt number of 2 is the continuum regime solution for the heat transfer from a stationary sphere.

As discussed in Section 1.3 the continuum solution for particle heat transfer does not apply to nanoparticles. Yet, even when commonly used expressions for the heat transfer from nano soot are used ($Nu=0.3/Kn$) the a 80nm particle must combust in less than 1 microsecond in order to reach 3000 K. This solution results in a burn time that is two orders of magnitude smaller than experimental results would suggest. These simple analysis ignore any fundamental chemistry, and a model could be suggested where for instance 80% of

the particle combusts in less than 0.5 microseconds in order for the particle to reach 3000 K and the remaining 20% combust over the next 100 $\mu$s, however, such a mechanism is highly unphysical and is unsupported by the transient temperature profiles. The proposed mechanism where a large percentage of the particle combusts in a short time while the remaining percentage combusts over a long duration would result in a transient temperature profile that rapidly rises to 3000 K and then rapidly decreases to the ambient temperature where the particle finishes reacting. This result is not supported by experimental data.

Altman proposed that the accommodation coefficient for high temperature nanoparticles may be small ($\sim$0.005). Such a small accommodation coefficient would support the potential for high particle temperatures and relatively long burn times because very little heat transfer would occur to the surrounding gas molecules. The accommodation coefficient has not been directly measured for nano-aluminum/nano-alumina at any temperature and is relatively unknown. Those models that have considered the accommodation coefficient have primarily considered values $\sim$1 for lack of available data that suggests any deviation. The following section proposes a simple combustion model that will predict particle burn time and transient temperature profiles using various heat transfer assumptions and accommodation coefficients. The model will provide an estimate on the accommodation coefficient necessary to support the burn times and temperatures observed in experiment. This result will be compared to the predictions of Altman.

# CHAPTER 4

# NANO-ALUMINUM COMBUSTION MODEL

## 4.1 Model Description

A nano-aluminum combustion model was developed to further investigate the heat transfer of the particles. The model is an energy balance of the particle that assumes a surface-process limited combustion mechanism and heat transfer through conduction to the ambient gas and radiation to the walls of the shock tube at 300 K. Figure 4.1 depicts facets of the combustion model. The reaction surface is the initial surface area of the particle and does not change because diffusion of oxidizer and fuel are assumed to occur much faster than the limiting surface process (i.e. surface diffusion or chemical reaction).

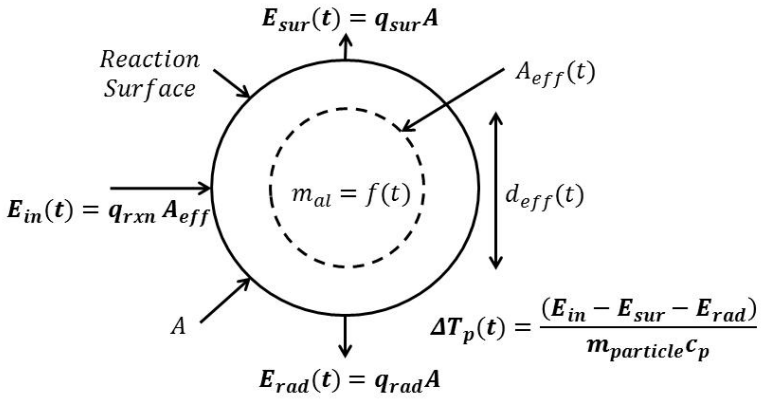


**Figure 4.1: Depiction of the surface process nano-aluminum combustion and heat transfer model**

The influx of heat to the particle is assumed to be due to the chemical reaction between the oxygen and aluminum following Equation 4.1, which releases $1.85(10^{-18})$ joules of energy for each collision of an oxygen molecule resulting in reaction with the aluminum surface. The rate of reaction is cal-

culated using the number density of oxygen at the particle surface (Eq. 4.2), thermal velocity (Eq. 4.3), the collision frequency (Eq. 4.4), and a sticking probability $\phi$ which is a variable parameter in the model. The velocity distribution in Eq. 4.3 assumes a Maxwellian distribution. This assumption ignores the chemical reaction occurring at the surface of the aluminum particle which consumes the oxidizer molecules; however, it will be shown that the model predicts very small sticking coefficients ($\sim$0.001), and in the limit of small sticking coefficients the velocity distribution approaches that of a Maxwellian distribution, and the assumption is considered valid.

The sticking probability represents the percentage of collisions that react and has a value between zero and one. A sticking probability of zero represents no reaction, and a sticking probability of one indicates each collision results in chemical reaction. The sticking probability is assumed to remain constant during the combustion of the aluminum particle. Equations 4.2-4.6 represent the calculation for the heat due to the reaction. An effective area is used for the influx of heat to model the reduction in the amount of aluminum surface area at the reaction surface during combustion. The effective area is determined by calculating the surface area of the remaining mass of aluminum at each time step as if it were a sphere. The assumption is that the reaction occurs at the outer surface of the particle, but as the particle burns the amount of reactive area decreases as a function of time following Eq. 4.5. A variable reaction area is chosen to account for changes in reactivity as the aluminum is depleted. As reaction occurs and oxide builds up on the surface, this barrier most likely impedes the oxidizer from reaching fresh metal. This effect can be simulated in our simplistic model by reducing either sticking probability ($\phi$) and/or reaction area ($A$) as a function of reaction extent. We, somewhat arbitrarily, choose the latter approach. The effect of including a time varying $\phi$ or $A$ alters the predicted transient temperature profile. Assuming the sticking probability or reactive surface area decreases with time results in the particle attaining an initial peak temperature followed by a temperature decay, which is similar to what was seen in experiment. If the product $\phi\ A$ is constant, then the particle temperature rises and remains at the peak temperature until particle burnout. The value of the peak temperature is relatively unaffected ($\leq$200 K) by this treatment, as the peak temperature occurs at the beginning of particle combustion when the reactive surface area is nearly equal to the outer particle surface area.

The model burn time using this method is increased more significantly as shown in Figure 4.2, however the constant reactive surface area gives an non-physical temperature profile. In terms of the estimated accommodation coefficient that will be discussed in the following section the reactive surface area has little effect on the interpretation of EAC magnitude. If instead the model used the constant reactive area the estimated EAC would be even smaller.

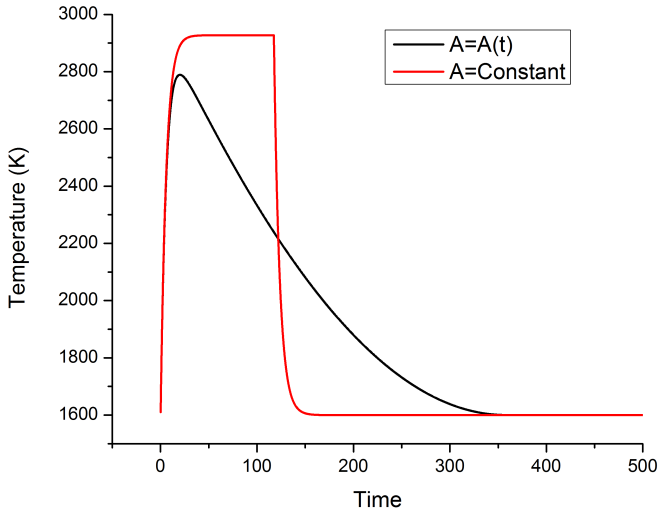


**Figure 4.2: Comparison of model transient temperature profile predictions using a constant reactive surface area and the the time varying surface area**

$$2\,Al + 3/2\,O_2 \rightarrow Al_2O_3 + 1.85\,(10^{-18})\,\frac{J}{Collision\,O_2} \tag{4.1}$$

$$N_{O_2} = \frac{X_{O_2}\,P}{T_a\,k_b} \tag{4.2}$$

$$c = \left(\frac{8\,k_b\,T_a}{m_{O_2}\,\pi}\right)^{1/2} \tag{4.3}$$

$$f = N_{O_2}\frac{c}{4} \tag{4.4}$$

$$A_{eff} = \left(\frac{6\,m_{al}}{\rho_{al}\,\pi}\right)^{2/3} \tag{4.5}$$

$$E_{in} = A_{eff} f q \phi \tag{4.6}$$

The conduction of heat to the surrounding gas is the key effect of interest in the present study. As previously mentioned, Altman predicts a decrease in the accommodation coefficient at high temperatures. Altman puts an upper limit on the accommodation coefficient $\alpha_E$ following Equation 4.7, where $\theta$ is the Debye temperature of the solid. For the conditions in this study Eq. 4.7 puts the upper limit of the accommodation coefficient at approximately 0.006. The heat transfer to the surroundings through conduction in the free molecular regime is calculated following Equation 4.8. Equation 4.9 shows the corresponding heat transfer equation assuming continuum mechanics, where $k$ is the thermal conductivity of the gas, $Nu$ is the Nusselt number, and $d$ is the particle diameter. The radiation to the walls follows the Stefan-Boltzmann law using Eq. 4.10 with an emissivity of 0.1 for alumina [65]. The temperature of the particle changes as shown in Eq. 4.11.

$$\alpha_E < \frac{1}{2\frac{C_v}{R} + 1} \frac{\theta^2}{T_g \, T_s} \tag{4.7}$$

$$E_{sur}(t) = \frac{\alpha_E \, P \, c}{8 \, T_a} \frac{\gamma + 1}{\gamma - 1} \left(T_p - T_a\right) \tag{4.8}$$

$$E_{sur}(t) = Nu \, \frac{k}{d} \left(T_p - T_a\right) A \tag{4.9}$$

$$E_{rad}(t) = \epsilon \, \sigma \left(T_p^4 - T_w^4\right) A \tag{4.10}$$

$$\Delta T(t) = \frac{E_{in} - E_{sur} - E_{rad}}{m_{particle} \, c_p} \tag{4.11}$$

## 4.2 Model Results

The model has two unknown parameters which must be fit to experimental data. These parameters are the sticking probability, $\phi$, and the energy accommodation coefficient, $\alpha_E$. The two independent unknowns are fit by comparing the predicted dependent variables of model peak temperature and burning time to the values obtained in the shock tube experiments. Figure

4.3a and Figure 4.3b show the model predictions graphically for an 80 nm particle. The burn time calculated in the model is independent of the heat transfer of the particle with the assumptions provided, and is plotted in black on the log scale. The particle is considered fully burned in the model once 90% of the original mass is reacted. A sticking probability of zero represents no reaction and therefore the burn time asymptotes towards infinity at this value. The particle temperature increases with increasing sticking probability as expected because a larger percentage of the collisions result in exothermic heat release.

Seven potential temperature profiles are plotted for comparison, each using a different accommodation coefficient or heat transfer assumption. Five accommodation coefficients, a correlation for the Nusselt number deduced from laser induced incandescence on nano-particles [44], and a Nusselt number of 2 are considered. For a given sticking probability the burning time and particle temperature considering one of the seven heat transfer models satisfy the energy balance of the system.

It is evident that an accommodation coefficient between 0.001-0.005 is necessary in order to achieve burn times greater than 100 $\mu$s and peak temperatures of $\sim$3300 K as indicated by the highlighted section of Figure 4.3b. The dashed box indicates the experimentally determined possible peak temperatures for sticking probabilities that give burning times also in the experimentally observed range. The best fit values for the accommodation coefficient and sticking probability are 0.0035 and 0.0009 respectively. The values obtained for the accommodation coefficient here match extremely well with the value of 0.005 found experimentally by Altman in previous work. These results clearly suggest that the nano-aluminum particles are experiencing thermal isolation from the ambient gas due to low energy accommodation coefficients.

Further comparison of the simple model with the experiment can be made by comparing the transient pyrometry temperature trace to the model predicted transient temperature profile. Figure 4.4 shows the predicted luminosity compared to pyrometry temperature from the experiment at 1500 K and 20 atm in air. For these traces the best fit accommodation coefficient of 0.003 and sticking probability of 0.0006 were chosen. The comparison between model and experiment is quite good.

The model predicts the peak temperature for each particle size to be ap-

proximately 3000 K, which is below the 3450 K boiling temperature of aluminum at 20 atm within uncertainty. It is likely that as the particle heats up some of the aluminum is volatilized and reacts at the surface of the particle limiting the peak temperature of the system to the boiling temperature of the aluminum at the given pressure. The peak temperature does not change significantly in the model with particle size because all modes of heat transfer scale similarly as shown in Table 4.1. The heat loss scales with $d^2$ and the heat due to chemical reaction scales with the effective area, but the peak temperature occurs near the start of the particle reaction when the effective area is very near the initial area of the particle. The model prediction that the peak temperature remains constant independent of the particle diameter agrees with the experimental data shown previously in Section 3.4. The model predicts the particle burn time to scale linearly with particle diameter as shown in Table 4.1. This result is inherent in the model design due to the assumption of a kinetically limited system.

| **Initial Particle Diameter** **nm** | **Burn Time** $\mu$**s** | **Peak Temperature** **K** |
|---|---|---|
| 20 | 140.1 | 2791.1 |
| 50 | 351.3 | 2789.3 |
| 80 | 562.4 | 2788.8 |
| 110 | 773.6 | 2788.6 |

**Table 4.1: Model predicted burn time and peak temperature at various initial particle diameters using $\phi$=0.0006 and $\alpha$=0.003**

The comparison extends to lower pressures as well. The model predicts a peak temperature of 2541 K at a pressure of 3.5 atm using the accommodation coefficient (0.003) and sticking probability (0.0006) as those used to fit the data at 20 atm. Pyrometry measurements found the temperature to be 2375K at 3.5 atm. The model slightly over predicts the temperature but considering the pyrometry uncertainty is very close. The accommodation coefficient used was fit to a system with the peak particle temperature of 2900 K and an ambient gas temperature of 1500 K. In the case of lower pressure, the peak temperature is lower and following Eq. 4.6, a lower particle temperature implies a higher accommodation coefficient if scaling applies which would further decrease the peak temperature at lower pressures closer to the experimental value.

A small accommodation coefficient has significant implications on the heat transfer of nano-aluminum particles and may give insight into why nanoparticles are capable of igniting at low ambient temperatures. As discussed previously, micron sized particles ignite at an ambient temperature of 2300 K in air upon the melting of the oxide layer. Nano-particles have been observed to ignite at ambient temperatures as low as 1200 K. Nanoparticle ignition at temperatures below 2300 K may be due to the low accommodation coefficient. Ignition occurs when the rate of heat production due to reaction reaches a threshold where the heat releases is greater than the heat losses so that a reaction can self-sustain. With a small energy accommodation coefficient, the ambient temperature at which this shift in heat transfer balance occurs may be at a much lower ambient temperature. Heat release due to slow reaction at temperature below ignition would not be significantly lost to the surroundings and would primarily go to raise the temperature of the particle. As the particle temperature rises, other rate limiting parameters such as diffusion and kinetics will increase further which will allow ignition to occur. Therefore, at equivalent ambient temperatures a nano-sized particle temperature could be higher than a micron-sized particle temperature. Ignition is primarily a function of particle temperature in aluminum combustion and this may explain nanoparticles low ignition temperature.

The possible effect of particle agglomeration on the results and conclusions is worthy of consideration. If nanoparticles agglomerate rapidly or are not efficiently de-agglomerated, then large agglomerates may still readily ignite at low temperatures but will coalesce and burn as larger particles. If agglomerates contain enough primary particles, the coalesced particulate may be large enough to burn in the diffusion limit, with correspondingly high temperatures.

In our arrangement, breakup of agglomerates is strongly promoted during injection and by the shock waves. During injection, the dispersed aerosolized particles are entrained in a jet of gas, then sent through an array of fine meshes that have been shown to effectively produce a well-dispersed cloud [87]. Petersen used a much milder form of injection [88] and directly measured particle sizes in the resulting cloud, finding little agglomeration of aluminum nanoparticles within the first minute after injection. Furthermore, it has been shown that the strong shear forces of the shock waves are effective at breaking weak agglomeration in nano-particles [77–79]. Thus, the experi-

mental evidence to date suggests clouds formed in the shock tube are, at the least, resistant to the formation of agglomerates.

Post shock agglomeration should also be relatively slow. Calculations considering an evenly dispersed thin cloud of particles behind the incident and reflected shock using the Smoluchowski monodisperse model, which ignores electrostatic forces, suggest that each particle will conservatively collide with less than two other nano-particles during the test time. In order for a nanoparticle to increase in size from 100 nm to 500 nm, it would require an agglomerate consisting of approximately 125 primary particles assuming spherical geometry. Heat transfer analysis of a 500 nm particle using the non-continuum heat transfer approximation still shows that the agglomerate particle must combust in less than 15 $\mu$s in order to reach 3000 K, still well below what is seen in experiment. Furthermore, the lack of significant AlO and Al emission during nano-particle combustion at 1500 K also suggests that it is not particles burning in the diffusion limit that is responsible for the measured temperature overshoot [39].

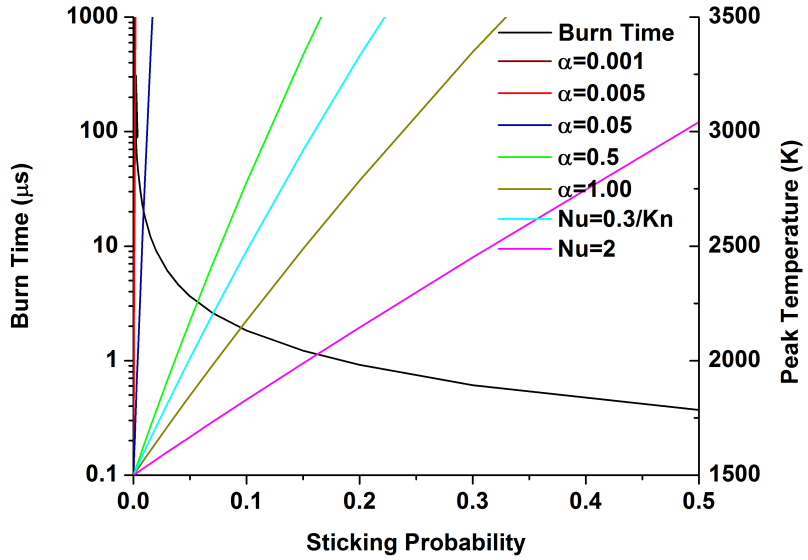


(a) Model results for an 80 nm particle comparing burn time and peak temperature at ambient conditions of 1500 K and 20 atm in air for sticking probabilities between 0-0.5

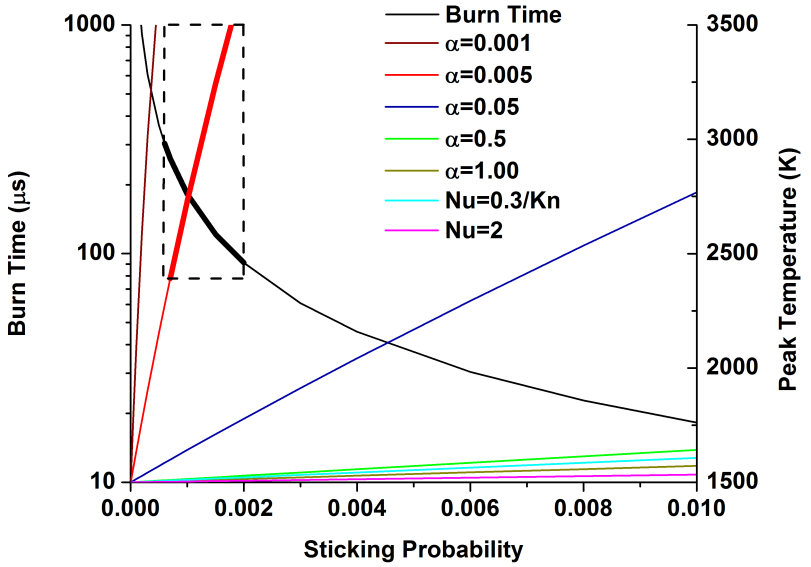


(b) Model results for an 80 nm particle comparing burn time and peak temperature at ambient conditions of 1500 K and 20 atm in air for sticking probabilities between 0-0.01

Figure 4.3

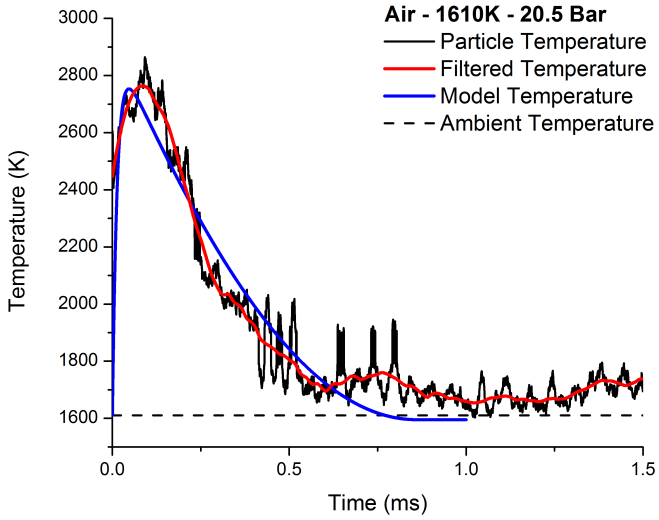


**Figure 4.4: Comparison of model transient temperature profile predictions using a constant reactive surface area and the the time varying surface area**

# CHAPTER 5

# HEAT TRANSFER EXPERIMENTS

## 5.1 TiRe-LII Results and Discussion

Modeling of the peak temperature and burning time of nano-aluminum particles agreed well with previous work by Altman suggesting a low accommodation coefficient [1, 50]. Since then, others have further suggested low accommodation coefficients in order to model the high peak temperatures seen in experiments [89]. However, it is necessary to directly measure the accommodation coefficient in order to decouple the predicted accommodation coefficient from the assumed combustion mechanism which leads to a large amount of uncertainty. Measurements of aerosolized nanoparticles have traditionally focused on measurements of nano-soot particle size distribution and concentration for post combustion diagnostic measurements [51–53]. Laser induced incandescence (LII) measurements are the primary method for performing optical particle size and concentration measurements. In order to interpret LII data for particles in the free molecular regime it is equally important to precisely determine the accommodation coefficient. A great deal of research has gone into accurately describing the accommodation coefficient of soot systems. Most results suggest the value to be between 0.18 and 0.5 [56]. The most effective experimental method to determine $\alpha$ is using time resolved LII (TiRe-LII) of a well described particle sample [51, 57, 58]. Computational Monte Carlo methods have also been used to predict the accommodation coefficient [47,48]; however, these models are highly dependent on the gas/surface interface potentials used in the model, and it is often necessary to validate such models with experimental data before the results can be extended to new particle systems.

Relatively little work has been done to describe the accommodation coefficient of metal and metal oxide nanoparticles systems. VanDer Wal has

performed preliminary tests and shown the LII method to be sensitive to particle concentration and size with a variety of metal nanoparticles including tungsten, iron, molybdenum, and titanium [59]. LII has since been used by other researchers to measure the accommodation coefficient, size distribution, and concentration of certain metal systems, primarily iron [57,58]. Kock and Eremin performed 2-color TiRe-LII measurements of the accommodation coefficient on iron nanoparticles in various gaseous environments. Eremin's results showed $\alpha$ to be 0.01, 0.2, and 0.1 for the Fe/He, Fe/CO, and Fe/Ar systems respectively. These values were significantly lower than those also found by Eremin for carbon systems (0.44-0.51). Koch's results showed $\alpha$ to be 0.13 for both the Fe/Ar and Fe/$N_2$ system. These results further suggest that the accommodation coefficient may be smaller than commonly assumed for the aluminum/alumina system, yet no experimental measurements have been performed to date.

In order to accurately describe nano-aluminum particle combustion it is necessary to have a valid estimate of the accommodation coefficient of aluminum oxide because the primary gas/surface interaction will occur on the oxide layer of the aluminum particle. The following work intends to extend the knowledge of the accommodation coefficient to systems of interest for nanoparticle combustion using 2-color TiRe-LII measurements of aluminum oxide nanoparticles with a well characterized size distribution. Alumina nanoparticles are used because the primary gas-surface collisional interaction occurs at the surface of the aluminum particle which is primarily aluminum oxide. Furthermore, alumina particles are less prone to agglomeration and are inert. The tests were performed in inert Ar, He, and $N_2$ at 300 K ambient temperature and varying pressures. The pressures were varied to scale the particle Knudsen number in the LII experiment to similar Knudsen values as those seen during shock tube combustion tests. The majority of the experiments were run at 2 atm of pressure.

A description of the experimental set-up and considerations for the LII experiment can be found in Section 2.3.2. In order to verify that the observed signal was due to particle incandescence rather than another laser induced emission process within the test gas, initial tests without particle injection were performed. Figure 5.1 shows the observed LII signal while the test chamber is under vacuum without injection (black), with the test chamber at 2 atm of argon without injection (red), and with the test chamber at 2

atm of argon with injection (blue). The observed signal with injection was significantly larger than without injection in either atmosphere indicating that the emission is likely due to particle incandescence. There is a small observed signal even without particle injection immediately after the laser pulse likely due to unavoidable incandescence from small dust particles within the chamber or inelastic scattering.

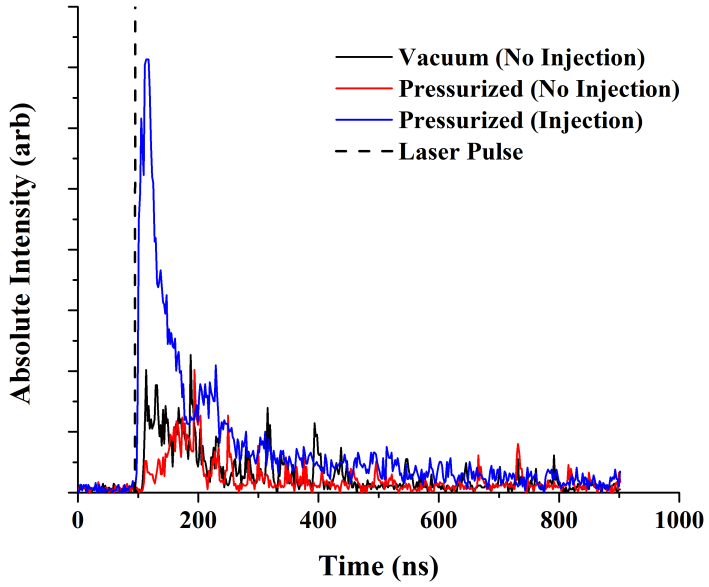


**Figure 5.1: LII signal at 705 nm after single laser pulse with and without particle injection. Tests were run with the test chamber under vacuum pressure and pressurized to 2 atm with argon prior to injection.**

In the free molecular regime of heat conduction there is a clear ambient pressure dependence on the heat transfer rate as shown previously in Equation 1.13 and reshown below in Equation 5.1. In the continuum regime the heat transfer is dominated by convection which is given by Newton's law of cooling as shown previously in Equation 1.11 and below in Equation 5.2 where Nu is the Nusselt number and k is the thermal conductivity of the gas. The Nusselt number for spherical particles in the continuum regime is 2 and is independent of pressure, and the thermal conductivity is relatively insensitive to pressure until very low pressures (∼100 Pa) are reached. Therefore, in the continuum regime the particle heat transfer is expected to be pressure independent. Figure 5.2 shows the pressure dependence of the LII signal

decay rate at 1.06 and 2.08 atm in helium at 705 nm. As expected in the free molecular regime the decay rate decreases with decreased pressure. The pressure dependence of the LII signal suggests that the observed LII is due to primary nanoparticles and not compacted clusters of agglomerated primary particles. The LII signals have been normalized, however this does not affect the interpretation because it is the decay rate which determines the pressure dependence.

$$q = \alpha \frac{c\,P}{8\,T_a} \frac{\gamma+1}{\gamma-1} (T_p - T_a) \tag{5.1}$$

$$q = Nu\frac{k}{d}A_s(T_p - T_a) \tag{5.2}$$

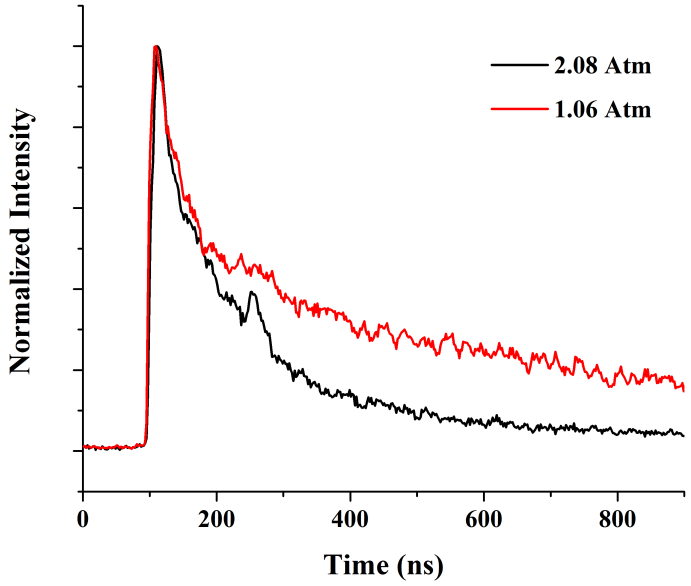


**Figure 5.2: Comparison of nanoparticle LII signal at 1.06 atm and 2.08 atm nm in helium monitored at 705 nm**

As discussed before, the measured temperature is not a true particle temperature but rather an effective particle temperature that is influenced by the particle size distribution within the collection volume. The temperature profiles will vary for each individual particle size within the distribution and must be properly weighted before comparison to the measured effective temperature. In order to do this the temperature profile for each individual

particle size bin within the distribution was modeled for a specified accommodation coefficient, and then the curves were properly averaged. Once the transient temperature profile for each particle size bin is calculated the temperature is converted to a transient intensity profile using Planck's law. The transient intensity profile for each particle size is then weighted by the particle size distribution frequency and particle radiating surface area ($d^2$) before all are summed together. This process is done at both 705 and 826 nm resulting in two transient intensity curves that are modeled for a selected accommodation coefficient and weighted by the particle size distribution and surface area. These modeled curves can then be used to calculate a modeled effective temperature using a similar procedure to that used to calculate a temperature from the measured intensity profiles at 705 and 826 nm.

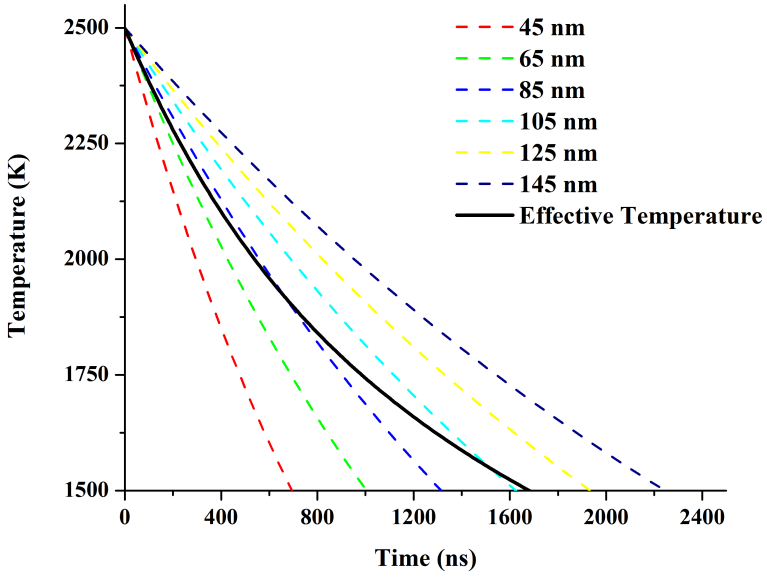


**Figure 5.3: Modeled transient temperature profile for various particle sizes with an accommodation coefficient of 0.1 and the resulting effective temperature modeled using particle size distribution shown in Section 2.5.2**

Figure 5.3 shows an example modeled temperature for various particle sizes and the resulting effective temperature distribution after proper weighting is considered. As expected pyrometry measurements are weighted towards the peak temperature of the system due the exponential dependence of Planck's law with temperature, as the temperatures decrease the effective tempera-

ture begins to more closely resemble the larger particle temperatures while early on the effective temperature more closely represents a direct average of all the particle temperatures. It must be noted that the accommodation coefficient is assumed constant for the range of particle diameters being considered. The calculated effective temperature is then compared to the measured temperature in order to determine the accommodation coefficient observed in experiment.

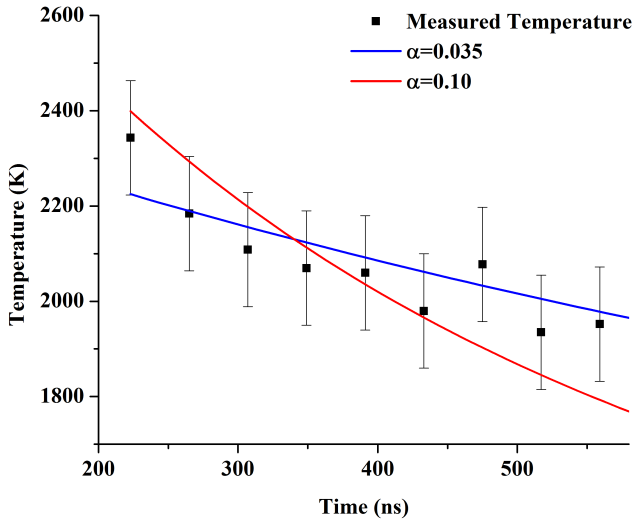


**Figure 5.4: Accommodation coefficient fit to the measured transient temperature profile for nano-alumina particles dispersed in nitrogen (N2) at 300 K and 2 atm. The two lines show upper and lower limits on the fit to an accommodation coefficient.**

Figures 5.4-5.6 show the experimental temperature measurements plotted alongside calculated effective temperatures using best fit accommodation coefficients. The uncertainty in the pyrometry measurements allows for a range of accommodation coefficients to fit the experimental data within the measurement uncertainty. The two lines represent upper and lower limits for fitted accommodation coefficients. The first 100 ns of the measured incandescence is not used in the fitting procedure due to previously mentioned concerns over various laser induced emission processes, as has been done [47]. The fit is performed until the signal to noise ratio in the incandescence becomes too large to obtain an accurate experimental temperature which occurs nearly 600 ns after the initial laser pulse in most experiments.

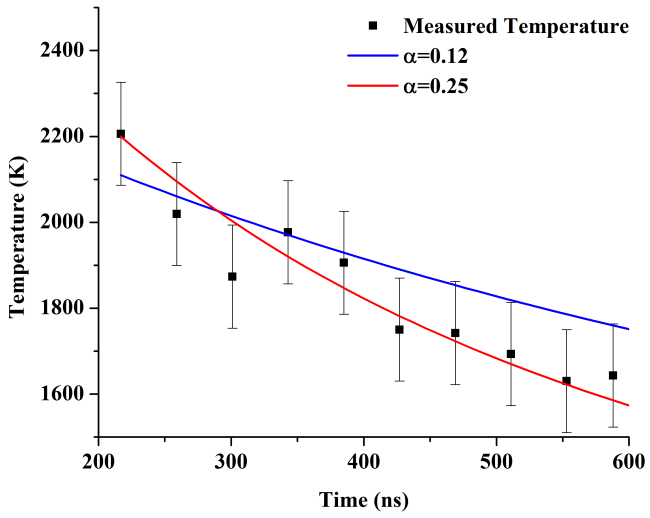


**Figure 5.5: Accommodation coefficient fit to the measured transient temperature profile for nano-alumina particles dispersed in argon (Ar) at 300 K and 2 atm. The two lines show upper and lower limits on the fit to an accommodation coefficient.**

Table 5.1 summarizes the accommodation coefficient fitting results. The results are similar to what has been seen by Eremin for metal nanoparticles. Eremin found an accommodation coefficient of 0.01 for iron nanoparticles in helium and a value of 0.1 for iron nanoparticles in argon [57]. Similar values were found in the present experiments and the uncertainty range is shown as well. From a molecular dynamics standpoint the two primary factors that influence the accommodation coefficient are the ratio of weight between the gas and surface atoms ($\mu$=$m_g/m_s$) and the gas/surface interface potential. Small values of $\mu$ suggest a small accommodation coefficient and therefore it is expected that the accommodation coefficient in helium is smaller than that of argon or nitrogen. In the alumina nanoparticle system greater complexity arises in determining trends because the condensed phase is a lattice of both oxygen and aluminum atoms. In recent work, molecular dynamic simulations have focused on the interaction of gases with monatomic condensed phases such as carbon or iron.

As previously stated it has been suggested that at high temperatures the accommodation coefficient of aluminum nanoparticles may be as small as 0.005 [40], as suggested by Altman who used Equation 5.3 to derive an up-

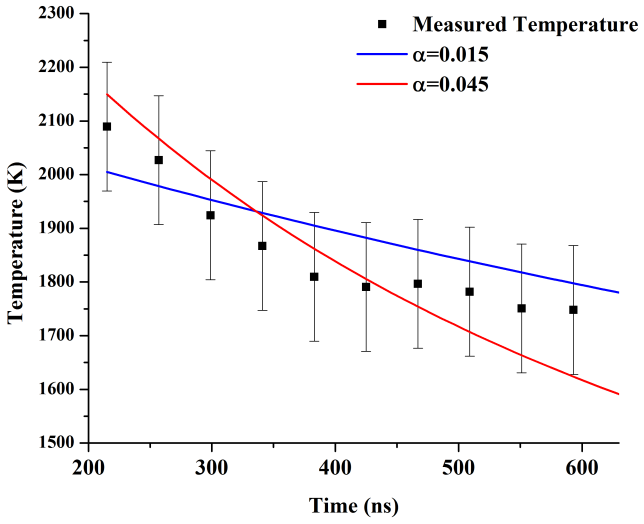


**Figure 5.6: Accommodation coefficient fit to the measured transient temperature profile for nano-alumina particles dispersed in Helium (He) at 300 K and 2 atm. The two lines show upper and lower limits on the fit to an accommodation coefficient.**

| Inert Environment | Accommodation Coefficient | Range |
|---|---|---|
| Helium | 0.03 | 0.015-0.045 |
| Nitrogen | 0.07 | 0.035-0.10 |
| Argon | 0.15 | 0.12-0.25 |

**Table 5.1: Measured accommodation coefficient for nano-alumina particles with Helium, Nitrogen, and Argon at 300 K and 2 atm.**

per limit on the accommodation coefficient where $\theta$ is the debye temperature of the condensed phase [1]. Equation 5.3 suggests an ambient and particle temperature dependence on the upper limit of the accommodation coefficient. Relatively little work has investigated the dependence of the accommodation coefficient on temperature. Michelsen attempted to derive a particle and gas temperature dependence for the accommodation coefficient using molecular beam data from Hager, Walther, and coworkers for the interaction of NO with graphite surfaces to be applied to soot particles [61]. Michelsen found an exponential decrease in the accommodation coefficient with increasing particle temperature. The data sets were not complete enough for the NO/graphite system to generate an overall accommodation coefficient as a function of the gas temperature. Michelson attempted to estimate the effect by extending

the values of the data set using linear extrapolation but little evidence support this method outside of the chosen data-set. Using this extrapolation it was found that the accommodation coefficient decreased with increasing temperature at gas temperatures below 1650 K and increased with increasing gas temperature above 1650 K.

$$\alpha_E < \frac{1}{2\frac{C_v}{R}+1}\,\frac{\theta^2}{T_g\,T_s} \tag{5.3}$$

While no such molecular beam data exists for the interaction of aluminum oxide with the gases of interest in aluminum combustion, the decrease in the accommodation coefficient with increasing particle temperature is expected to hold true for these systems. As the particle temperature increases the probability of the gas molecule being physisorbed to a surface for a sufficiently long time such that the internal and kinetic energy of the molecule is able to fully equilibrate with the surface is decreased. This effect is likely to hold true for the aluminum oxide surface.

The effect of ambient gas temperature on the accommodation coefficient is less certain. There are two different approaches to theoretically model gas-surface interactions, the classical model and the quantum-mechanical model. Goodman originally derived the classical model of ambient temperature dependence of the accommodation coefficient from lattice theory considering simplified gas-surface scattering interactions [45]. In the simplified lattice model the result showed that in all cases the accommodation coefficient initially decreased as ambient temperature increased until reaching a minimum value $\alpha_{min}$. As the temperature increased further the accommodation coefficient asymptotically increases toward $\alpha(\infty)$, slightly higher than $\alpha_{min}$ as discussed previously in Section 1.3.3.

Altman noted that the classical model of gas-surface interaction does not generally satisfy the principle of detailed balancing [50]. The quantum mechanical model does satisfy detailed balancing however an exact solution is said to present an unsolvable problem. Instead, Altman used detailed balancing to calculate an upper bound of the energy accommodation coefficient and noted that the result was that the EAC asymptotically approached zero with increasing ambient gas temperature as shown in Equation 8 which was supported by experiment [1, 50]. This result differs from the classical approach of Goodman which suggested that as ambient temperature increases

the accommodation coefficient asymptotically increases toward $\alpha(\infty)$, a value above zero. In either case, in the limit of high temperatures the increase in ambient temperature is likely to either decrease (Altman) the accommodation coefficient or have little impact (Goodman). Because of this the accommodation coefficients observed in the present experiments are likely upper limits for particle temperatures greater than ∼2300 K. Previous estimates of lower accommodation coefficients at higher temperatures suggest the approach by Altman may be more appropriate.

Extrapolation of the present LII results of nano-alumina to nano-aluminum combustion may also need more consideration due to the possibility of molecular collision resulting in chemical reaction. From a molecular dynamics viewpoint, those molecular collisions that result in significant residence time within the particle may also be those that lead to chemical reaction rather than heat transfer. This may suggest that, the accommodation coefficient for aluminum may be significantly lower during combustion than it would be in an inert environment because a portion of the collisions that would result in heat transfer in an inert environment may result in chemical reaction in a combustion environment. Even if true, however, the present result would again be an upper estimate on the accommodation coefficient.

## 5.2 Constant Volume Combustion Results

Preliminary constant volume combustion experiments were performed in an attempt to determine the macroscopic effects of a low energy accommodation coefficient on the energy release from an aersolized nanoparticle dust cloud. The transient pressure response was monitored, and an example pressure trace is shown below in Figure 5.7. In this pressure trace, a significant pressure rise is observed which is similar to what has been seen previously in constant volume combustion experiments [76, 90]. The shape of the transient pressure trace suggest that the internal particle distribution is relatively uniform. Significant non-uniformity in the particle concentration within the chamber would manifest in sharp increases in pressure as the flame front propagated through an area of high particle concentration. These effects were not observed, and furthermore results from same condition experiments were highly repeatable.

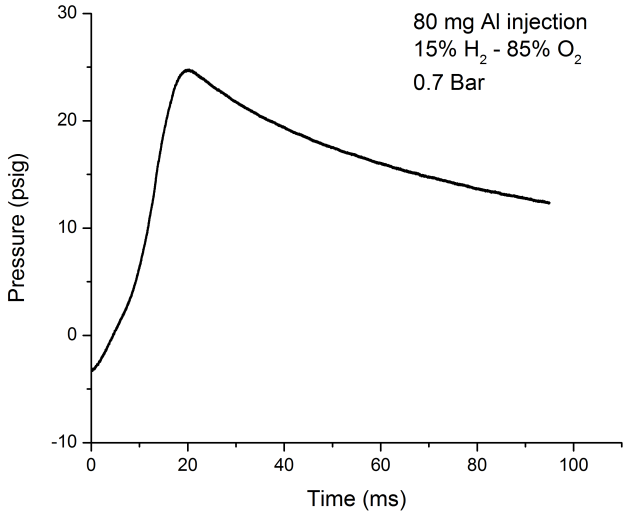


**Figure 5.7: Transient pressure profile for constant volume combustion experiments with 80 mg of 20 nm aluminum injected into the chamber at 0.6 bar and 15%$H_2$-85%$O_2$**

Tests were performed within the constant volume combustion chamber in order to determine the effect of aluminum mass loading, initial pressure, and oxidizing concentration. Figure 5.8 shows the effect of increased loading of nano-aluminum particles within the constant volume chamber. As the loading of aluminum particles is increased the peak pressure and the rate of pressure rise ($dp/dt$) are significantly increased due to increased aluminum combustion. This effect suggests that nano-aluminum is significantly contributing to the overall pressure rise as expected. In both Figure 5.7 and Figure 5.8 the timescale observed for the pressure rise is significantly greater than the previously observed single nanoparticle burning times in the shock tube. In the constant volume combustion experiment the pressure rise timescale is dependent on the rate the flame front prppagation. In this specific experiment the ignition occurs in the center of the chamber and the flame propagates towards the chamber walls. Even though the combustion propagation is a spatially varying event the pressure within the chamber is likely near uniform because pressure equilibrates within very few molecular collisions. The spatial temperature distribution is highly varying inside and outside of the flame front because temperature does not equilibrate as rapidly as pressure.

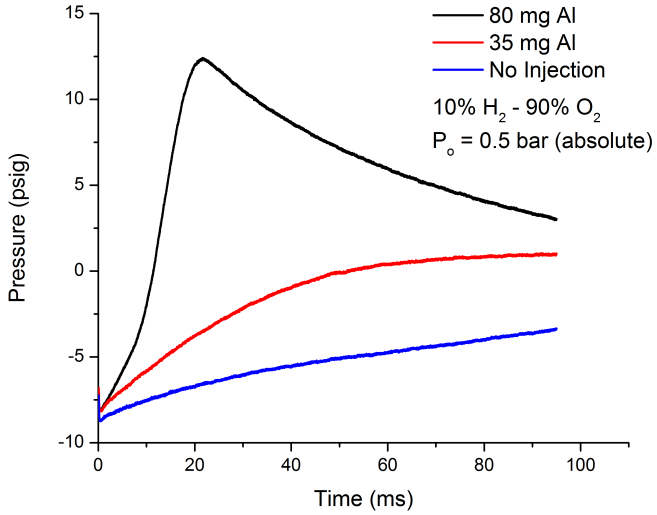


**Figure 5.8: Transient pressure profile for constant volume combustion experiments with various amounts of nano-aluminum injected into the chamber at ~0.45 bar and 15%$H_2$-85%$O_2$**

In the observed pressure rise without aluminum injection the pressure rise is due solely to the combustion of hydrogen with oxygen in a dilute mixture. Similar experiments have been performed in order to measure the laminar flame speed of hydrogen [90]. In stoichiometric mixtures of hydrogen and air the flame speed has been observed to be approximately 2 m/s, while in dilute mixtures the flame speed is less than 0.25 m/s [90]. In the present set-up, the ignition source is approximately 2" in distance from the ignition source, and therefore the pressure peak is not expected to occur until ~200 ms after ignition. In fact, this agrees relatively well with test data that show the pressure peak without aluminum injection to occur near 150 ms after ignition. The change in laminar flame speed at various equivalence ratios is due to the laminar flame speed dependence on temperature and pressure. The flame speed pressure and temperature dependence presents an issue when attempting to determine heat release due to aluminum that is ignited in a mixture of hydrogen because the flame speed of the hydrogen will be greater when aluminum is participating in combustion event. Aluminum combustion will increase the temperature and pressure which will result in an increased hydrogen flame speed with similar intial concentrations. Varying flame speeds result in varying amounts of heat loss to surroundings which

will be discussed in greater detail below. Therefore, the pressure rise due to hydrogen/oxygen combustion will likely vary depending on the presence of aluminum combustion.

In order to perform the equilibrium calculation an assigned specific volume is necessary which is determined based on the mass load of the constant volume chamber. Table 5.2 shows the predicted temperature and pressure using the NASA CEA constant volume equilibrium calculation for different loading conditions. As the loading increases the predicted adiabatic temperature and pressure increase accordingly. The energy release of aluminum contributes greatly to the predicted final pressure. The final pressure is approximately 3.5 times higher with the addition of 40 mg of aluminum than it is without aluminum addition. The adiabatic flame temperatures are actually higher at lower initial pressures due to the lower total heat capacity of the gas within the chamber.

| | Final Temperature (K) | | | Final Pressure (bar) | | |
|---|---|---|---|---|---|---|
| Gas Environment | 0 mg | 40 mg | 80 mg | 0 mg | 40 mg | 80 mg |
| 5%$H_2$-95%$O_2$-0.4 bar | 823 | 3139 | 3738 | 1.09 | 3.89 | 4.74 |
| 10%$H_2$-90%$O_2$-0.4 bar | 1291 | 3218 | 3756 | 1.65 | 3.95 | 4.75 |
| 5%$H_2$-95%$O_2$-0.5 bar | 823 | 2953 | 3584 | 1.35 | 4.57 | 5.60 |
| 10%$H_2$-90%$O_2$-0.5 bar | 1291 | 3068 | 3619 | 2.07 | 4.70 | 5.62 |

**Table 5.2: Adiabatic combustion temperature and pressure predicted for CVE experiments using equilibrium calculations**

The equilibrium pressure rise expected for a 10%$H_2$ dilute mixture in oxygen (no aluminum) with an initial pressure of 0.45 bar (absolute) in the given chamber is 1.86 bar. The pressure rise observed during experiment was only 0.94 bar (absolute), which is only 50% of the theoretical value. In similar experiments using stoichiometric methane/air mixtures, Santhanam found the experimental value to be 83% of the theoretical maximum [76]. The lower efficiency in the present experiments is attributed to the slower flame speed in the dilute mixture of hydrogen/oxygen and the smaller chamber volume resulting in greater heat loss throughout the duration of flame propagation. It is expected that when the pressure rise is more rapid (higher flame speed) significantly less heat loss to the surroundings will occur while the flame is

propagating due to a shorter timescale over which losses may occur.

In the equilibrium equation the system is considered to be adiabatic. This assumption grows increasingly suspect as the flame speed within the constant volume decreases. Not only do radiation losses scale linearly with propagation duration, but a decreased flame speed also results in an inversely large flame thickness. The larger flame thickness leads to greater conductive heat loss to the ambient walls and ignition probes with the possibility of quenching arising.

Results have shown that the addition of aluminum decreases the time required to reach the maximum pressure by an order of magnitude from $\sim$200 ms to $\sim$20 ms. Accordingly, the flame thickness will be an order of magnitude smaller resulting in less heat loss to the surroundings. The faster flame speeds and greater combustion efficiencies of Santhanam support the heat loss argument [76]. Therefore, while only 50% of the theoretical energy in the hydrogen/oxygen mixture is observed in the peak pressure, this percentage is likely to increase as the flame speed increases with the addition of aluminum.

In order to gain an estimate of the combustion completeness Energy Dispersive Spectroscopy (EDS) using a JEOL 6060LV general purpose scanning electron microscope (SEM) was performed on collected post-combustion particles. The EDS analysis is used to determine oxygen and aluminum concentration in a sample. The theoretical atomic concentration for aluminum and oxygen with an aluminum oxide particle are 40% and 60% respectively. The theoretical atomic concentration of aluminum and oxygen within an aluminum particle will vary depending on oxide thickness within the limit between $40\% \leq N_{Al} \leq 100\%$ and $0\% \leq N_O \leq 60\%$ respectively.

The EDS has a limited penetration depth into a sample and therefore the measured atomic oxygen concentration is skewed towards higher oxygen concentrations due to the oxide layer on aluminum particles. Furthermore, the EDS measurement of oxygen is only semi-quantitative because the detector sensitivity is not constant, and large correction factors are needed in order make it a true quantitative measurement. It has been shown that relative comparisons between pure Al, pure $Al_2O_3$, and the combusted aluminum particles can be used in order to quantify combustion completeness [13]. In order to make a quantitative analysis, the EDS measurement was performed on the 80 nm alumina nanoparticles discussed in Section 2.5.2, uncombusted nano-

aluminum particles, and post-combustion collected nanoparticles. Peuker showed previously that the concentration of oxygen was linearly dependent within a sample using this methodology [13].

| | Atomic Concentration | |
|---|---|---|
| Sample | %-Oxygen | %-Aluminum |
| Aluminum (initial) | 42.5 | 57.5 |
| Aluminum (Post-Test) | 46.0 | 54.0 |
| Alumina (Reference) | 49.3 | 50.7 |

**Table 5.3: Atomic mass fraction of collected sample and references using EDS analysis**

Table 5.3 shows the EDS measured aluminum and oxygen atomic concentration within each sample. The measured atomic fraction of aluminum and oxygen values were within the range previously discussed. The alumina reference sample did not result in the theoretical ratio of aluminum/oxygen however this is likely due to previously discussed instrumentation sensitivities. It is observed that the combusted particle oxygen concentration falls between the range of oxygen concentration for the unreacted nano-aluminum particles and the reference nano-alumina particles. A linear fit suggests that 51.8% of the collection sample had reacted during the experiment. Santhanam found combustion efficiencies ranging from 60%-90% measured by comparing the peak pressure to the theoretical peak pressure considering full combustion. The value found presently is slightly less which may again be due to wall quenching effects that are expected to be greater in the present set-up.

With knowledge of the combustion efficiency for a given initial set of conditions the theoretical pressure rise can be compared to the measured pressure rise expected for the measured combustion completeness. The primary tests were performed in 10%$H_2$-90%$O_2$ initially at ∼0.5 bar and 300 K. In the case of 80 mg injection of nano-aluminum particles the peak pressure was found to be 1.85 bar (absolute) as shown in Figure 5.8. In the same conditions the combustion efficiency was found to be 51.8% which would suggest that the theoretical peak pressure for the experimental system is 4.73 bar. The observed pressure is slightly less than 40% of the theoretical output which would

suggest the other energy is lost due to heat transfer with the surroundings.

Determining the fraction of energy that is lost to the surroundings due to wall conduction and radiation presents a signficant challenge. Ideally, it would be assumed that the initial pressure rise occurs rapidly such that non-radiative heat losses may be ignored on the short time scale; however, decreases in flame speed previously attributed to wall quenching suggest that this may not be an accurate assumption. Large radiative losses would support the estimation of a low energy accommodation coefficient observed in previously discussed experiments; however, Santhanam et al. suggested radiation may be the dominant form of heat loss within the flame zone in experiments using micron sized particles [76] regardless of the accommodation coefficient. Development of a heat transfer model between the flame zone and the unburned mixture requires assessing a significant number of poorly known flame characteristics such as flame emissivity, preheat zone thickness, and optical thickness. Such a model is outside the scope of the present work and therefore determining the percentage of the heat losses that go into conduction/radiative modes is not easily ascertained.

Experimentation has shown that only 40% of the theoretical energy from mixture combustion is observed in the peak pressure measurement even when the combustion completeness is accounted for. The lost energy is assumed to be lost via radiation and conduction; however, quantification of the amount lost in each mode is beyond the present experimental scope. Santhanam suggested that at high flame temperatures a significant amount of the energy lost is due to radiation without considering non-continuum heat transfer for micron sized particles. Consideration of a low EAC would further increase the energy lost due to radiation, and in fact, the present experiments with nanoparticles suggest higher losses than those found by Santhanam et al for micron sized particles. A lower energy accommodation coefficient is one of multiple possible explanations for the large amount of heat losses. Therefore, while at the macroscopic level it cannot be directly deduced that a lower energy accommodation coefficient is observed, the heat losses account for greater than 60% of the theoretical heat release.

# CHAPTER 6

# CONCLUSIONS AND RECOMMENDATIONS

## 6.1 Summary and Conclusions

This work provided included a significant parametric study measuring characteristic combustion parameters of shock heat nano-aluminum particles. The results of this parametric study were used to develop a simple nano-aluminum combustion model that considered various heat transfer mechanisms from the nanoparticle. The results of the model showed that the burn times and peak temperatures observed in the parametric study were only reconciled if the heat transfer from the nanoparticle to the ambient gas through conduction/convection is relatively inefficient. This result was supported by previous work by Altman who predicted a low accommodation coefficient for high temperature nanoparticles in high temperature ambient environments. In order to further investigate this phenomenon laser induced incandescence experiments were performed in order to directly measure the accommodation coefficient decoupled from a combustion event. This measurement further supported the notion of a small energy accomodation coefficient; however, it was not as low as those suggested at combustion temperatures using the combustion model. The LII experiments were performed at lower ambient temperature, the interpretation and scaling to higher ambient temperatures was investigated. Constant volume experiments were used in order to determine the macroscopic effect (if any) on the low energy accommodation coefficient.

- Emissivity measurements of nano-aluminum within the heterogeneous shock tube have shown that:
  - The relative emissivity at 705, 826, and 905 nm changes with the phase change of nano-alumina. At temperatures above the melting

temperature of alumina (∼2300 K) the wavelength dependence of the emissivity is close to $\lambda^{-0.92}$ while at temperatures below the melting temperature the wavelength dependence is closer to $\lambda^{-2.45}$. The shift was not shown to be a stark jump in emissivity but rather a relatively gradual shift in the range of temperatures between 2000 and 2500 K.

- Spectroscopic measurements investigating the emission of the nano-aluminum combustion have shown that:
  - In both air and $CO_2$ environments at ambient temperatures between 1500-2000 K and at pressures ranging from 3-30 atm no gas phase emission of AlO or Al vapor was present.
  - The emission during combustion gave off primarily a thermal radiation signature indicating that the primary emission was due to condensed phase radiation.
  - When the thermal radiation is modeled using emissivity assumptions previously characterized the temperature fit is above the ambient environment temperature suggesting that the particle rise above the ambient temperature. This result is further supported by pyrometry measurements
  - The lack of gas phase emission is supported by previous work by Lynch suggesting very little gas phase presence through absorption measurements at similar temperatures. These findings suggest a surface combustion process potentially similar to the shrinking core model.
- Photometric measurements investigating the burn time of the nano-aluminum particle samples in air have shown that:
  - Ignition of the nano-aluminum particles was observed at temperatures as low as 1500 K in air.
  - The burn times for 50 nm particles in air were found to be highly dependent on ambient temperature and ambient pressure. The pressure dependence was found to be nearly linear for the case of 50 nm aluminum particles which is predicted by a surface process limited combustion. This gives further evidence that the primary

reaction is happening at the surface of the particle as predicted by a shrinking core type model. Gas phase diffusion flames have previously been shown to have very little ambient temperature and pressure dependence as described by the Beckstead correlation.

- The burn times for 50 nm particles in air were between 200-600$\mu$s for pressures between 10-30 atm at temperatures between 1500-1650. The burn times were found to be between 50-200$\mu$s for 50 nm particles at pressures between 10-30 atm and temperatures between 1850-2050 K.
- The activation energy for aluminum combustion in air was calculated to be between 63.4-74.9 kJ/mol which varied with pressure. Higher pressures had lower calculated activation energies. These values compared favorably with previous values found in the literature.
- The activation energy for aluminum combustion in air was calculated to be between 63.4-74.9 kJ/mol which varied with pressure. Higher pressures had lower calculated activation energies. These values compared favorably with previous values found in the literature.
- The 20 nm particle sample consistently showed shorter burn times than all other particle samples (50, 80, 110 nm). Determining a diameter dependence on the particle burn time was not feasible due to the high variation in particle diameter within each sample. However, tests showed that the 20 nm particles had the shortest burn time while all other samples had relatively similar burn times.
- At temperatures near 2500 K the luminosity trace gave late time intensity increases that were attributed to the ignition of larger particles within the sample that would not have been seen to ignite at lower ambient temperatures. This late time phenomenon disallowed a burning time to be quantified at these temperatures. The late time phenomenon may have also been attributed to gas phase combustion progression from the nanoparticle.

• Photometric measurements investigating the burn time of the nano-

aluminum particle samples in $CO_2$ have shown that:

  - Ignition of the nano-aluminum particles was observed at temperatures as low as 2000 K in 20%$CO_2$-80% Ar.
  - The burn times for 50 nm particles in $CO_2$ were found to be highly dependent on ambient temperature and ambient pressure similar to the result found in air. The pressure dependence was again found to be nearly linear for the case of 50 nm aluminum particles which suggests the particles are undergoing a surface process combustion in $CO_2$ as well as air.
  - The burn times for 50 nm particles in $CO_2$ were significantly longer than those observed in air as expected. The burn times were between 300-600$\mu$s for pressures between 10-30 atm at temperatures between 1900-2050 K. The burn times were found to be between 50-150$\mu$s for 50 nm particles at pressures between 10-30 atm and temperatures between 2400-2500 K.
  - The burn times were approximately 5 times longer in $CO_2$ compared to tests at similar temperatures in pressures in air. An analysis of the gas composition at the temperatures and pressures suggests that the reactions involving monatomic oxygen may be the key kinetic rate limiting step. At 2000 K and 10 atm the concentration of monatomic oxygen is approximately 6.7 times higher in air than it is in an initial mixture of 20%$CO_2$-80%Ar which is similar to the ratio in burn times.
  - The activation energy for aluminum combustion in air was calculated to be between 103-113 kJ/mol which varied with pressure. Higher pressures had lower calculated activation energies. These values compared favorably with previous values found in the literature.

- Pyrometry measurements investigating the condensed phase temperature of the nano-aluminum samples during combustion in air have shown that:

  - The peak temperatures observed during nano-aluminum combustion at 1500 K were highly pressure dependent. At high pressures

(∼20 atm) the peak temperature was seen to rise near 3000 K. At lower pressures (∼3.5 atm) the peak temperature remained relatively near the ambient temperature.

  - The duration of the temperature increase compared favorably to the duration of luminosity observed in the burning time measurements. The shortest (duration) pyrometry traces corresponded to the 20 nm particles which also had the shortest burn times as measured from luminosity.
  - The particle peak temperature was relatively insensitive to the sample diameter (20, 50, 80, 110 nm) within the uncertainty of the pyrometry measurement.
  - The peak particle temperatures observed remain below the vaporization temperature of aluminum for all tests. The peak temperature also becomes relatively insensitive to pressure above 20 atm suggesting that a potential heat sink (boiling of aluminum) begins to occur once a given peak temperature is reached that limits the particles overall peak temperature.

- Pyrometry measurements investigating the condensed phase temperature of the nano-aluminum samples during combustion in $CO_2$ have shown that:

  - At higher ambient temperatures (∼2500 K) and any pressure, the particle emission can be observed during the incident shock and reflected shock. The particle temperature is observed to remain at the incident and reflected shock temperatures.
  - At lower ambient temperatures (∼2000 K) and low pressures ∼10 atm the ambient temperature is observed to rise above the ambient temperature. This phenomenon is unexpected and may suggest that at higher ambient temperatures pre-ignition of the particles is occurring. It also may suggest that combustion mechanism is changing although this is not evidenced in the luminosity traces used in the burning time measurements.
  - At lower ambient temperatures (∼2000 K) the higher ambient pressures resulted in lower peak temperatures which is inconsistent

with the results observed in air. However, this may be in part due to the fact that higher ambient pressures will result in a lower mole fraction of oxidizing radicals.

- A combustion and heat transfer model for nano-aluminum was created for nanoparticles combusting in air at temperatures between 1500-2000 K. The model results have shown that:
  - The observed pressure and temperature dependencies of nano-aluminum combustion can be explained by a surface limited combustion process that considers the flux of oxygen molecules to the surface of the paricle through molecular diffusion.
  - The high peak temperatures and long burn times may be explained if a low energy accommodation coefficient ($\sim$0.005) is considered similar to that predicted by Altman.
  - The model predicts a particle diameter dependence of $d^1$. This is implicitly determined due to the model set-up.
  - The transient temperature profile of the nano-aluminum model suggests that the effective area of the reactive surface decreases as the reaction progresses which is supported in the idea of the shrinking core model.
- Time-resolved laser induced incandescence measurements were performed to directly measure the accommodation coefficient decoupled from the combustion mechanism to show that:
  - The measured EAC value was 0.03, 0.07, and 0.15 in Helium, Nitrogen, and Argon respectively at an ambient temperature of 300 K and 2 atm.
  - The observed values are well below traditional assumptions and similar in value to those found for nano-iron particles by Eremin. The values are similar to what Altman's expression would predict at similar temperatures and pressures ($\sim$0.06); however, these values are an order of magnitude higher than the values estimated at higher ambient temperatures.

  - The measurements suggests that Altman's ambient temperature scaling may be more appropriate than Goodman's ambient temperature scaling.

- Constant volume combustion measurements in dilute hydrogen oxygen mixtures were performed to show that:
  - Observed pressure rises without injection of nano-aluminum particles agreed well with flame speed measurements performed in constant volume experiment mixtures of hydrogen and air.
  - Increasing the nano-aluminum concentration within the constant volume chamber increased both the peak pressure and rate of pressure rise, suggesting that nano-aluminum combustion was contributing to the overall combustion. The peak pressure observed with nano-aluminum injection was greater than the theoretical maximum energy release considering hydrogen combustion alone.
  - EDS measurements were performed to determine the combustion completeness of collected nano-aluminum post-experiment samples. Measurements suggest that approximately 50% of the aluminum had reacted during the experiment.
  - Comparison with theoretical adiabatic constant volume equilibrium calculations suggest that only 40% of the energy released during combustion (accounting for combustion completeness) was observed in the peak pressure rise. The losses are attributed to radiation and conduction to the walls.
  - The amount of energy lost into each mode of heat transfer is not directly calculable and therefore an energy accommodation estimate cannot be obtained, however, the large amount of heat loss support a low energy accommodation. This effect was equally explained by Santhanam for micron sized particles as due to radiation losses without consideration of a low EAC.

## 6.2 Recommendations for Future Work

### 6.2.1 Extension to other nanoparticles

The present experiments were performed primarily on nano-aluminum and nano-alumina particles, however, the results may be able to encompass a larger sample of metal and metal oxide particles. The transition from continuum heat transfer to free molecular heat transfer and the transition from diffusion controlled combustion to surface limited combustion is predicted due to particle size scaling and is independent of species. Therefore, the present results may extend to other nanoparticles. Specifically, it may extend to those likely to react at the particle surface. Particles such as boron and silicon are likely candidates for which the present combustion results might extend.

Furthermore, the heat transfer analysis has supported previous theory proposed by Altman. This theory relies on the Debye temperature of the solid material but otherwise is material independent and can extended outside the scope of the present work. The reliance of Altman's theory on the Debye temperature of the solid is also worth further investigation. Debye theory traditionally applies to crystals while many of the powders used in combustion on the micron scale are amorphous and have defects. The presence of these defects likely will change the particles ability to accommodate heat transfer. This will require investigation into the fundamental molecular dynamics of liquids and solid materials.

### 6.2.2 High Temperature TiRe-LII

The TiRe-LII measurements performed in the present set of experiments were performed at ambient 300 K temperature. There is very little literature outside of the prediction by Altman that investigates the effect the ambient gas temperature has on the energy accommodation coefficient. In the previously discussed results, the EAC estimated using the combustion model is significantly lower than the EAC measured at ambient 300 K. This is predicted by Altman, but should be further investigated in order to verify. In order to do this TiRe-LII measurements should be performed on nanoparticles at hight temperatures.

The most direct way in which to measure the the EAC at high temperature is to perform the measurement on flame synthesized particles or flame heated particles. Flame synthesis is most desirable as agglomeration will more readily be avoided. Low pressure flames have been used to produce unagglomerated nano-phase particles [91]. Similar flames could be used to produce nanoparticles with which laser induced incandescence could be performed at high ambient temperatures. Difficulty may arise in separating emission from other flame processes/species from the incandescence of the particle after the laser pulse. Extending the accommodation coefficient to higher temperatures this way will add significantly to the literature and to nano-aluminum combustion knowledge. Furthermore, this process can be extended to other metal oxides of interest including titanium oxide, silicon oxide, and potentially others.

### 6.2.3 Molecular Dynamics Simulation

Molecular dynamics (MD) has more recently begun use in predicting the energy accommodation coefficient for various systems. Daun et al. has used it to predict both soot and nickel nanoparticle energy accommodation coefficients [47]. Previously, experimentation has been the only reliable way in which to predict the EAC, however, it is nearly impossible to measure the EAC at all temperatures, pressures, and ambient gas environments needed in order to extrapolate results to real combustion systems using these particles. Therefore, a single value is commonly used and assumed across all conditions. Molecular dynamic simulations present an opportunity to create models which can be compared to accurately measured systems and then extended in order to determine factors such as temperature and gas composition dependence. This would add tremendous knowledge to the nanoparticle gas/surface literature.

The molecular dynamics approach begins by defining potential energies between the atoms within the nanoparticle surface as well as pairwise potentials between the gas molecule and the surface atoms. Interatomic forces are calculated by differentiating the interatomic potentials with respect to displacement. Once forces are known, the gas molecule and surface atom trajectories are calculated using Newton's equations of motion throughout

the scattering event [47]. This process is used within a Monte Carlo simulation that considers all possible incident gas molecular velocities to obtain the accommodation coefficient. The gas velocities are calcualted from a Maxwell-Boltzmann distribution at the gas temperature. This process lends itself well to performing simulations to compare to low temperature EAC data and extrapolating to higher temperature by varying the Maxwell Boltzmann distribution. The most difficult aspect of the MD simulations is obtaining an accurate interatomic potential. Daun compared results using ab initio derived Morse potential as well as the Lorentz-Berthelot derived Lennard-Jones potential to find that the Morse potential was significantly more accurate when compared to experimental data [47].

The application of the MD simulation to the combustion event may also raise issues in interpretation. From a molecular dynamics standpoint the chemical reaction potentials may not be necessarily decoupled from the heat transfer. Those molecular collisions that result in significant residence time within the lattice may also be those that lead to chemical reaction rather than heat transfer. This may suggest that, the accommodation coefficient for aluminum may be significantly lower during combustion than it would be in an inert environment because a portion of the collisions that would result in heat transfer in an inert environment may result in chemical reaction in a combustion environment. Molecular dynamics may be able to estimate this effect, but the interatomic potential forces again will need accurate description in order to model this effect.

# REFERENCES


[1] I. Altman, "High-temperature estimation of energy accommodation coefficient of gas molecules on the surface," *Journal of Physical Studies*, vol. 3, pp. 456–457, 1999.

[2] G. A. Risha, B. J. Evans, E. Boyer, R. B. Wehrman, and K. K. Kuo, "Nano-sized aluminum-and boron-based solid-fuel characterization in a hybrid rocket engine," in *39th AIAA Joint Propulsion Conference and Exhibit, Huntsville, Alabama*, 2003.

[3] K. Kuo, *Challenges in Propellants and Combustion: 100 Years After Nobel*. Begell House Publishers, Incorporated, 1997.

[4] M. Sitarski and J. H. Seinfeld, "Brownian coagulation in the transition regime," *Journal of Colloid And Interface Science*, vol. 61, no. 2, pp. 261–271, 1977.

[5] G. A. Risha, S. F. Son, R. Yetter, V. Yang, and B. Tappan, "Combustion of nano-aluminum and liquid water," *Proceedings of the Combustion Institute*, vol. 31, no. 2, pp. 2029–2036, 2007.

[6] Y. Huang, G. A. Risha, V. Yang, and R. A. Yetter, "Analysis of nano-aluminum particle dust cloud combustion in different oxidizer environments," in *43 rd Aerospace Sciences Meeting and Exhibit, AIAA*, 2005, pp. 2005–0738.

[7] L. Meda, G. Marra, L. Galfetti, F. Severini, and L. De Luca, "Nano-aluminum as energetic material for rocket propellants," *Materials Science and Engineering: C*, vol. 27, no. 5, pp. 1393–1396, 2007.

[8] M. L. Pantoya and J. J. Granier, "Combustion behavior of highly energetic thermites: Nano versus micron composites," *Propellants, Explosives, Pyrotechnics*, vol. 30, no. 1, pp. 53–62, 2005.

[9] T. A. Roberts, R. L. Burton, and H. Krier, "Ignition and combustion of aluminummagnesium alloy particles in o2 at high pressures," *Combustion and Flame*, vol. 92, no. 1, pp. 125–143, 1993.

[10] C.-L. Yeh and K. Kuo, "Ignition and combustion of boron particles," *Progress in energy and combustion science*, vol. 22, no. 6, pp. 511–541, 1996.

[11] J. Moore, S. Turns, and R. Yetter, "Combustion of lithiumaluminum alloys," *Combust. Sci. and Tech.*, vol. 177, no. 4, pp. 627–669, 2005.

[12] A. Maek, "Fundamentals of combustion of single aluminum and beryllium particles," in *Symposium (International) on Combustion*, vol. 11. Elsevier, 1967, pp. 203–217.

[13] J. Peuker, "Using optical techniques to measure aluminum burning in post-detonation explosive fireballs," Ph.D. dissertation, 2012.

[14] T. R. Sippel, S. F. Son, and L. J. Groven, "Altering reactivity of aluminum with selective inclusion of polytetrafluoroethylene through mechanical activation," *Propellants, Explosives, Pyrotechnics*, vol. 38, no. 2, pp. 286–295, 2013.

[15] A. Ulas, K. K. Kuo, and C. Gotzmer, "Ignition and combustion of boron particles in fluorine-containing environments," *Combustion and flame*, vol. 127, no. 1, pp. 1935–1957, 2001.

[16] M. Beckstead, "Correlating aluminum burning times," *Combustion, Explosion and Shock Waves*, vol. 41, no. 5, pp. 533–546, 2005.

[17] K. Park, D. Lee, A. Rai, D. Mukherjee, and M. Zachariah, "Size-resolved kinetic measurements of aluminum nanoparticle oxidation with single particle mass spectrometry," *The Journal of Physical Chemistry B*, vol. 109, no. 15, pp. 7290–7299, 2005.

[18] A. Rai, K. Park, L. Zhou, and M. Zachariah, "Understanding the mechanism of aluminium nanoparticle oxidation," *Combustion Theory and Modelling*, vol. 10, no. 5, pp. 843–859, 2006.

[19] T. Bazyn, H. Krier, and N. Glumac, "Evidence for the transition from the diffusion-limit in aluminum particle combustion," *Proceedings of the Combustion Institute*, vol. 31, no. 2, pp. 2021–2028, 2007.

[20] P. Lynch, H. Krier, and N. Glumac, "A correlation for burn time of aluminum particles in the transition regime," *Proceedings of the Combustion Institute*, vol. 32, no. 2, pp. 1887–1893, 2009.

[21] S. Mohan, M. A. Trunov, and E. L. Dreizin, "Heating and ignition of metal particles in the transition heat transfer regime," *Journal of heat transfer*, vol. 130, no. 10, 2008.

[22] P. Bucher, R. Yetter, F. Dryer, E. Vicenzi, T. Parr, and D. Hanson-Parr, "Observations on aluminum particles burning in various oxidizers," in *Princeton Univ, The 33 rd JANNAF Combustion Subcommittee Meeting p 449- 458(SEE N 97-18565 01-25)*, 1996.

[23] T. Bazyn, H. Krier, and N. Glumac, "Oxidizer and pressure effects on the combustion of 10-micron aluminum particles," *Journal of propulsion and power*, vol. 21, no. 4, pp. 577–582, 2005.

[24] M. A. Trunov, S. M. Umbrajkar, M. Schoenitz, J. T. Mang, and E. L. Dreizin, "Oxidation and melting of aluminum nanopowders," *The Journal of Physical Chemistry B*, vol. 110, no. 26, pp. 13 094–13 099, 2006.

[25] T. Bazyn, H. Krier, and N. Glumac, "Combustion of nanoaluminum at elevated pressure and temperature behind reflected shock waves," *Combustion and Flame*, vol. 145, no. 4, pp. 703–713, 2006.

[26] M. A. Trunov, M. Schoenitz, X. Zhu, and E. L. Dreizin, "Effect of polymorphic phase transformations in al2o3 film on oxidation kinetics of aluminum powders," *Combustion and Flame*, vol. 140, no. 4, pp. 310 – 318, 2005.

[27] M. A. Trunov, M. Schoenitz, and E. L. Dreizin, "Ignition of aluminum powders under different experimental conditions," *Propellants, Explosives, Pyrotechnics*, vol. 30, no. 1, pp. 36–43, 2005.

[28] V. Rosenband, "Thermo-mechanical aspects of the heterogeneous ignition of metals," *Combustion and Flame*, vol. 137, no. 3, pp. 366–375, 2004.

[29] S. Yuasa, Y. Zhu, and S. Sogo, "Ignition and combustion of aluminum in oxygen/nitrogen mixture streams," *Combustion and flame*, vol. 108, no. 4, pp. 387–396, 1997.

[30] I. Glassman and R. Yetter, *Combustion*. Academic press, 2008.

[31] J. C. Melcher, H. Krier, and R. L. Burton, "Burning aluminum particles inside a laboratory-scale solid rocket motor," *Journal of propulsion and power*, vol. 18, no. 3, pp. 631–640, 2002.

[32] T. Bazyn, "Spectroscopic measurements of the combustion of aluminum and aluminum-based energetic material particles using a heterogeneous shock tube," Ph.D. Thesis, University of Illinois at Urbana-Champaign. Dept. of Mechanical and Industrial Engineering, 2006.

[33] B. Legrand, M. Marion, C. Chauveau, I. Gokalp, and E. Shafirovich, "Ignition and combustion of levitated magnesium and aluminum particles and carbon dioxide," *Combustion Science and Technology*, vol. 165, pp. 151–174, 2001.

[34] V. I. Levitas, "Burn time of aluminum nanoparticles: Strong effect of the heating rate and melt-dispersion mechanism," *Combustion and Flame*, vol. 156, no. 2, pp. 543–546, 2009.

[35] V. I. Levitas, B. W. Asay, S. F. Son, and M. Pantoya, "Melt dispersion mechanism for fast reaction of nanothermites," *Applied Physics Letters*, vol. 89, no. 7, pp. 071 909–071 909–3, 2006.

[36] K. Aita, N. Glumac, S. Vanka, and H. Krier, "Modeling the combustion of nano-sized aluminum particles," *AIAA Paper*, vol. 1156, 2006.

[37] P. Lynch, "High temperature spectroscopic measurements of aluminum combustion in a heterogeneous shock tube," Ph.D. dissertation, 2010.

[38] S. Chowdhury, K. Sullivan, N. Piekiel, L. Zhou, and M. R. Zachariah, "Diffusive vs explosive reaction at the nanoscale," *The Journal of Physical Chemistry C*, vol. 114, no. 20, pp. 9191–9195, 2010.

[39] P. Lynch, G. Fiore, H. Krier, and N. Glumac, "Gas-phase reaction in nanoaluminum combustion," *Combustion Science and Technology*, vol. 182, no. 7, pp. 842–857, 2010.

[40] D. Allen, H. Krier, and N. Glumac, "Heat transfer effects in nanoaluminum combustion at high temperatures," *Combustion and Flame*, vol. 161, no. 1, pp. 295–302, 2014.

[41] S. F.M, "Convective heat transfer from spheres in a free-molecule flow," *Journal of the Aeronautical Sciences (Institute of the Aeronautical Sciences)*, vol. 18, no. 5, pp. 353–354, 1951.

[42] A. Filippov and D. Rosner, "Energy transfer between an aerosol particle and gas at high temperature ratios in the knudsen transition regime," *International journal of heat and mass transfer*, vol. 43, no. 1, pp. 127–138, 2000.

[43] H. Levey, "Heat transfer in slip flow at low reynolds number," *Journal of Fluid Mechanics*, vol. 6, no. 03, pp. 385–391, 1959.

[44] F. Liu, K. Daun, D. R. Snelling, and G. J. Smallwood, "Heat conduction from a spherical nano-particle: status of modeling heat conduction in laser-induced incandescence," *Applied Physics B*, vol. 83, no. 3, pp. 355–382, 2006.

[45] F. O. Goodman and H. Y. Wachman, "Formula for thermal accommodation coefficients," *The Journal of Chemical Physics*, vol. 46, no. 6, pp. 2376–2386, 1967.

[46] F. O. Goodman and H. Y. Wachman, "Dynamics of gas-surface scattering academic," *New York*, vol. 33, 1976.

[47] K. Daun, M. Karttunen, and J. Titantah, "Molecular dynamics simulation of thermal accommodation coefficients for laser-induced incandescence sizing of nickel nanoparticles," in *ASME 2011 International Mechanical Engineering Congress and Exposition*. American Society of Mechanical Engineers, 2011, pp. 307–315.

[48] K. Daun, T. Sipkens, J. Titantah, and M. Karttunen, "Thermal accommodation coefficients for laser-induced incandescence sizing of metal nanoparticles in monatomic gases," *Applied Physics B*, vol. 112, no. 3, pp. 409–420, 2013.

[49] V. Chirita, B. Pailthorpe, and R. Collins, "Molecular dynamics study of low-energy ar scattering by the ni (001) surface," *Journal of Physics D: Applied Physics*, vol. 26, no. 1, p. 133, 1993.

[50] I. Altman, D. Lee, J. Song, and M. Choi, "Experimental estimate of energy accommodation coefficient at high temperatures," *Physical Review E*, vol. 64, no. 5, p. 052202, 2001.

[51] F. Liu, G. J. Smallwood, and D. R. Snelling, "Effects of primary particle diameter and aggregate size distribution on the temperature of soot particles heated by pulsed lasers," *Journal of Quantitative Spectroscopy and Radiative Transfer*, vol. 93, no. 1, pp. 301–312, 2005.

[52] S. Will, S. Schraml, and A. Leipertz, "Two-dimensional soot-particle sizing by time-resolved laser-induced incandescence," *Optics letters*, vol. 20, no. 22, pp. 2342–2344, 1995.

[53] B. F. Kock, T. Eckhardt, and P. Roth, "In-cylinder sizing of diesel particles by time-resolved laser-induced incandescence (tr-lii)," *Proceedings of the Combustion Institute*, vol. 29, no. 2, pp. 2775–2782, 2002.

[54] K. Daun, "Thermal accommodation coefficients between polyatomic gas molecules and soot in laser-induced incandescence experiments," *International Journal of Heat and Mass Transfer*, vol. 52, no. 21, pp. 5081–5089, 2009.

[55] Y. Murakami, T. Sugatani, and Y. Nosaka, "Laser-induced incandescence study on the metal aerosol particles as the effect of the surrounding gas medium," *The Journal of Physical Chemistry A*, vol. 109, no. 40, pp. 8994–9000, 2005.

[56] D. R. Snelling, F. Liu, G. J. Smallwood, and m. L. Glder, "Determination of the soot absorption function and thermal accommodation coefficient using low-fluence lii in a laminar coflow ethylene diffusion flame," *Combustion and Flame*, vol. 136, no. 1, pp. 180–190, 2004.

[57] A. Eremin, E. Gurentsov, and C. Schulz, "Influence of the bath gas on the condensation of supersaturated iron atom vapour at room temperature," *Journal of Physics D: Applied Physics*, vol. 41, no. 5, p. 055203, 2008.

[58] B. F. Kock, C. Kayan, J. Knipping, H. R. Orthner, and P. Roth, "Comparison of lii and tem sizing during synthesis of iron particle chains," *Proceedings of the Combustion Institute*, vol. 30, no. 1, pp. 1689–1697, 2005.

[59] R. L. Vander Wal, T. M. Ticich, and J. R. West, "Laser-induced incandescence applied to metal nanostructures," *Applied optics*, vol. 38, no. 27, pp. 5867–5879, 1999.

[60] A. Eremin, E. Gurentsov, M. Hofmann, B. Kock, and C. Schulz, "Nanoparticle formation from supersaturated carbon vapour generated by laser photolysis of carbon suboxide," *Journal of Physics D: Applied Physics*, vol. 39, no. 20, p. 4359, 2006.

[61] H. A. Michelsen, "Derivation of a temperature-dependent accommodation coefficient for use in modeling laser-induced incandescence of soot," *Applied Physics B*, vol. 94, no. 1, pp. 103–117, 2009.

[62] D. A. Gryvnak and D. E. Burch, "Optical and infrared properties of al¡ sub¿ 2¡/sub¿ o¡ sub¿ 3¡/sub¿ at elevated temperatures," *JOSA*, vol. 55, no. 6, pp. 625–629, 1965.

[63] C. F. Bohren and D. R. Huffman, *Absorption and scattering of light by small particles*. John Wiley and Sons, 2008.

[64] S. Goroshin, J. Mamen, A. Higgins, T. Bazyn, N. Glumac, and H. Krier, "Emission spectroscopy of flame fronts in aluminum suspensions," *Proceedings of the Combustion Institute*, vol. 31, no. 2, pp. 2011–2019, 2007.

[65] P. Lynch, H. Krier, and N. Glumac, "Emissivity of aluminum-oxide particle clouds: Application to pyrometry of explosive fireballs," *Journal of Thermophysics and Heat Transfer*, vol. 24, no. 2, pp. 301–308, 2010.

[66] J. Kalman, D. Allen, N. Glumac, and H. Krier, "Optical depth effects on aluminum oxide spectral emissivity," *Journal of Thermophysics and Heat Transfer*, vol. Accepted for Publication, 2014.

[67] M. Spalding, "Boron particle ignition and combustion in a shock tube using time resolved spectroscopy," Masters, 2000.

[68] T. A. Bazyn, "Spectroscopic measurements of the combustion of aluminum and aluminum-based energetic material particles using a heterogeneous shock tube," Ph.D. dissertation, 2006.

[69] P. Lynch, "High temperature spectroscopic measurements of aluminum combustion in a heterogeneous shock tube," Ph.D. Thesis, University of Illinois at Urbana-Champaign. Dept. of Mechanical Science and Engineering, 2010.

[70] A. Gaydon., *The Shock Tube in High Temperature Chemical Physics*. Reinhold Publishing Corporation, 1963.

[71] J. N. Bradley, *Shock waves in chemistry and physics*. Methuen London, 1962.

[72] I. I. Glass and J. P. Sislian, *Nonstationary flows and shock waves*. Clarendon Press Oxford, 1994.

[73] N. Glumac, H. Krier, T. Bazyn, and R. Eyer, "Temperature measurements of aluminum particles burning in carbon dioxide," *Combustion Science and Technology*, vol. 177, pp. 485–511, 2005.

[74] R. Starke, B. Kock, and P. Roth, "Nano-particle sizing by laser-induced-incandescence (lii) in a shock wave reactor," *Shock Waves*, vol. 12, no. 5, pp. 351–360, 2003.

[75] N. Glumac, H. Krier, T. I. M. Bazyn, and R. Eyer, "Temperature measurements of aluminum particles burning in carbon dioxide," *Combustion Science and Technology*, vol. 177, no. 3, pp. 485–511, 2005.

[76] P. Santhanam, V. Hoffmann, M. Trunov, and E. Dreizin, "Characteristics of aluminum combustion obtained from constant-volume explosion experiments," *Combustion Science and Technology*, vol. 182, no. 7, pp. 904–921, 2010.

[77] O. Brandt, A. Rajathurai, and P. Roth, "First observations on break-up of particle agglomerates in shock waves," *Experiments in fluids*, vol. 5, no. 2, pp. 86–94, 1987.

[78] J. J. Strecker and P. Roth, "Particle breakup in shock waves studies by single particle light scattering," *Particle and particle systems characterization*, vol. 11, no. 3, pp. 222–226, 1994.

[79] L. Forney and W. McGregor, "Scaling laws for particle breakup in nozzle generated shocks," *Particulate Science and Technology*, vol. 1, no. 4, pp. 419–431, 1983.

[80] L. P. Bakhir, G. I. Levashenko, and V. V. Tamanovich, "Refinement of the imaginary part of the complex refractive index of liquid aluminum oxide," *Journal of Applied Spectroscopy*, vol. 26, pp. 378–383, 1977.

[81] D. L. Parry and M. Brewster, "Optical constants of $Al_2O_3$ smoke in propellant flames," *Journal of Thermophysics and Heat Transfer*, vol. 5, no. 2, pp. 142 – 149, 1991.

[82] R. Reed and V. Calia, Eds., *Review of aluminum oxide rocket exhaust particles*, July 1993.

[83] A. Medvedev, A. Fedorov, and V. Fomin, "Mathematical modeling of metal particle ignition in the high-temperature flow behind a shock," *Combustion, Explosion, and Shock Waves*, vol. 18, no. 3, pp. 261–265, 1982.

[84] V. J. H. J. Vladimir Hlavacek, Hilmar Rode and J. E. Gatica, "Combustion of metallic powders: a phenomenological model for the initiation of combustion," *Combustion science and technology*, vol. 88, no. 3-4, pp. 153–175, 1993.

[85] Y. Huang, G. A. Risha, V. Yang, and R. A. Yetter, "Effect of particle size on combustion of aluminum particle dust in air," *Combustion and Flame*, vol. 156, no. 1, pp. 5–13, 2009.

[86] M. Fitzgerald, "Optical measurements of nano-aluminum combustion in a heterogeneous shock tube and in a flat flame burner," 2014.

[87] J. T. Brown, "Comparison of ignition characteristics of pure and coated aluminum powder in a shock tube facility," Ph.D. dissertation, 2007.

[88] D. M. Kalitian and E. L. Petersen, "Nano-aluminum aerosol characterization with application to heterogeneous shock-tube combustion," in *5th US Combustion Meeting*.

[89] C. Kong, Q. Yao, D. Yu, and S. Li, "Combustion characteristics of well-dispersed aluminum nanoparticle streams in post flame environment," *Proceedings of the Combustion Institute*, 2014.

[90] A. Dahoe, "Laminar burning velocities of hydrogenair mixtures from closed vessel gas explosions," *Journal of Loss Prevention in the Process Industries*, vol. 18, no. 3, pp. 152–166, 2005.

[91] G. Skandan, Y. Chen, N. Glumac, and B. Kear, "Synthesis of oxide nanoparticles in low pressure flames," *Nanostructured materials*, vol. 11, no. 2, pp. 149–158, 1999.